2. THE RESULTS OF SPACE RESEARCH OF THE INSTITUTES IN 2006–2007

2.1. THE RESULTS OF THE COMPLETED FLIGHT SCIENTIFIC PROGRAMMES OF INVESTIGATION AND OBSERVATION

2.1.1. SPACE RESEARCH INSTITUTE OF THE RAS

2.1.1.1. High energy astrophysics

1. Large scale structure of the local Universe in hard X-rays and measuring the cosmic hard X-ray background with INTEGRAL

While on very large scales our Universe is isotropic and homogeneous, on scales smaller than 100–200 Mpc there are large concentrations of mass, separated by voids, which form so called Large Scale Structure of the Universe. Clear signatures of the local Large Scale Structure in the spatial distribution of nearby X-ray luminous active galactic nuclei were found by the INTEGRAL observatory during an all-sky survey.

We know from optical and infrared galaxy surveys that the distribution of visible mass in the local Universe (within a few hundred Mpc from us) is far from uniform. The number density of galaxies may vary by an order of magnitude between galaxy superclusters and voids. The highest known mass agglomerations ($M > 10^{15}$ Msun) in the local Universe include the nearby Virgo cluster and the more distant Great Attractor and Perseus-Pisces supercluster. It is now generally accepted that practically every galaxy in the local Universe has a supermassive black hole in its center and some of these black holes are active galactic nuclei (AGNs). It is therefore natural to anticipate that the space density of AGNs should be proportional to the space density of ordinary galaxies.

A recent hard X-ray survey of the whole sky performed by the INTErnational Gamma-Ray Astrophysics Laboratory (INTEGRAL) provided an unbiased census of AGNs in the local Universe. Thanks to the hard X-ray selection, the obtained sample includes many dust-enshrouded AGNs, which are not visible at optical and soft X-ray wavelengths. The effective depth of the survey allows one to effectively probe the nearby Universe out to distances of order 100 Mpc. Indeed, the distribution of nearby AGNs is found to be strongly anisotropic. It also matches well the mass concentrations in the local Universe (green contours on the Fig. 1) as traced by the «IRAS point source catalogue red-shift survey» at distances smaller than about 230 million light years (70 Mpc).

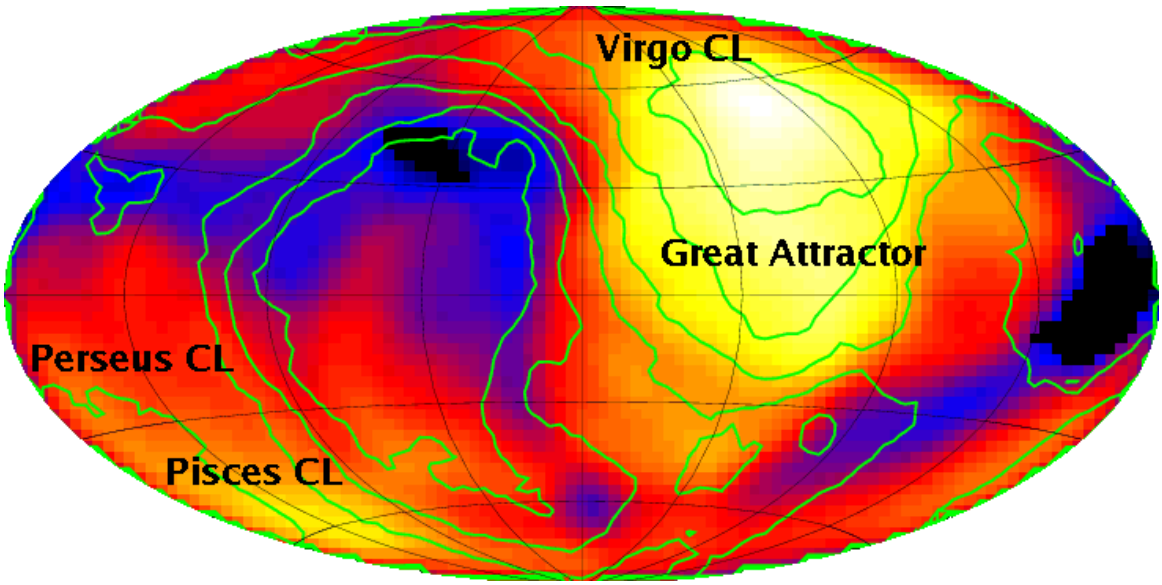

Figure 1: Space density of nearby hard X-ray bright AGNs in different directions of the sky. Each pixel in the map represents the number density of sources within a cone of space with a half-opening angle of 45 degrees. The image demonstrates that the distribution of nearby AGNs is indeed strongly anisotropic, as expected. For comparison, green contours show a usual tracer of mass concentrations in the local Universe - the surface density of IRAS PSCz galaxies at distances smaller than 70 Mpc. The large-scale feature in the north-east direction is consistent with the projected position of the highest mass concentrations in the local Universe - the Virgo cluster and the Great Attractor. The south-western structure is consistent with the Perseus — Pisces supercluster.

Supermassive black holes millions and billions times heavier than our Sun are lurking in the centers of all galaxies. Many of these black holes are dormant now, but each had a period of rapid growth in its history when a vast amount of radiation was emitted. All together the growing black holes are believed to be making a dominant contribution to the «cosmic X-ray background» (CXB) — hard radiation filling the space around us.

Understanding the nature of the CXB means that we know its flux and that we can account for all of it in terms of known populations of objects. At low energies (below few keV) deep surveys with large X-ray telescopes like XMM-Newton and Chandra already resolve 90 % of the CXB, directly counting of order of 1000 sources per square degree of the sky. At energies higher than 10 or 20 keV such an exercise is far beyond the capabilities of existing instruments and other techniques have been employed by the INTEGRAL observatory to study the CXB above 20 keV. Aiming at measuring the total CXB flux, the INTEGRAL observatory spent several days looking directly at the Earth disk. The Earth served as a giant shield, which blocks the emission of a distant source and causes a decrease in the flux seen by INTEGRAL. By measuring this decrease the combined emission from all distant sources, no matter how weak they are, can be measured. This is schematically shown in Fig. 2, where the Earth disk is superposed onto the all sky 20–50 keV map obtained by INTEGRAL.

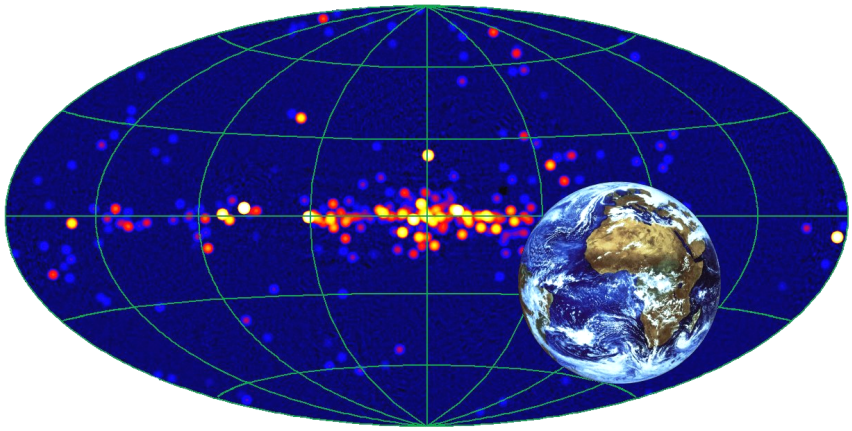

Figure 2: 17–60 keV all-sky image obtained by INTEGRAL during four years of operations. The concentration of sources along the mid-plane of the image is due to neutron stars and stellar mass black holes in our Galaxy, while the majority of sources located far away from the Galactic plane are supermassive black holes in other galaxies. The Cosmic X-ray Background is composed of the emission of tens of millions of similar objects much further away from us. Superposed is an Earth image by ESA/EUMETSAT's Meteosat satellite. Blocking the emission from a distant source by the Earth disk allows astronomers to measure the intensity of the X-ray and gamma-ray background. An angular size of the Earth as seen from Integral during actual observations was smaller than shown in the image.

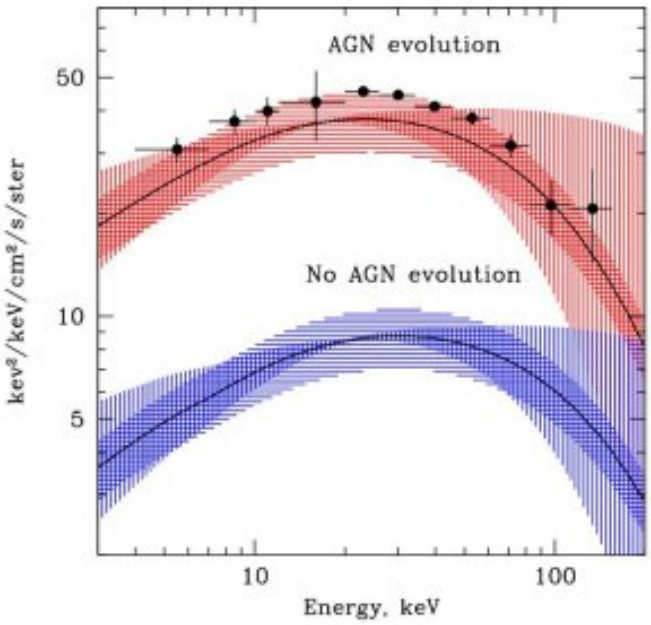

Figure 3: Upper part of the plot: Solid line - the result of convolving the local cumulative AGN spectrum with the redshift dependence of the AGN X-ray luminosity density inferred from deep extragalactic surveys conducted by Chandra and XMM-Newton. The vertically hatched region represents the associated statistical uncertainty and the horizontally hatched region the additional 20% systematic uncertainty in the overall normalization. The points with error bars represent the cosmic X-ray background spectrum measured by INTEGRAL during Earth occultation observations. For comparison in the lower part of the plot the result of a similar calculation for the case of no cosmological evolution of AGN (i.e. the same total AGN luminosity per cubic Mpc at all redshifts as at z=0) is shown.

Using the INTEGRAL all-sky data the cumulative spectrum of the local (at redshift $z < 0.1$) AGN population in the broad energy band 3–300 keV was calculated. To this end a stacking analysis was performed of the spectra of 84 AGN detected by the PCA instrument aboard RXTE and of 68 AGN detected by the IBIS/ISGRI instrument aboard INTEGRAL, properly taking into account the space densities of AGN with different luminosities (using the well-known 1/Vmax technique).

Now, knowing the total flux of the CXB and the detailed properties of the local population of active black holes, scientists are able to learn more on how such black holes have been evolving from early times (corresponding to redshifts $z \sim 1.5$) till today ($z = 0$, Fig. 3).

It turns out that both the amplitude and spectral distribution of the CXB can be explained if the AGN population as a whole has experienced pure luminosity downsizing (from bright quasars to relatively weak Seyfert galaxies), as suggested by deep extragalactic X-ray surveys, while its other key properties such as the ratio of obscured to unobscured AGNs have not changed. This has important implications for theoretical models trying to unify different types of AGNs based on geometrical orientation and physical properties.

2. Milky Way X-ray background

The origin of the so-called galactic X-ray background has been a long-standing mystery. This background is seeng as a diffuse X-ray glow of the Galactic plane, first found more than 30 years ago. Recent study suggests this X-ray light is not diffuse, as many have thought, but originates from hundreds of millions of individual sources dominated by white dwarfs and coronally active stars. The best evidence that the Galactic X-ray background might be associated with stellar population comes from the comparison with the near-infrared map of the Milky Way, taken by COBE satellite. Near-infrared light traces old stellar population of the Galaxy and the distribution of the X-ray background follow near-infrared extremely well (Fig. 4).

If the objects composing Galactic “diffuse” X-ray background are in fact discrete sources, they must be very faint in order to avoid direct detection and very numerous to account for total Milky Way (background) flux. Starting from this hypothesis the careful census of the X-ray objects in the close vicinity of the Solar system (within 100 pc) was made and the total luminosity function of discrete objects of the Milky Way was constructed.

These luminosity function, which spans 13 orders of magnitude, has two very prominent peaks: one due to bright Low Mass X-ray binaries and another one due to cataclysmic variables (CVs) and active binaries (ABs). The latter objects are faint enough and numerous enough to explain bulk of the Milky Way “diffuse” X-ray glow.

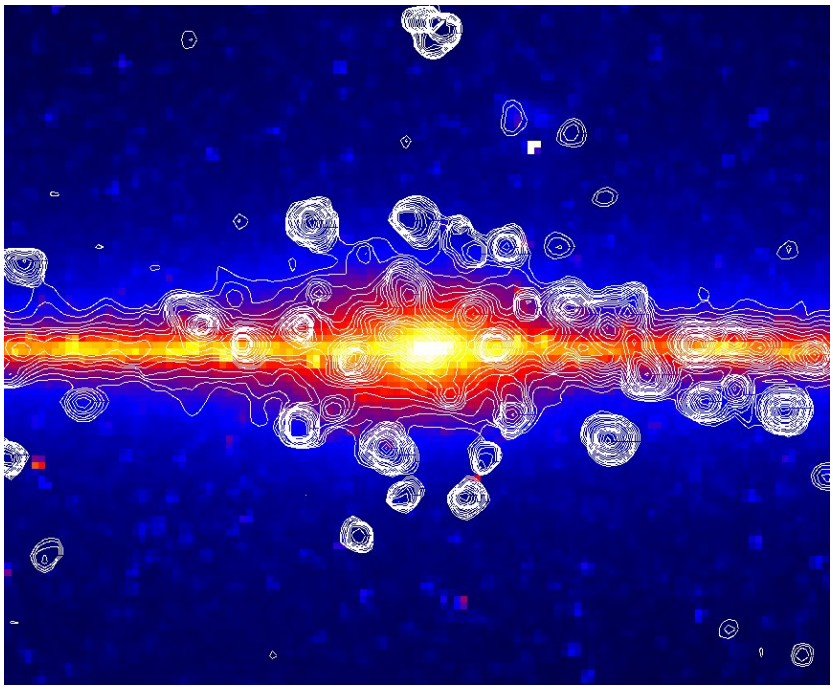

Figure 4: The perfect match between the X-ray image obtained by Rossi XTE (contours) and the near-infrared image of the Galaxy taken by COBE (color) suggests that X-ray emission traces stellar mass distribution and suggests that the Galactic X-ray background consists of a huge number of faint discrete sources.

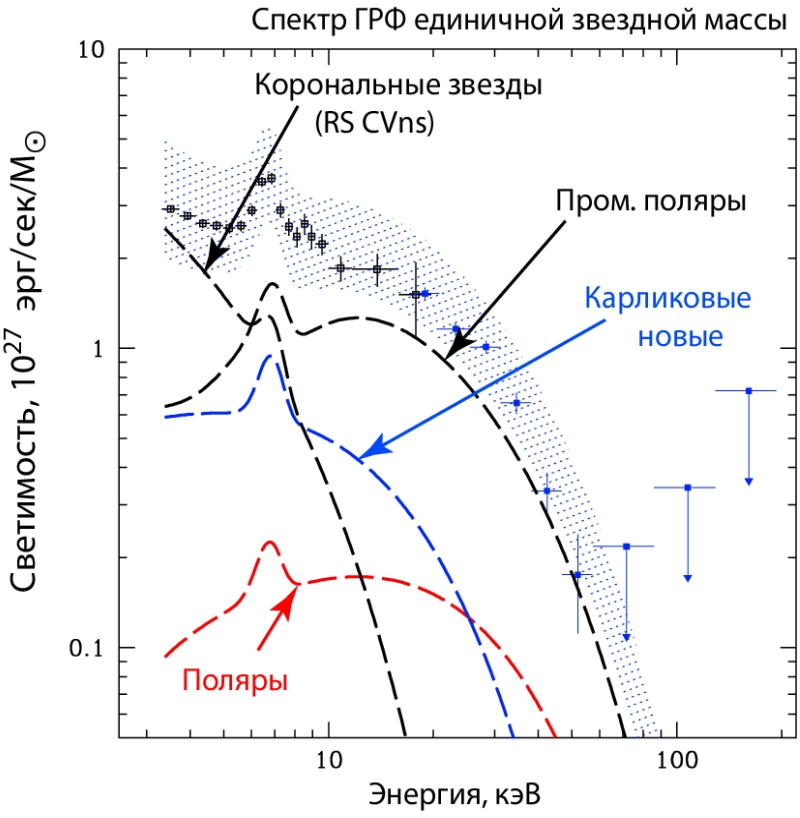

Figure 5: Energy spectra of faint X-ray emitters – white dwarfs at binary systems and coronally active stars.

The conclusion that discrete sources powers Galactic X-ray background resolves one of the long standing puzzles of source of energy needed to sustain Milky Way X-ray glow. It is now further confirmed that similar contribution of faint discrete sources dominates X-ray emission of gas poor elliptical galaxies, once the contribution of bright LMXBs is resolved.

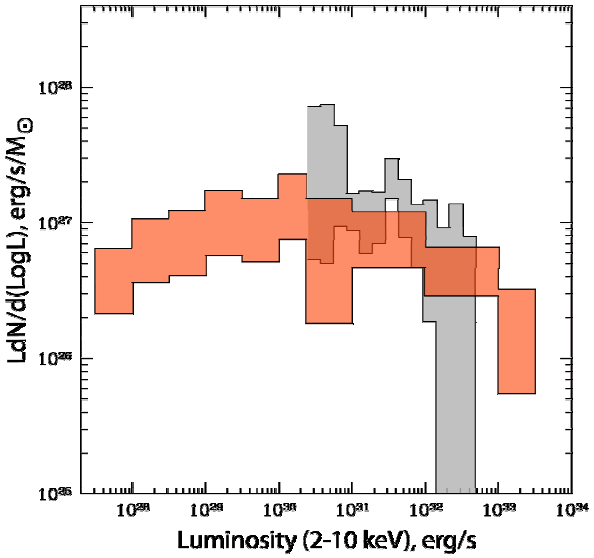

Figure 6: Luminosity functions of faint X-ray sources measured in the Solar vicinity (red area) and in the Galactic Center region (gray area). It can be seen that they are quite compatible with each other. The sources in the gray area explain at least 40–50 % of the total X-ray flux measured in the Galactic Center region, while still weaker sources expected to be present in this region by analogy with the Solar neighborhood, probably provide the remaining 50-60% of the total flux.

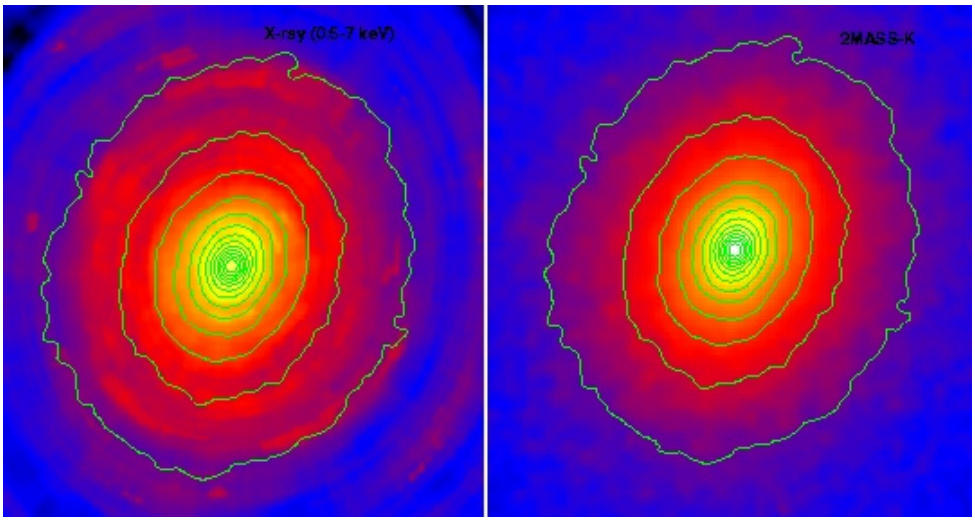

Figure 7: M32 elliptic galaxy in X-rays (left) and in infrared (right). Detailed study has shown that observed diffuse X-ray emission of the galaxy is result of summation of emission of faint discret sources – accreting white dwarf and coronal stars.

3. High mass X-ray binaries, star formation history and spiral structure of galaxies

High mass X-ray binaries (HMXBs) are young objects and thus should be tightly related to the recent star formation in the host galaxy. This hypothesis has been proposed a decades ago and is now supported by numerous observations of compact X-ray sources in various galaxies (at distances up to few tenths Mpc) with Chandra, XMM-Newton and preceding X-ray observatories. However the detailed quantitative relation between the population of HMXBs and the recent star formation in the host galaxy is yet to be understood. Indeed, while on the one hand recent Chandra and XMM-Newton observations of galaxies in the local Universe point to a simple linear relation between the number of HMXBs and recent star formation rate of the form N(HMXB) = A*SFR, theoretical considerations as well as some observational evidence seem to point to more complex relation taking into account recent star formation history (SFH) of the host galaxy over past 100 Myr (Shtykovskiy & Gilfanov, 2007).

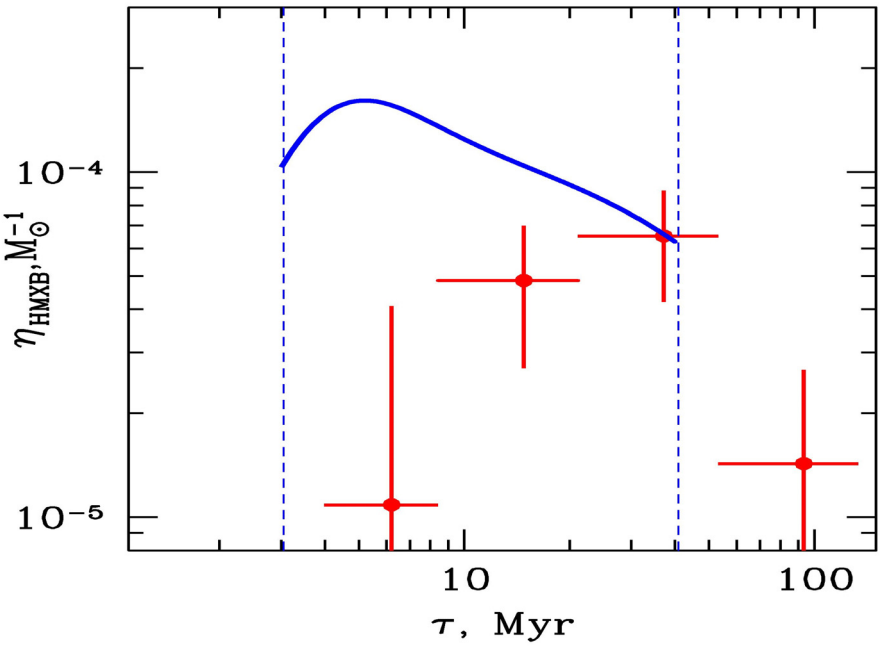

Figure 8: Dependence of the HMXBs number on time elapsed since the star formation burst obtained based on the X-ray (XMM-Newton) and optical observations of the Small Magellanic Cloud. Solid curve shows the behavior of type II SN rate, vertical lines show the formation times of the first black hole (~2–3 Myr) and the last neutron star (~40 Myr).

Our neighbors, the Magellanic Clouds, thanks to their proximity, provide a unique opportunity to study this problem in details. For this purpose, using the archive optical data, we reconstructed the spatially-resolved recent SFH of the Small Magellanic Cloud. Combining it with the spatial distribution of HMXBs in the SMC, we reconstructed the time-dependent evolution of HMXBs number after the star formation burst (Fig.8). As is clear from the figure, the maximum abundance

of HMXBs is reached ~20–50 Myr after the SF burst, followed by a rapid decay. On the other hand, the number of HMXBs younger than 10 Myr is also small, pointing to a low contribution of systems with black holes and supergiant donors. The obtained dependence is of importance due to several reasons. First of all, it relates the number of HMXBs to the recent SFH in the host galaxy and provides a better understanding of the former as a star formation proxy. On the other hand it gives possibility to test population synthesis models and predicts a number of observational effects.

One of such effects is related to the spatial distribution of HMXBs in the spiral galaxies. We demonstrated that significant time required for the HMXBs abundance to reach its maximum leads to their shift relative to the spiral structure as observed in such classic star formation indicators as Hα hydrogen line. We constructed a simple kinematic model of this effect and discussed it's dependence on the HMXB type and luminosity. Observations of such a shift may provide useful information on the spiral structure of the host galaxy as well as on the HMXB evolution. The predictions of the model were compared with the Chandra observations of M51 (fig.9) and INTEGRAL observations of HMXBs in our galaxy.

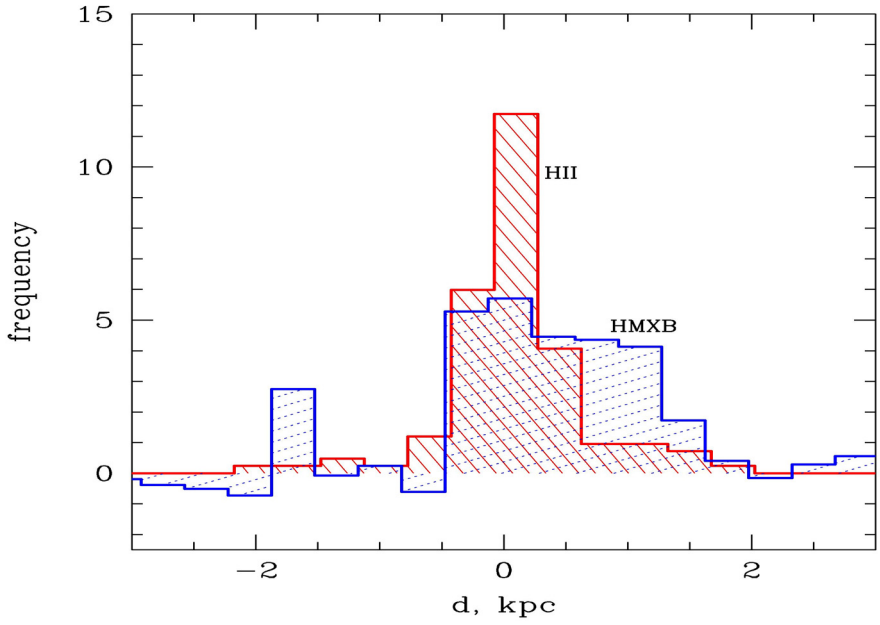

Figure 9: Distribution of HMXBs (blue histogram) and HII regions (red histogram) distances relative to the closest spiral arm. The former distribution is wider than the latter due to the finite lifetime required for the HMXB abundance to reach its maximum.

4. The 400 Square Degree ROSAT PSPC Galaxy Cluster Survey: Catalog and Statistical Calibration

We present a catalog of galaxy clusters detected in a new ROSAT PSPC survey. The survey is optimized to sample, at high redshifts, the mass range corresponding

to T>5 keV clusters at z=0. The new survey covers 397 deg2 and is based on 1610 high Galactic latitude ROSAT PSPC pointing, virtually all pointed ROSAT data suitable for the detection of distant clusters. The search volume for X-ray luminous clusters within z<1 exceeds that of the entire local universe ($z < 0.1$). Our sample clearly shows a decrease in the number density for the most luminous clusters at $z > 0.3$.

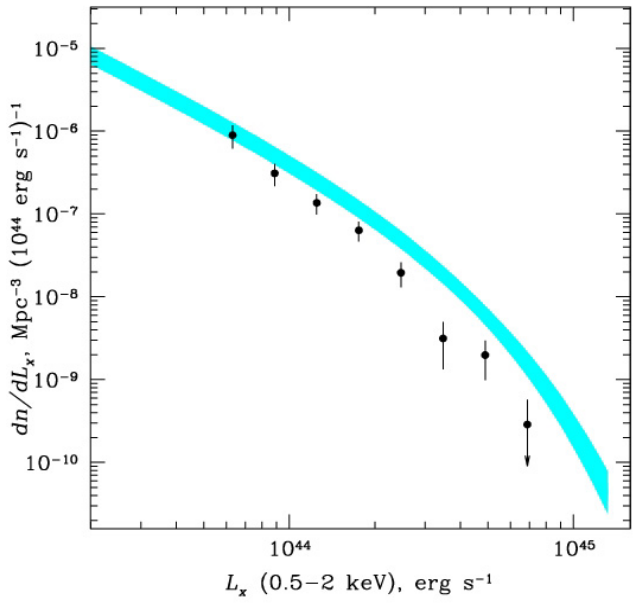

Figure 10: The X-ray luminosity functions of distant (z>0.3) galaxy clusters from 400d survey (data points) and nearby galaxy clusters from ROSAT All-Sky Survey (shaded region). The cosmological evolution of clusters X-ray luminosity function is clearly seen.

The subsample of 40 most distant and massive clusters from our survey was reobserved by Chandra in order to obtain accurate measurements of the masses of clusters. These data will allow to set new constraints on the dark energy equation of state.

5. Optical identifications of hard X-ray sources from INTERGAL, SWIFT and RXTE surveys

We started the works on the optical identifications of hard X-ray sources from INTERGAL, SWIFT and RXTE all-sky surveys. Among these sources we identified about 20 previously unknown nearby (z<0.1) active galactic nuclei, several new cataclysmic variables and high-mass X-ray binaries.

6. Observations of gamma-ray bursts optical afterglows

We continued our observations of the gamma-ray bursts optical afterglows with Russian-Turkish 1.5-m Telescope (RTT150). The observations of 16 gamma-ray

bursts were done, including very well sampled photometric observations of GRB 060526. The observations of GRB 060526 afterglow were started from about 5 hours after the GRB and lasted for 5 consecutive nights. At approximately one day after the GRB the afterglow started to show highly variable light curve. It was suggested, that this variability may be a signature the transition to non-relativistic motion of the ejecta which should be expected in case of high interstellar density near the GRB source.

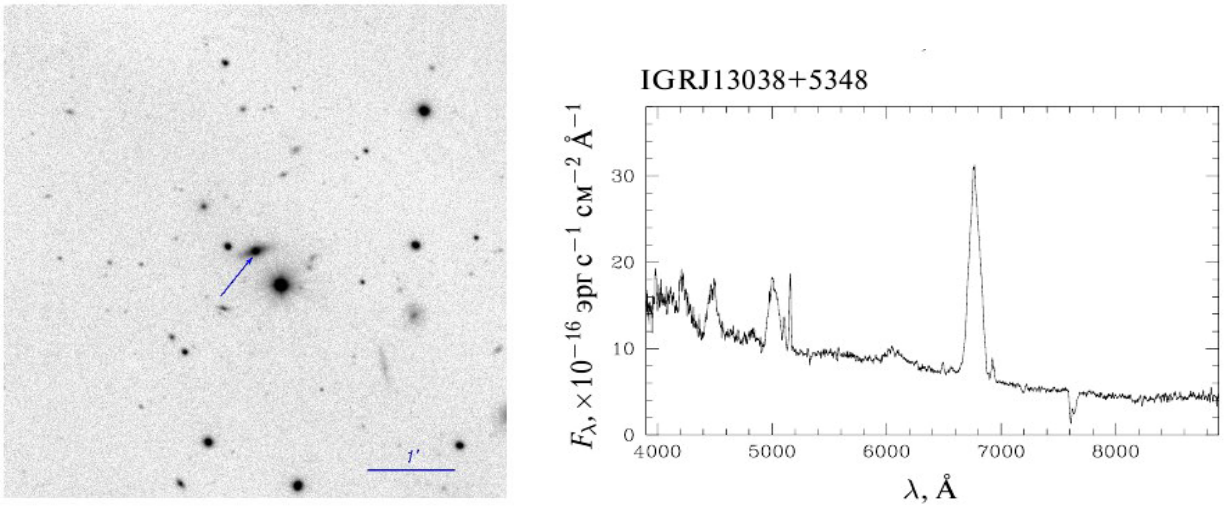

Figure 11: Optical identification of hard X-ray source IGRJ13038+5348 as a Seyfert 1 galaxy.

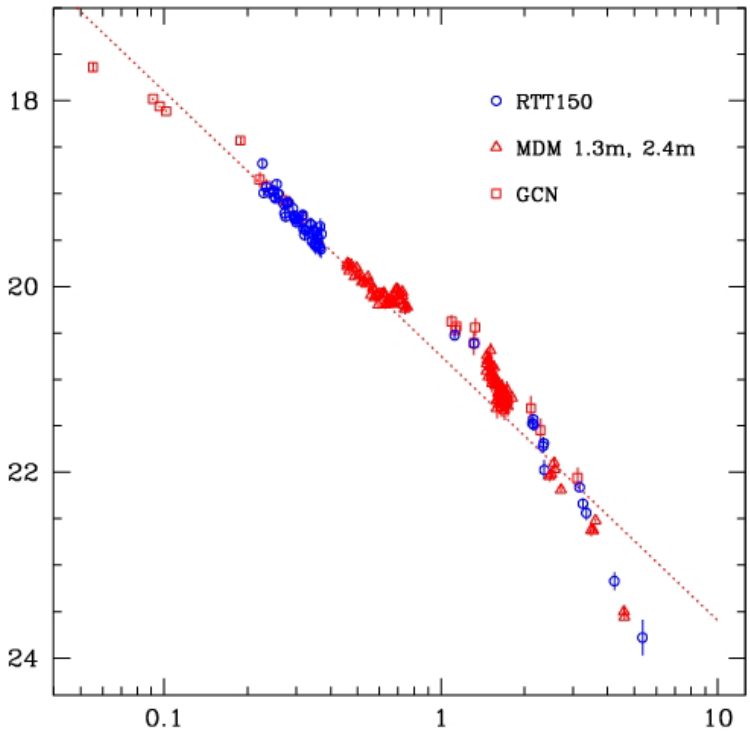

Figure 12: The light curve of the optical afterglow of GRB 060526.

7. Recombination spectrum calculations with two photons processes.

Roughly 260,000 years after the Big Bang the initially fully-ionized plasma became sufficiently cold to allow the existence of neutral hydrogen atoms. By that time the temperature of the nearly isotropic CMB blackbody radiation, which is filling the expanding Universe, had dropped to about 3800 K. The process of recombination is associated with the emission of several photons by electrons cascading from upper levels of the hydrogen atom to its ground state. For 40 years the kinetics of cosmological recombination is known to be extremely unusual: due to the very small expansion rate of the Universe the escape of photons from the Lyman-α resonance was extremely inefficient. This strongly enhanced the role of the very improbable two-photon decay of the metastable 2s level to the 1s state. About 57% of all electrons in recombined hydrogen atoms reached the ground state via the 2s-1s two-photon transition. As a result, the kinetics of recombination cannot be described by the formulae for Saha-equilibrium in cooling plasmas, and recombination was strongly delayed. In addition, because of the extremely high entropy of the Universe (with about $2x10^9$ photons per baryon), the primordial plasma is dominated by photons. Therefore collisions of atoms with electrons and ions played a negligible role, and the populations of highly excited levels were completely defined by radiative rates, including stimulated recombination and induced emission.

Detailed computations have allowed us to calculate the spectrum of the recombinational radiation arising from all possible atomic transitions of hydrogen among levels with principal quantum numbers up to 100 (see Fig. 13). Due to the expansion of the Universe this signal is redshifted more than 1000 times, so that ultraviolet photons reach the observer in the sub-mm band today. Transitions among highly excited levels lead to photons that nowadays should appear at radio frequencies, where experimental techniques developed for the extremely successful investigations of CMB angular fluctuations have achieved unprecedented sensitivity.

For experimentalists the ratio of the computed signal relative to the intensity of the CMB blackbody radiation is more representative (see Fig. 14). Most likely it will be easiest to search for the distortions under discussion in the low frequency domain, just above 1.4 GHz. This is because there the contributions from the lines of distant galaxies, especially due to the 21 cm line of neutral hydrogen, is minimal. The insert of Figure 2 illustrates the detailed frequency dependence of the features produced during cosmological recombination. These have a unique «pattern» which has nothing in common with other widely discussed and well-known foregrounds. Using the computed «template» observers may have a chance to separate the recombinational signal from possible sources of noise.

IKI and MPA scientists are proposing a new type of CMB experiment: instead of scanning the sky at given frequency and searching for tiny angular fluctuations of the CMB temperature, one should observe a large area of the sky, scanning its radiation over frequency, and looking for the predicted characteristic spectral

variability. Experiments under construction in the USA to observe the CMB angular fluctuations will have sensitivities on the level of 10 nK. The spectral features under discussion have amplitudes between 50 and 100 nK. It is very important to mention that the recombinational signal should be the same in any direction on the sky.

The position of the spectral features on the frequency axis strongly depends on the exact value of the CMB temperature. The best and only existing precise measurement of this value, as performed by the COBE spacecraft, was awarded the Nobel Prize in Physics, 2006. It is very important to have new independent methods to determine the CMB monopole, and the computations carried out at MPA might offer such an opportunity. Furthermore, the intensity of the features depends on the total amount of hydrogen nuclei in our Universe, and is practically independent of the values of the other key cosmological parameters. If the CMB monopole temperature is, an observation of these spectral distortions will provide an additional way to measure the entropy of the Universe. In principle it should also be possible to determine the abundance ratio between helium and hydrogen, and to reconstruct the detailed ionization history.

It is worth mentioning that the photons forming these small CMB spectral distortions were emitted mainly between redshifts z~1300 and 1400, i.e. before recombination made the Universe transparent, defining the last scattering surface around z~1100, at which the observed CMB angular fluctuations were formed. Therefore, a detection of the recombinational lines in the CMB spectrum will yield the final proof that recombination has occurred as we think it has.

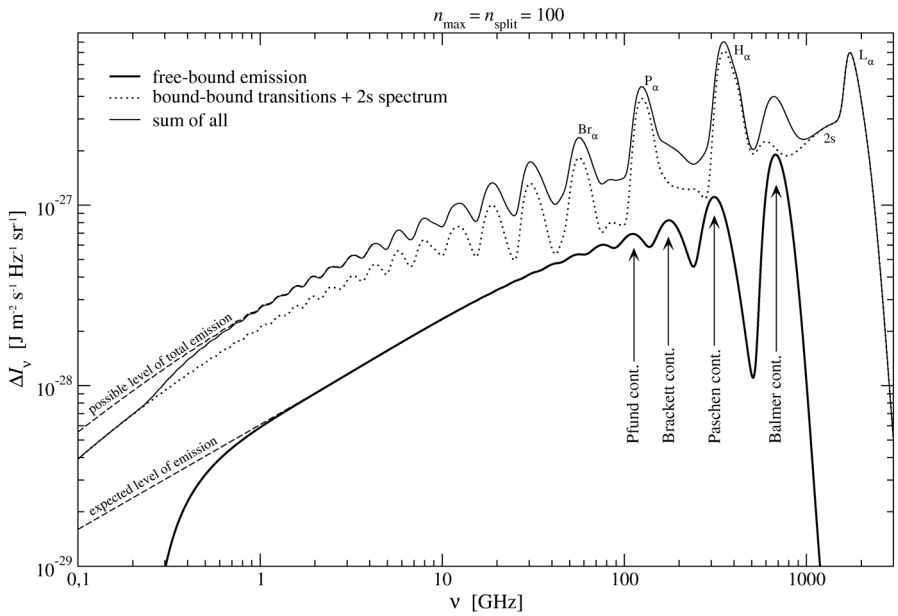

Figure 13: CMB spectral distortions due to cosmological hydrogen recombination. At high frequencies one can clearly see the features connected to the Lyman, Balmer, Paschen and Brackett series. At low frequencies the lines due to α-transitions among highly excited state overlap strongly.

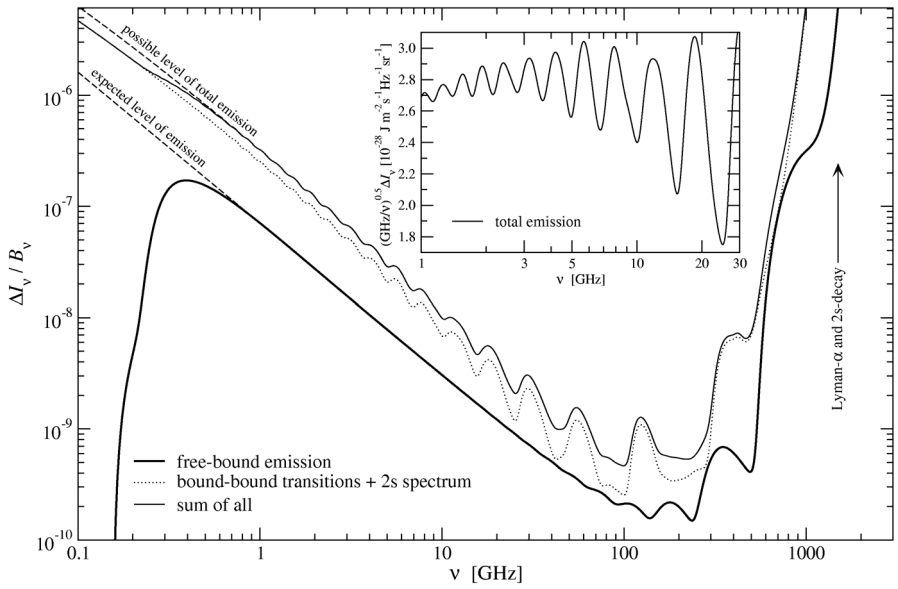

Figure 14: CMB spectral distortion due to hydrogen recombination relative to the CMB blackbody spectrum. The strongest distortion appears in the Wien part of the CMB blackbody spectrum and is due with the Lyman-α and 2s-1s two photon transition. At low frequencies the relative distortion exceeds the level of 10^{-7}.

2.1.1.2. Space plasma physics and Solar-terrestrial relations

1. Particle acceleration in solar flares

We have got evidences of prolonged and multiple particle acceleration at the Sun for the most powerful proton flares of 2003–2006 years studying their hard X-ray solar emission and proton fluxes in the interplanetary space. All cases of Anti-Coincidence System of Spectrometer on INTEGRAL (ACS SPI) count rate increases during solar flares were investigated. The ACS SPI is sensitive to primary and secondary γ-rays >150 keV and registers mainly primary solar hard X-rays and γ-rays during solar flares.

After a well-known solar flare on January 20, 2005 solar protons with energies >80 MeV propagated scatter-free to the Earth about first 30 minutes since their release into the interplanetary space and time-profiles of their intensity at the Earth were determined only by temporal and energetic characteristics of the solar injection function. The injection of 80–165 MeV protons started at 06:43 UT ±1 min and their injection function can be expressed as a product of the ACS SPI count rate (temporal dependence) and the proton spectrum ~ $E^{-4.7\pm0.1}$ (energetic dependence). The protons of higher energies were injected 4 min, but the relativistic electrons 9 min later, than that time. A close connection between high energetic solar electromagnetic emission and solar proton fluxes near the Earth is a strong argument in favor of the prolonged and multiple accelerations of protons in solar flares.

The impulsive phase of the three most intense flares of solar cycle 23 (October 28, 2003, January 20, 2005, and September 7, 2005) has been considered, these flares lasted about 20 min and consisted of at least three energy release episodes, which differed by their manifestation in the soft (1–8 Å, GOES) and hard (>150 keV, INTEGRAL) X-ray ranges as well as at radio frequencies of 245 MHz and 8.8 GHz. The protons and electrons were accelerated in each episode, but with a different efficiency; the relativistic protons were accelerated only after 5 6min of impulsive-phase development after the onset of a coronal mass ejection. We associate the record fluxes of protons with energies > 200MeV observed in the heliosphere in the September 7, 2005 event with effective particle acceleration at the end of the impulsive phase, when the hard X-ray intensity several folds greater than in two other flares has been measured.

2. Multi-component kinetic-continuum model of the solar wind interaction with the interstellar medium including the non-equilibrium of the pick-up ions.

The unique multi-component model of the solar wind interaction with the supersonic flow of the partly ionized hydrogen plasma of the interstellar medium is developed. This model includes the non-equilibrium of the solar wind pick-up ions, which are originated due to ionization of the interstellar atoms. Kinetic temperature of the pick-up ions is much greater then temperature of primary solar protons. This model is the generalization of the Baranov-Malama model (1993), in which the instantaneous assimilation of the pick-up ions was assumed. In this new model the pick-up ions as well as the hydrogen atoms are described kinetically. The following results were obtained in the frame of this model:

(1) in the nose region the thermodynamic non-equilibrium results in decrease of the thickness of the heliosheath (because of the increase of the heliocentric distance to the termination shock by 5 a.u. and decrease the distance to the heliopause by 12 a.u.)

(2) the distance to the termination shock increases by 70 a.u. in the tail

(3) the non-equilibrium leads to the smaller fluxes of the hydrogen atoms with the energy < 1 Kev and to the greater fluxes with the energy >1 Kev as compared with Baranov-Malama model.

The calculations in the frame of non-stationary kinetic gasdynamic model of the heliospheric interface were performed. Solar wind parameters at 1 AU measured by Wind and IPM 8 spacecraft were taken as the boundary conditions in these calculations. Consequently the temporal and spatial distributions of the plasma and hydrogen atoms parameters in the heliospheric interface and inside the heliosphere were obtained. These results were used for the calculations of the solar wind velocity and number density along the trajectory of the Voyager-2. Good agreement of the theoretical calculations with the data from the spacecraft Voyager-2 was shown in the periods from 1984 to 1995 and from 1999 to 2007.

The good agreement of the calculated solar wind velocity with the Voyager-2 data allows to estimate the number density of the interstellar hydrogen atoms in regions close to the termination shock: $n_{H,TS} \sim 0.1$ cm^{-3}.

3D kinetic-MHD model of the heliospheric interface has been developed. This model allowed to study the effects of interstellar magnetic field (IsMF orientation and magnitude on the structure of the heliospheric interface, and, in particularly, on the shapes of the heliopause and the heliospheric termination shock. It was shown also that the interstellar magnetic field leads to deflection of interstellar *H* atom flow direction inside the heliophere. This effect was also observed by SOHO/SWAN. The best agreement of the model results with the Voyager crossings of the heliospheric termination shock was obtained for IsMF magnitude of 3–3.5 μG and for $\alpha = 15$–30 degrees, where α is the angle between interstellar flow and IsMF direction.

The data of the scattered solar Lyman-alpha emission obtained from the spacecraft SOHO (SWAN instrument) in the period from 1996 to 2005 were compared with theoretical model calculations. This work has been done in collaboration with E, Quemerais and R. Lallement from Service d'Aeronomie (CNRS, France). The theoretical model includes: a) non-stationary model of the solar wind interaction with the local interstellar medium, b) model of the solar Lyman-alpha emission transfer including multi-scattering. The intensities of the solar Lyman-alpha emission obtained from the spacecraft SORCE (instrument SOLSTICE) were used for modeling of the hydrogen atoms distribution inside the heliosphere and intensities of the scattered emission. The spectra of scattered solar Lyman-alpha emission and the moments of the distribution function – the intensity of emission, the value of Doppler shift of the spectrum line and line width were calculated. It was shown that there is a strong difference between the theoretically and experimentally obtained intensities of the scattered solar Lyman-alpha emission. The time dependence of intensity also differs in theory and experiment. While there is good agreement between theory and data for the values of Doppler shift and line width. It means that the hydrogen atoms distribution function obtained in model agrees with the experimental data. The most probable reason of the discrepancy between theoretical and experimental intensities is connected with the ionization frequency accepted in model.

3. Investigation of middle and small-scale solar mind density structures

It was obtained by comparison of solar wind ion flux measurements with very high time resolution onboard spacecraft Interball-1 and WIND that sharp boundaries of small-scale density structures conserve their shape and conserve or decrease their durations during the solar wind propagation from L1 point to the Earth. Also for the solar wind dynamics on the large distances it was at the first time shown that shape and duration of sharp (shorter than 10 min.) boundary of the middle-scale density structure are conserved during its motion on the way 90 mln km (0.6 AU) from heliospheric probes Helios 1,2 to Earth's satellite IMP 8 (see the Figures)

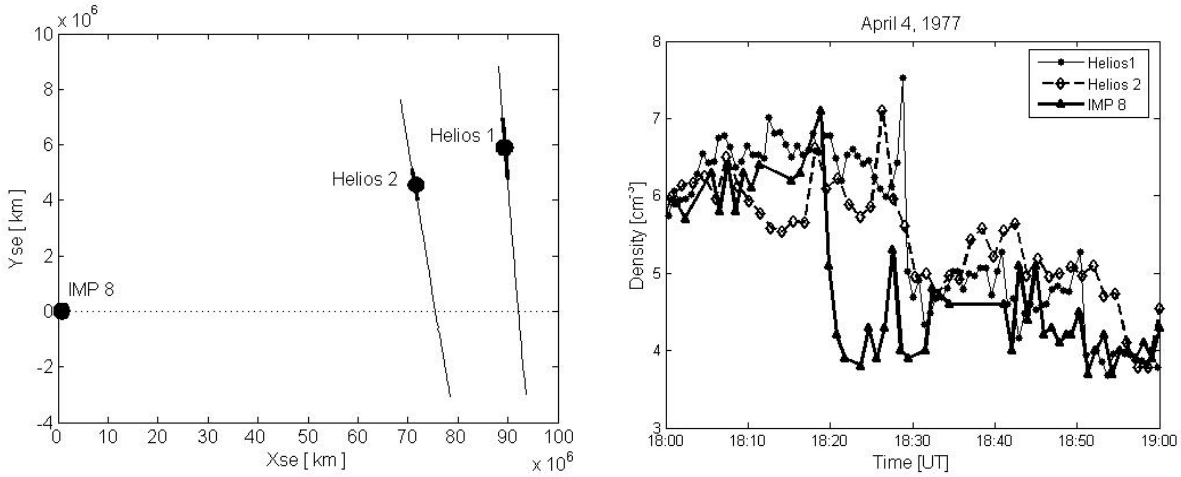

Using the large statistics of the fast solar wind measurements onboard Interball-1 in 1995–2000 was determined the probability distribution functions of ion flux fluctuations in the large range of scales from 10^{-5} Hz till 1 Hz. This study shows that for small time scales the large intermittency of fluctuations exists and it strongly increases with decreasing of time scale. Also this intermittency increase for solar wind intervals with sharp boundaries of plasma structures.

It was found that these sharp boundaries of solar wind density structures are mainly observed in the solar wind regions with increased density, low velocity and increased magnetic field amplitude.

It was performed on large statistics the correlation of the large and sharp changes of solar wind dynamic pressure with fast magnetic field variations in magnetosphere observed at geosynchronous orbits. The amplitudes of geosynchronous reply are proportional to the amplitudes of dynamic pressure changes. The geosynchronous reply is larger for the events with low magnetosphere compression before the solar wind pressure increase or decrease come to the magnetopause. The 3D MHD modeling of solar wind interaction with magnetosphere for investigated events are in rather well quality and quantitative coincidence with experimental data.

4. Statistical Investigation of Heliospheric Conditions Resulting in Magnetic Storms

On the basis of the OMNI database of interplanetary measurements we identified large-scale structures of solar wind (SW types) for all time intervals during 1976–2000. Our classification includes quasi-steady types: (1) Heliospheric current sheet (HCS), (2) Slow and (3) Fast SW streams, respectively, from closed and open magnetic field structures in the solar corona, and disturbed types: (4) Corotating interaction regions (CIR – compressed regions between slow and fast SW streams), (5) Sheath (compressed regions ahead of MC/Ejecta) and (6) Magnetic cloud (MC) and (7) Ejecta as well as (8) direct and (9) reverse interplanetary shocks (see catalogue on site ftp://ftp.iki.rssi.ru/pub/omni/).

The main interplanetary sources of magnetic storms are magnetic clouds including body of magnetic cloud (MC) and compressed region before it (Sheath) and CIRs which include southward component Bz of interplanetary magnetic field (IMF). Properties of solar wind resulting in 623 magnetic storms during 1976-2000 have been studied separately for Sheath, MC and CIR. The analysis is carried out by the superposed epoch technique (the magnetic storm onset time is taken to be the beginning of an epoch) for five various categories of storms induced by various types of solar wind: CIR (121 storms), Sheath (22 storms), MC (113 storms), "uncertain type" (367 storms) and all 623 events. Though the lowest values of the *B*z -component of IMF are observed in the MC, the lowest values of the *D*st-index are achieved in the Sheath. Thus, the strongest magnetic storms are induced, on average, during the Sheath rather than during the MC body passage, probably owing to higher pressure in the Sheath. Higher values of *nkT* , *T*/*T*exp, and beta-parameters are observed in the CIR and Sheath and lower ones in the MC, which corresponds to the physical essence of these solar wind types. The growth of variations (hourly standard deviations) of the density and IMF magnitude was observed 5–10 hours before the onset only in the Sheath. For the CIR-, Sheath- and MC-induced storms the dependence between the minimum of the IMF *Bz*-component and the minimum of the *Dst*-index, as well as the dependence between the electric field *E*y of solar wind and the minimum of the *Dst*-index are steeper than those for the "uncertain" solar wind type. The steepest *Dst* vs.*B*z dependence is observed in the Sheath, and the steepest *Dst*.vs.*E*y dependence is observed in the MC.

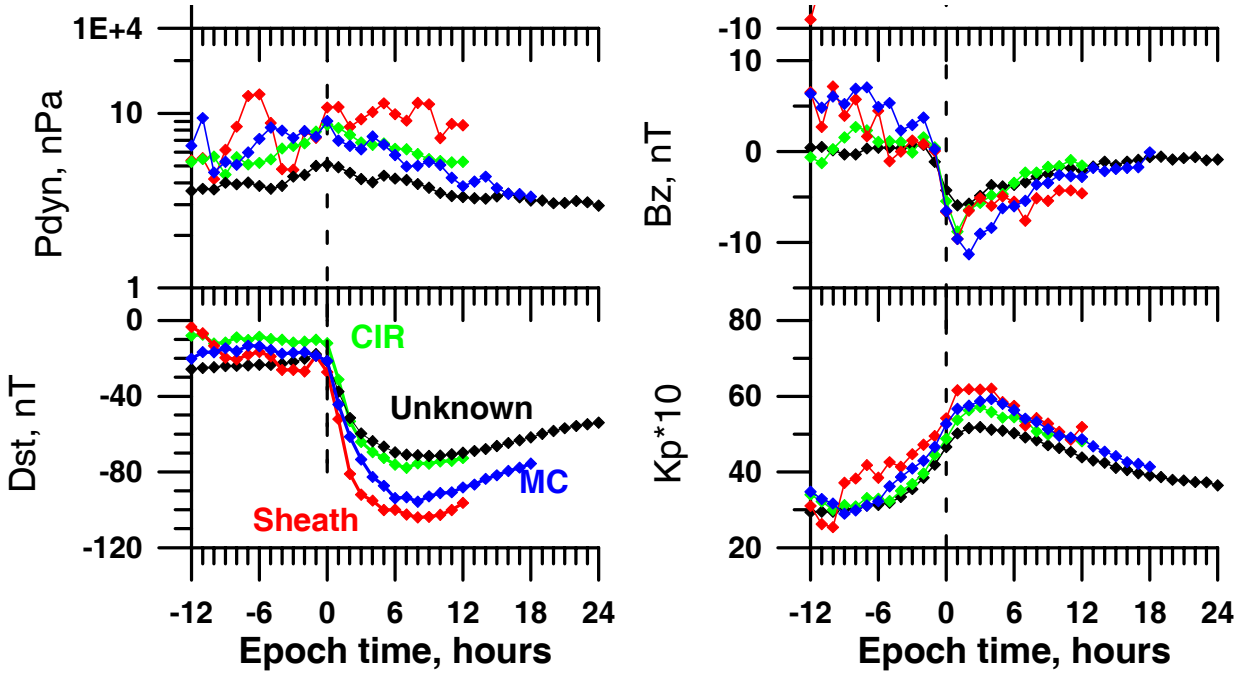

Figure. Temporal variations of parameters of solar wind and interplanetary magnetic field for 623 magnetic storms during 1976-2000 obtained by the superposed epoch technique on the basis of OMNI data for different types of solar wind: Sheath, MC and CIR.

5. Peculiarities of transport properties at magnetospheric boundaries: Implication of electric field and nonlinear magnetic barriers

For the first time from CLUSTER data we demonstrate a difference between the ion flow and cross-field plasma drift being due to ion finite-gyroradius effect. Also displayed is plasma acceleration by the inertial drift in non-uniform electric field at the thin (~ proton gyroradius) magnetopause. Comparison with similar Interball-1 data shows that such processes are the characteristic ones for the proton scales at boundaries of streaming plasmas. It represents a new type of the plasma transport across such boundaries and it provides the combined plasma heating in the non-uniform electric field with superimposed magnetic turbulence. The combined effect of electric and magnetic forces inside current sheets without magnetic reconnection, results in the solar plasma inflow and in ion effective temperature rise just inside the high- latitude magnetopause. Simultaneously deeper in the magnetosphere, the boundary layer flows can originate both from direct penetration across the cusp and from dayside reconnection sites. Thus, the experiment is clarifying a dilemma, which looked to be the unresolved one: if magnetic reconnection or a diffusive process provides the main contribution in the plasma inflow inside magnetosphere. Generally, their inputs occur to be comparable!

Our study of the nonlinear micro-structure influence on boundary layers between moving plasmas, surprisingly demonstrated that at the boundaries 3D disturbances in the incident flow can result in an overturn of the magnetic field lines, i.e. to Alfvenic collapse of the magnetic field, which generates thin magnetic barriers between the moving plasmas. Conversely to the previous finding dealing with magnetic field rarefactions, it infers a new mechanism for magnetic field concentration, serving to separate moving plasmas.

We generalize the Alfvenic collapse concept to the finite gyroradius limit, that leads to prediction of an equilibrium plasma flux at about ion thermal speed near the magnetic barrier boundaries, having scales comparable with ion gyroradius. And really, we find such thermal fluxes namely close to the micro-barrier with the dominant magnetic pressure both from Interball-1 and Cluster data. Unexpectedly, the specific boundary layer, steaming at about ion thermal speed between stagnant and super-sonic plasmas, with imbedded micro-barriers can be quasi-stationary throughout one Earth radius during about one hour.

6. Studies of the Earth's magnetopause shape.

It is revealed that the magnetopause of the Earth is ~5 % compressed in the directions perpendicular to the plane formed by solar wind velocity and interplanetary magnetic field vectors. This compression can results from the stress of the magnetic field lines draping the magnetopause. The influence of B_z component of the interplanetary magnetic field on the subsolar magnetopause position was not found in Prognoz's and Interball 1 data. The cross-section of the magnetopause by *Y*, *Z* plane of the GIPM reference frame is decreasing with

increase of solar wind ram pressure ρV^2. The ratio of R_{zGIPM} to R_{yGIPM} axis of cross-section approximating ellipsoid is about ~0.95 under all ρV^2 conditions.

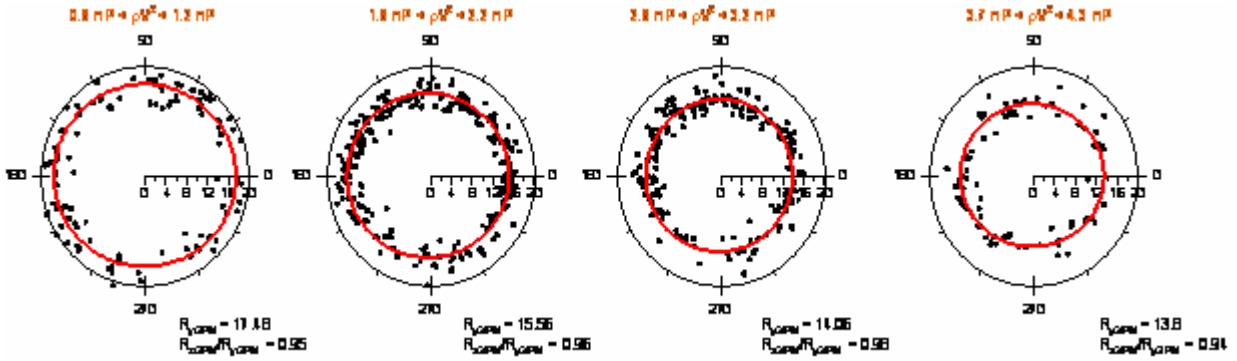

7. Experimental studies of the accelerated ion beams observed in the Plasma Sheet Boundary Layer of the Earth magnetotail by Cluster spacecraft.

Multipoint measurements of accelerated field-aligned ion beams (beamlets) performed by Cluster spacecraft in Plasma Sheet Boundary Layer (PSBL) allow to distinguish spatial and temporal effects in beamlet observations and to estimate, for the first time, their minimum duration and characteristic spatial scales. It has been revealed that beamlets represent plasma filaments elongated along the lobe magnetic field lines (~ tens of Re, where Re is the Earth radius) and strictly localized in the direction perpendicular to the magnetic field (< 1Re). The minimum duration of beamlets is about 10 min. It was also found out that the magnetic tubes containing beamlet ions are bended and, as a result, beamlet has «snake-like» spatial structure.

We performed the analysis of magnetic disturbances of the lobeward boundary of PSBL during the intervals of beamlet propagation. The analysis was based on the database containing all PSBL crossings by Cluster spacecraft during the period from 2001 to 2003 (at the distances from the Earth ~19Re). These disturbances caused the increasing of the energy of cold lobe plasma population moving tailward from the ionosphere. It was shown that the magnetic disturbances of the PSBL boundary may be caused by the Kelvin-Helmholtz instability arising due to the strong velocity gradient during the intervals of high-velocity ion beamlet propagating earthward. The magnetic disturbance of PSBL boundary propagates earthward with Alfven velocity and together with the flapping contribute to the oscillation motions of PSBL.

8. Thinning and stretching of the Earth's magnetotail plasma sheet before substorms

Cluster multisatellite project allowed to determine routinely structure of the current sheet in the Earth's nightside plasma sheet with a direct observations. Often observed during 2001–2004 years prolonged crossing of the thinning current sheet

in the course of the substorm growth phases were used to establish typical scenarios of thinning and stretching of the plasma sheet.

It was shown, that the sheet thinning (increase of the current density Jo) is inversely proportional to normal (Bn, Bz) component of local magnetic field (that is to stretching) and proportional to ion temperature. Sheets with dominating shear (By) component of the local magnetic field comprise of the order of 30% of observations and are characterized with a clear non-Harris profile with relatively narrow current density maximum in the center of the sheet.

The sheet scenarios of thinning-stretching are show on the plot. Only the first and last points of each interval are shown. On the horizontal axes — maximum current density and estimate of thickness.

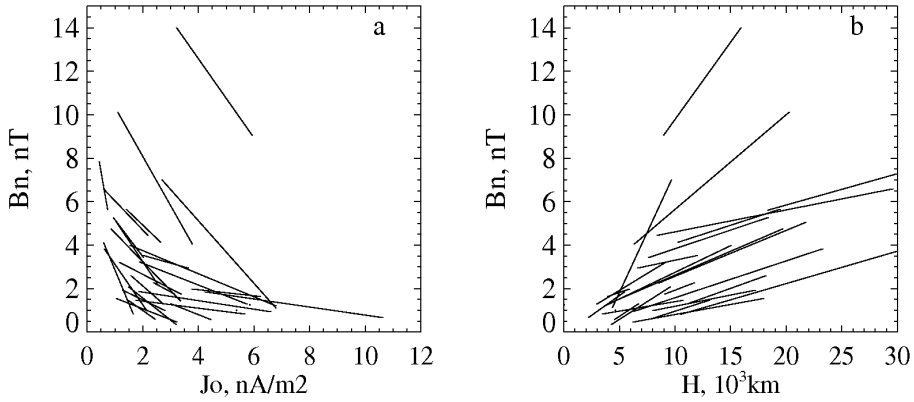

9. The modeling of plasma systems in the magnetotail

The analytical self-consistent model of multicomponent current sheets is presented where plasma consists of both solar wind and ionospheric ions. The influence of the electron population is taken into account in the form of quasi-equilibrium Boltsmann distribution in the electrostatic field, where electrons support the current with sharp peak in the center of current sheet. The contribution of heavy ions O^+ is taken into account in one of the item in Grad-Shafranov system of equations, describing an equilibrium configuration. It is shown that the contribution of oxygen ions across the magnetotail can not exceed 30 % in real conditions, but positive "wings" of current density supported essentially by O^+ ions lead to substantial thickening of current density profile. Very narrow electron sheet with thickness about $L \sim (0.05–0.1)\rho_L$ (where ρ_L is the proton gyroradius) is embedded inside thin proton sheet with $L \sim \rho_L$, which in its turn is embedded inside relatively thick oxygen current sheet ($L \sim (5–10)\rho_L$). Moreover, the whole current sheet is embedded inside more thick plasma sheet (its thickness in the model is equal to infinity but in real magnetosphere it might reach the scale from several to ten R_E, i.e. substantially lager than the thickness of current sheet). Therefore the model, presented here allows considering 4 levels of embedded plasma structures that is a reason of its name "matreshka model".

10. Investigation of the mechanism of relativistic electron precipitation bursts from the outer region of the radiation belt

Observations of particle precipitation into the Earth's atmosphere performed on low-altitude satellites have excited substantial interest in relativistic electron precipitation bursts from the outer zone of the radiation belt. As underlying mechanism of such bursts, we suggest particle scattering into the loss cone due to higher-order cyclotron resonance interaction between relativistic electrons and intense narrow-band upper hybrid waves, which are frequently observed outside the plasmapause.

Two cases have been considered: the case of a quasi-monochromatic wave, and the case of a wide spectrum. For both cases, particle diffusion coefficients in the phase space have been calculated with the account of plasma and the ambient magnetic field inhomogeneity. We show that relativistic electrons have a preference over lower energy electrons from the viewpoint of the number of cyclotron resonances that a particle crosses during each bounce period.

Due to predominantly longitudinal direction of the upper hybrid wave group velocity, the resonant wave-particle interaction can take place over many electron bounce periods, which facilitates the particle scattering into the loss cone.

The developed theory accounts for two main features of the relativistic electron precipitation bursts, namely, a strong energy dependence in the electron precipitation process and the small-scale burst structure, which is primarily attributed to the localization and strong inhomogeneity of the growth region of the upper hybrid modes responsible for the scattering.

11. Electric field shielding in the inner magnetosphere and plasma convection depending on plasma density and temperature at the outer boundary

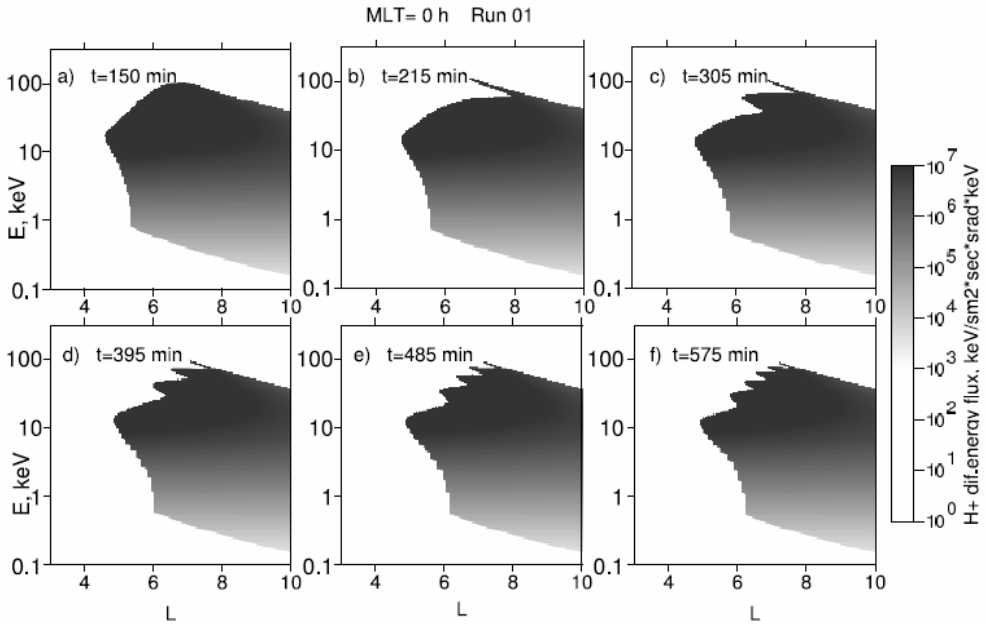

With the help of the self-consistent model of electric field in the inner magnetosphere maps of electric potentials and field-aligned currents are calculated. The shielding effect for different values of proton temperature (1.5–15 keV) and density (0.2–1 cm^{-3}) at the outer boundary substantially depends on MLT. Due to higher dayside ionospheric conductivity shielding is weaker at dayside. Increase of conductivity due to auroral precipitation also affects shielding in the same way. Shielding depends more on density, than on temperature. Structure of electric field and shielding boundary are more complicated in such models in comparison with analytical approximations such as Volland-Stern models. Plasma convection inside the magnetosphere also depends on history of the cross-polar cap electric potential changes. The well known “nose structures” in ion spectrograms appear after a potential reduction. The higher is density at the boundary, the stronger is shielding and therefore typical L-shell of “nose” formation is larger. On the picture formation of the multiple nose structures after a sequence comprising (1) a 30 min increase of potential; (2) 60 min constant potential; (3) 30 min decrease of potential. The formed “nose” structure are likely of the same nature as the drift echo.

12. The study of the nature, properties and the origin of Fine Dispersion Structures (FDS) in energetic particle spectra

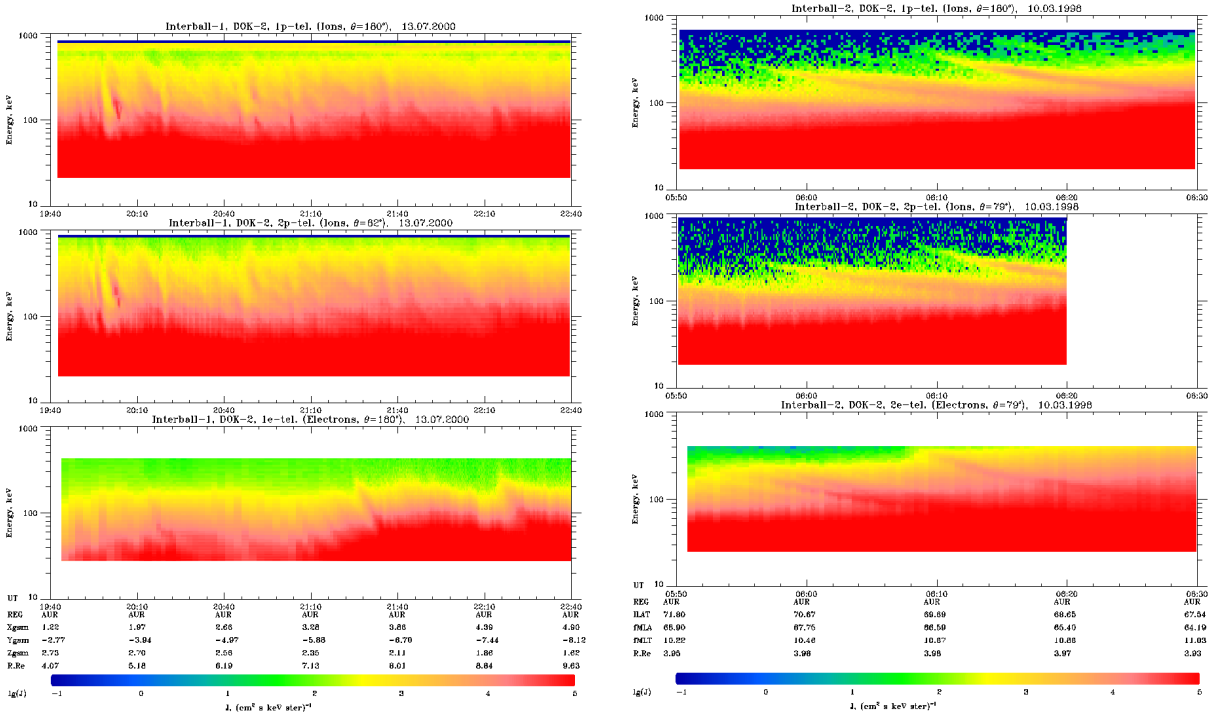

Fine Dispersion Structures (FDS) in energetic ion and electron spectra in the outer magnetosphere were discovered in the DOK-2 experiment onboard Interball-1 and -2 spacecrafts (1995–2000). In total more then 1000 FDS events were observed. Two types of FDS were observed: 1) short duration (<5 min) events and 2) long

duration (>5 min) events. It was shown that the first one's observed in the night side magnetosphere, have a "time-of-flight" character and correspond to particles arriving from the geotail after their impulsive acceleration in the plasma sheet. Simulations of particle motion in model magnetic fields showed that the majority of these particles return back to the plasma sheet after reflection from the outer magnetosphere. But the small part (<1%) can be captured in the closed field line region, start a gradient-curvature drift around the Earth and are responsible for "long" FDS's. While the average observation frequency of "long" FDS's is 0.17 per hour they can make several turns around the Earth and even a single event can give an essential addition to the total energy density (54–52 %) and total energy flux (67–66 %) of particle population in the outer magnetosphere. Below are shown examples of spectrograms for two types of FDS events: left — "short" ("time-of-flight" dispersion), right — "long" (gradient-curvature drift dispersion).

2.1.2. V.N. PUSHKOV INSTITUTE OF TERRESTRIAL MAGNETISM, IONOSPHERE AND RADIOWAVES PROPAGATION OF THE RAS

2.1.2.1. CORONAS-F: Solar and Solar-Terrestrial Physics

The processing of data obtained on board the CORONAS-F mission in the period of its orbital operation in 2001-2005 was continued during 2007-2008. CORONAS-F observed the Sun and recorded the manifestations of solar activity in the Earth's space environment.

Helioseismic Experiment DIFOS/CORONAS-F

Helioseismic data obtained with the DIFOS/CORONAS-F instrument have been used to demonstrate the potentialities of the newly developed method for processing the observation time series with the aim of determining the precise mean frequencies of the split lines of p-modes of the global solar oscillations and studying the origin of nonrotational splitting in the p-mode oscillation spectrum.

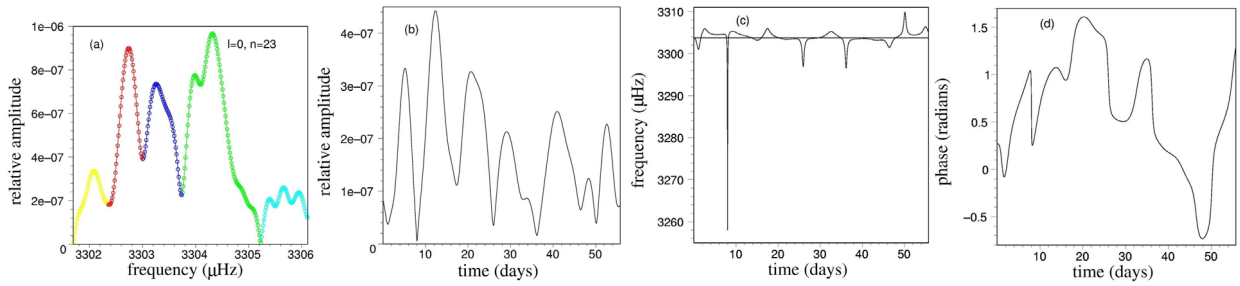

Figure 1: (*a*) Splitting of the line profile of the global p-mode ($l = 0$, $n = 23$) in the components shown by different colors. (*b*, *c*, *d*) Instant amplitude, frequency, and phase of the p-mode as a function of time.

Precise determination of the p-mode frequencies is the main goal of the global helioseismology. The accuracy of determining the frequency defines the accuracy of solution of the inverse problem. To solve this problem, ground-based observational networks and space stations have been created for continuous monitoring of the Sun, since the accuracy of the frequency measurements depends on the duration of observations. However, it was revealed that the spectral lines of the p-mode oscillations were subject to splitting that had no connection with the solar rotation. As a result, measuring the line frequencies involves certain difficulties. Various averaging methods have been used, but they yield incongruous

results. Thus, the efforts made to develop a system of continuous observations were not properly rewarded. A new method of the time series analysis has been developed and tested using the CORONAS-F/DIFOS data. The method is a generalization of the concept of the analytical signal. It permits finding the instant amplitude, phase and frequency of the signal, as well as estimating separately the contribution of the amplitude and frequency fluctuations to the line broadening.

Figure 1 illustrates the results of processing the CORONAS-F/DIFOS data by the method proposed above. A two-month series of observation of the brightness fluctuations in the wavelength range of 350 nm has been analyzed. Fig.1a shows the nonrotational splitting of the spectral line of the global p-mode with $l = 0$. The beats due to the occurrence of the line components result in time variations of the amplitude (Fig. 1b). Spikes of the instant frequency (Fig. 1c) occur at the amplitude minima to confirm that the amplitude variations are produced by the component beating. Spikes of the instant frequency manifest the phase jumps at the amplitude minima. The analytical signals obtained for each line component are shown with different colors in Fig. 1a. The instant amplitudes, frequencies, and phases of the line components are shown in Figs. 2a, b, c. The occurrence of the frequency spikes and phase jumps suggests that the line components consist of subcomponets, which are unresolved because of insufficient length of the time series. The variances of the amplitude and frequency fluctuations of the line components, as well as the variances of the entire spectral line are shown in Fig. 2d. In all cases, the variance of amplitude exceeds that of frequency by a factor of 10–100; i.e., the line width depends entirely on amplitude fluctuations, while the p-mode frequencies are very stable. Thus, the new method for analyzing the time series permits us to find the mean frequency of the split spectral line of the p-mode with a high degree of accuracy. Unusual features of the line components have been revealed that are hard to explain in terms of the theory of stochastic excitation of p-mode oscillations of the Sun.

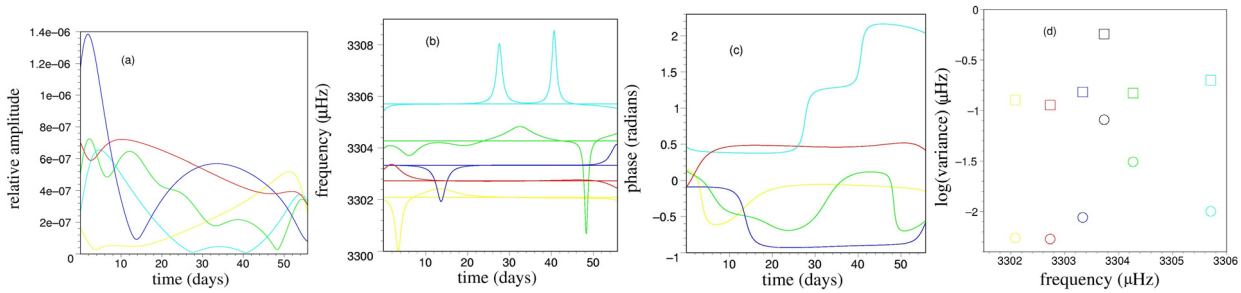

Figure 2: (*a*, *b*, *c*) Instant amplitudes, frequencies, and phases of the line components marked with different colors in Fig. 1a. (d) Variances of the amplitude (squares) and frequency (circles) fluctuations of the line components. Variance of the amplitude and frequency of the entire line is marked black.

CORONAS-F/SPIRIT experiment results

Monochromatic solar X-ray images were obtained in the SPIRIT experiment on board CORONAS-F satellite. Spectroheliograph Mg XII of the SPIRIT apparatus, which utilized bend crystal mirror, registered monochromatic images in spectral line $\lambda = 8.42$ Å (resonance line of H-like ion Mg XII). The emission of the spectral line is formed under relatively high (for solar corona) temperatures $T > 5$ MK. Thus, Mg XII spectroheliograph allowed for the first time to obtain direct images of hot (flare) solar plasma free from emission of colder plasma of quiet sun.

A comprehensive study of solar flare events based on soft X-ray (SXR) monochromatic Mg XII images as well as SXR flux have been carried out. New data about important characteristics of solar flare plasma – electron temperature, density, their spatial and temporal distributions was obtained. The methods are based on monochromatic X-ray images $\lambda = 8.42$ (SPIRIT) and simultaneous X-ray fluxes in relatively wide spectral ranges 1–8 Å and 0.5–4 Å (measured on GOES). Also, solar hard X-ray measurements obtained on RHESSI were used to verification of the developed methods.

The method for determination of temperature distribution (Differential Emission Measure) is based on flux intensities in different SXR spectral ranges. The data for 8.42 Å spectral line (SPIRIT) and two wide-band ranges 1–8 Å and 0.5–4 Å (GOES) were used. The method has been applied for reconstruction of DEM temporal profile during February 2002, when the SPIRIT data was obtained with high cadence (1.5 min). It was shown, that during long-last flare events considerable amount of flare plasma has relatively low (for flaring plasma) – 1-4 MK and moderate 4–10 MK temperatures (Fig. 3).

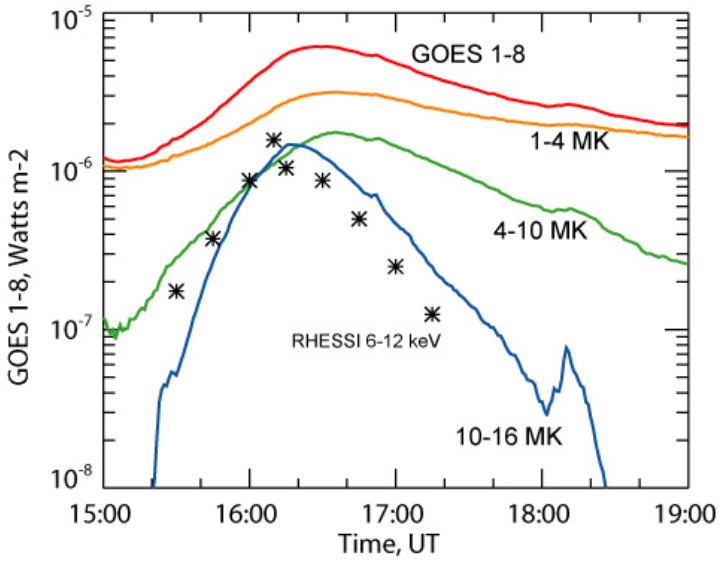

Figure 3: Flux temporal profile measured on 26th Feb 2002 by GOES 1–8 Å (red line) and its distribution to emission fluxes of low-temperature (orange line), mid-temperature (greed line) and hot-temperature (blue line) plasma. Asterisk – normalized flux measured by RHESSI 6– 12 keV X-ray channel.

Monochromatic images and simultaneous DEM distribution were used for modeling of spatial T_e and n_e distributions in flare plasma region. Long-last flare event of 26th Feb 2002 was modeled under assumption spherical symmetry (as suggested by corresponding SXR Mg XII image). The flare had relatively hot core with temperature ranging from 5 up to 16 MK, with the density being increased slightly – from $1.5 \cdot 10^9$ cm^{-3} in the periphery to $2.5 \cdot 10^9$ cm^{-3} in the center.

Temporal DEM profiles, obtained with the SXR flux data, were used to overlay monochromatic Mg XII and hard X-ray RHESSI images (Fig. 4). The composed image allowed to determine boundaries of hot plasma and ultimately check the spatial modeling of T_e and n_e distributions.

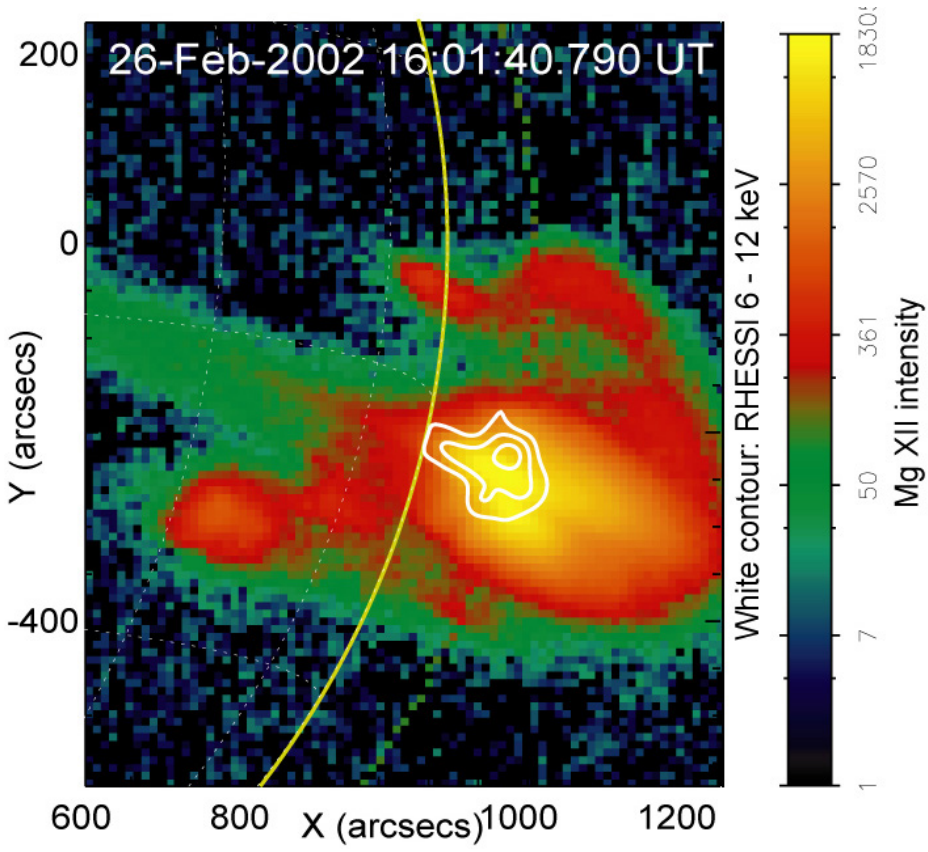

Figure 4: Mg XII image overlaid with RHESSI 612 keV contours.

The obtained information about density and emission measure could be used to test different heating model for flare plasma. It was shown that high amount of cold plasma during the flare and low density in it's core are in accordance with fast shock wave heating and thin target models.

High-temperature plasma in the solar corona

During a solar flare, the impulsive release of energy stored in the magnetic field efficiently accelerates particles and heats the plasma. Observations carried out

using the SXT telescope onboard the Yohkoh satellite (Masuda et al., 1994; Tsuneta et al., 1997) have shown that a hot plasma can be produced during flares in both the chromosphere and the solar corona. Currently, the spatial and temporal parameters of the high-temperature coronal plasma are studied with the RES-K X-ray spectroheliograph, which is part of the SPIRIT complex operated onboard the CORONAS-F satellite (Oraevsky et al., 2002). The RES-K spectroheliograph provides monochromatic images of the full solar disk in the Mg XII 8.42 A line with a temperature of $T = 5–15$ MK (Zhitnik et al., 2003). This makes it possible to directly observe the hot coronal plasma, whereas the data of the Yohkoh satellite can be used to reveal the high-temperature plasma only indirectly, by comparing SXT images obtained with various filters. We study here the structure and dynamics of the hot coronal plasma during solar flares and between them based on RES-K observations in the Mg XII line.

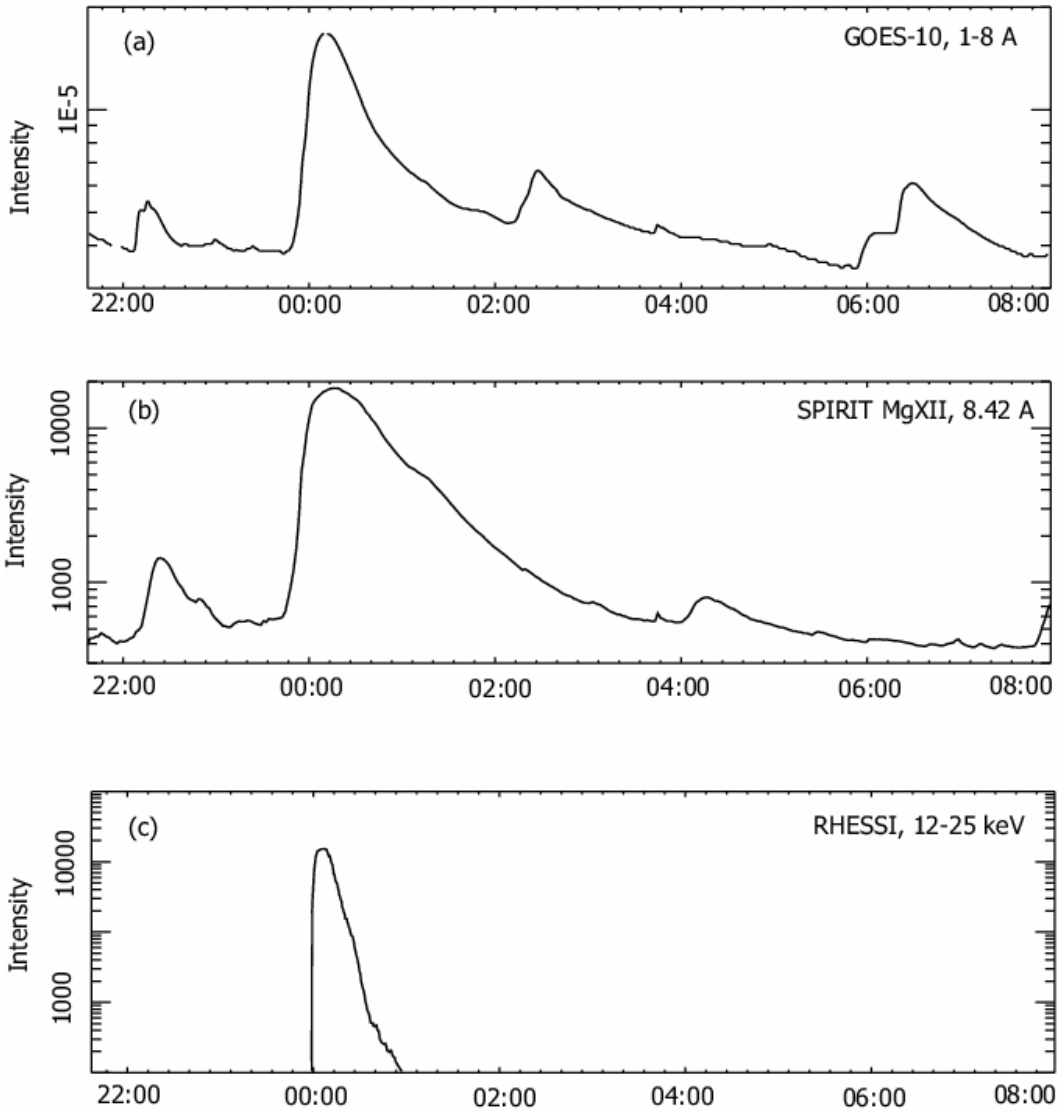

Figure 5: Time profiles of emission: (a) integrated solar emission in the 1-8 A range according to GOES data; (b) MgXII 8.42 A emission of the high-temperature plasma in the core; and (c) hard X-ray emission of the flare in the 25–50 keV range according to RHESSI data.

The SPIRIT instrumentation onboard the CORONAS-F satellite is designed to obtain full-disk images of the Sun in soft-X-ray and extreme-UV spectral channels and lines (for a technical description of the SPIRIT instrumentation, see Zhitnik et al., 2003). We analyze the series of successive images of the NOAA 9830 active region that was obtained using the RES-K spectroheliograph in the Mg XII 8.42 A channel from 21:40 UT on February 21, 2002, to 08:00 UT on February 22, 2002, during a period approximately coincident with a flare of class M4.4, according to the GOES (Geostationary Operational Environmental Satellite) scale. Figure 5 shows a time profile of the Mg XII emission obtained by integrating the emission of all fragments, together with the simultaneous emission curves obtained in the 25–50 keV range onboard the RHESSI (Ramaty High Energy Solar Spectroscopic Imager) satellite and in the 1 to 8 A range onboard the GOES satellite. The profile of hard X-ray emission should correlate with the injection rate of accelerated electrons.

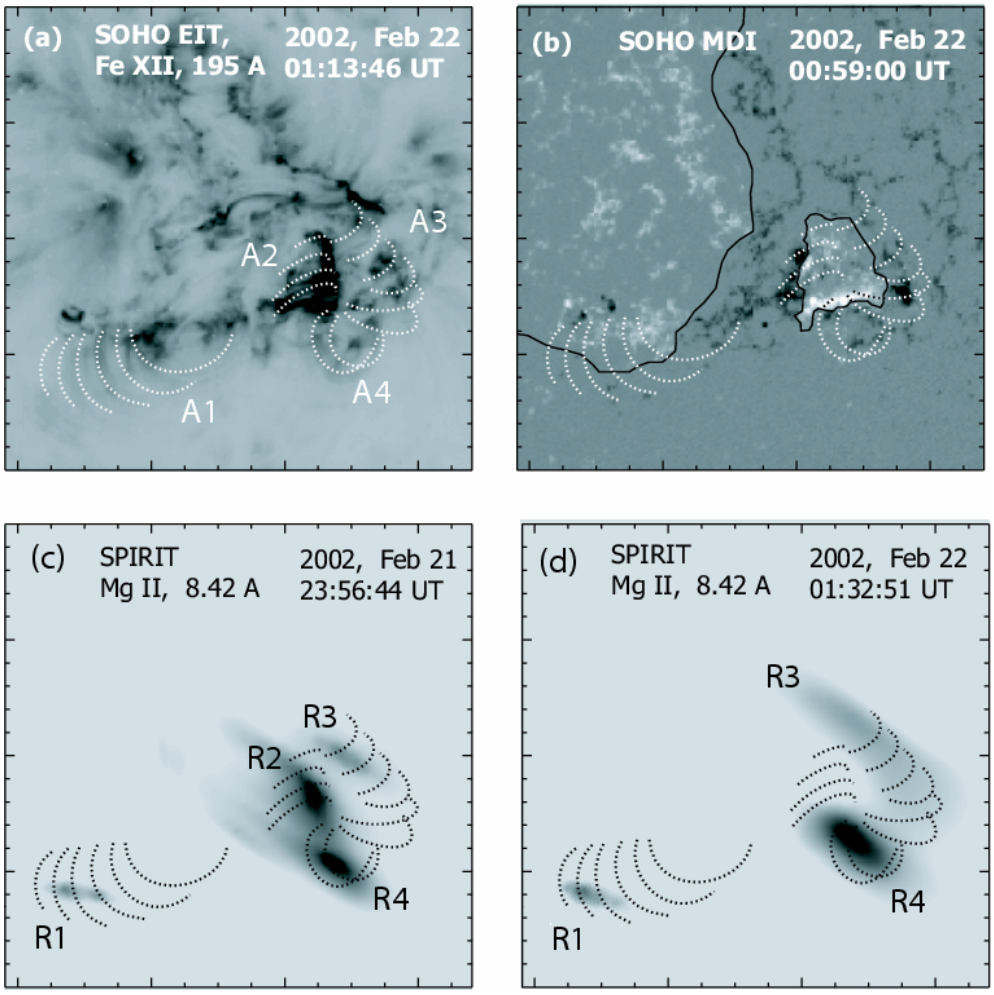

Figure 6: Active region NOAA 9830: (a) SOHO/EIT image in the 195 A line; (b) SOHO/MDI magnetogram and the schematized neutral line of the photospheric magnetic field; (c) location of high-temperature-plasma sources (R1–R4) before the flare (SPIRIT image in the MgXII 8.42 A line); and (d) distribution of high-temperature plasma after the flare. The loop systems observed on the TRACE satellite are marked with dotted curves and A1–A4 symbols.

The structure of the active region in the photosphere and corona is shown in Fig.6 by images in various emission ranges. All these images are reduced to the same scale and, in addition, compensation for their displacement due to solar rotation is applied. Upon analyzing the SOHO/EIT and TRACE images, we selected four groups of magnetic loops, which are denoted in the figure as A1–A4. In the bottom panels, these loop systems are superimposed onto the pattern of high-temperature emission sources that we detected in the Mg XII SPIRIT images. A comparison between the panels in Fig.6 shows that the location of hot-plasma regions observed in the Mg XII line corresponds to systems of coronal loops, and the plasma-emission intensity is maximal near the apices of the loops.

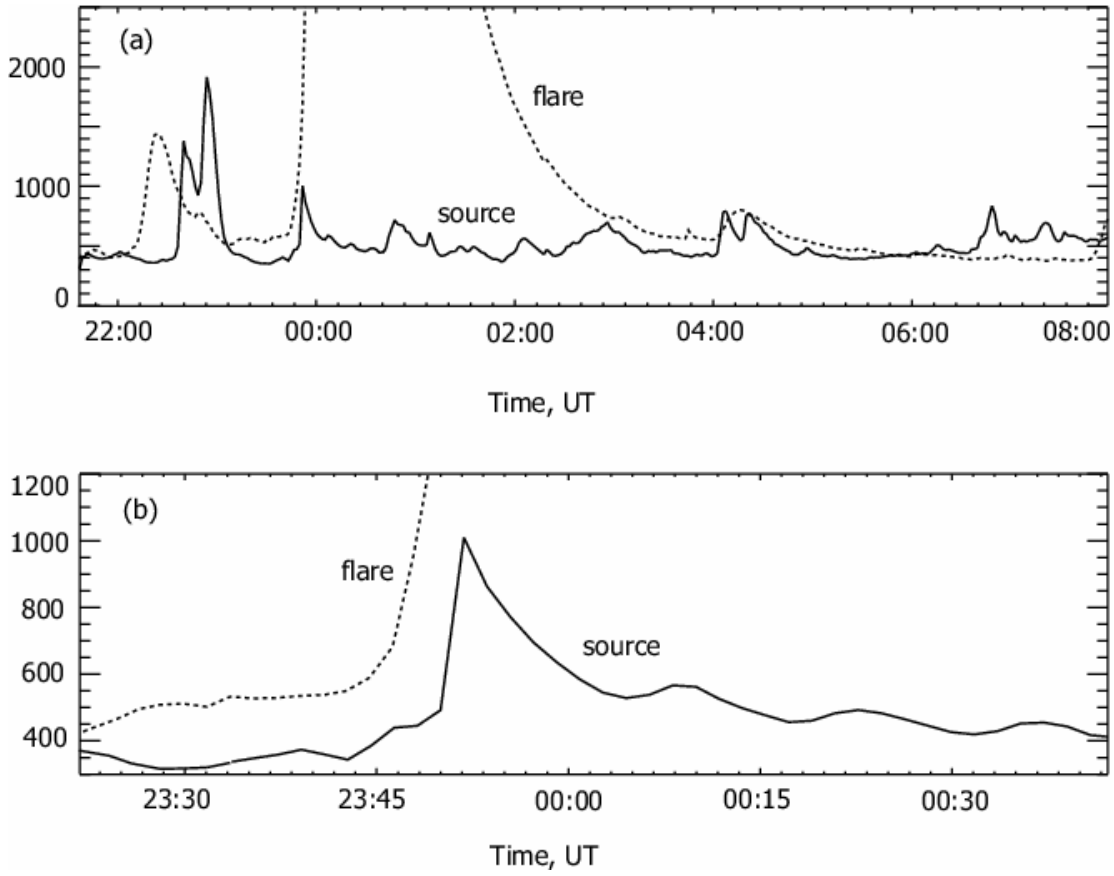

Figure 7: Comparison of the emission profiles of high-temperature plasma in the core of the flare (dotted curve) and in the distant source R1 (solid curve).

During the considered series of SPIRIT observations, a class~M4.4 flare occurred. Its onset in the Mg XII line was observed at about 23:45 UT in core R2, whose position is shown in Fig. 6. At the time of the flare, cores R2–R4 merged into one in the SPIRIT images, which prevented separate study of the dynamics of each of them. Core R1 was at a large distance from the flare center and could be identified in the images as a separate emission source even at the flare maximum. Fig. 7 shows time profiles in the R2–R4 flare area (dashed) and in the distant core R1 (solid). It is remarkable that the time profiles exhibit a correlation, which can be

noted at many intervals. In particular, some time after the onset of the flare (dashed curve), an emission outburst was also observed in the distant core R1, although it was weaker. Based on the time delay of the second outburst, 5 min, and the distance between the cores, 2105 km, the speed of the disturbance propagation from the center of the flare can be estimated to be 650 km/s.

References

Masuda, S., Kosugi, T., Hara, H., et al., Nature, Vol. 371, 495, 1994.

Tsuneta, S., Masuda, S., and Kosugi, T., ApJ, Vol. 478, 787, 1997.

Oraevsky, V.N. and Sobelman, I.I., Astron. Lett., Vol. 28(6), 401, 2002.

Zhitnik, I.A., Bugaenko, O.I., Ignatiev, A.P., et al., MNRAS, Vol. 338, 67, 2003.

EUV corona

The SPIRIT telescope aboard the CORONAS-F satellite (in orbit from 26/07/2001 to 05/12/2005), for the first time observed the solar corona in the 175 Å (Fe IX, X and XI lines) and 304 Å (He II and Si XI lines) bands in the coronagraphic mode at the distance of 1.1-5 R_{sun}. This intermediate region between the fields of view of ordinary extreme-ultraviolet (EUV) telescopes and most of white-light (WL) coronagraphs is very important for forming the streamer belt, acceleration of ejected matter and emergence of slow and fast solar wind.

The results of continuous coronagraphic EUV observations in June and December 2002 has shown that in the 175 Å band (Fe IX-XI lines) the corona contained a diffuse quasi-symmetric part and a structure of bright rays (radial or non-radial, features 1 and 2 in Fig.8) started from the solar surface. Some very bright rays were evidently originated from the active regions and possibly revealed the solar wind streams (feature 4 in Fig.8). Several big rising loops (e.g. feature 3 in Fig.8) were associated with the CME in the LASCO catalogue.

In 304 Å the corona is more diffuse and inhomogeneous. Only traces of the coronal rays seen in 175 Å are faintly visible. The analysis of radial distribution of the He II coronal brightness has shown that up to distances of 1.34-1.5 R_{sun} this radiation is excited by collisions (as for the coronal lines), but at greater distances the resonance scattering becomes dominant.

Reference

V.Slemzin, O.Bougaenko, A.Ignatiev, S.Kuzin, A.Mitrofanov, A.Pertsov, I.Zhitnik. Off-limb EUV observations of the solar corona and transients with the CORONAS-F/SPIRIT telescope-coronagraph. Ann. Geophys., 26, 1–10, 2008.

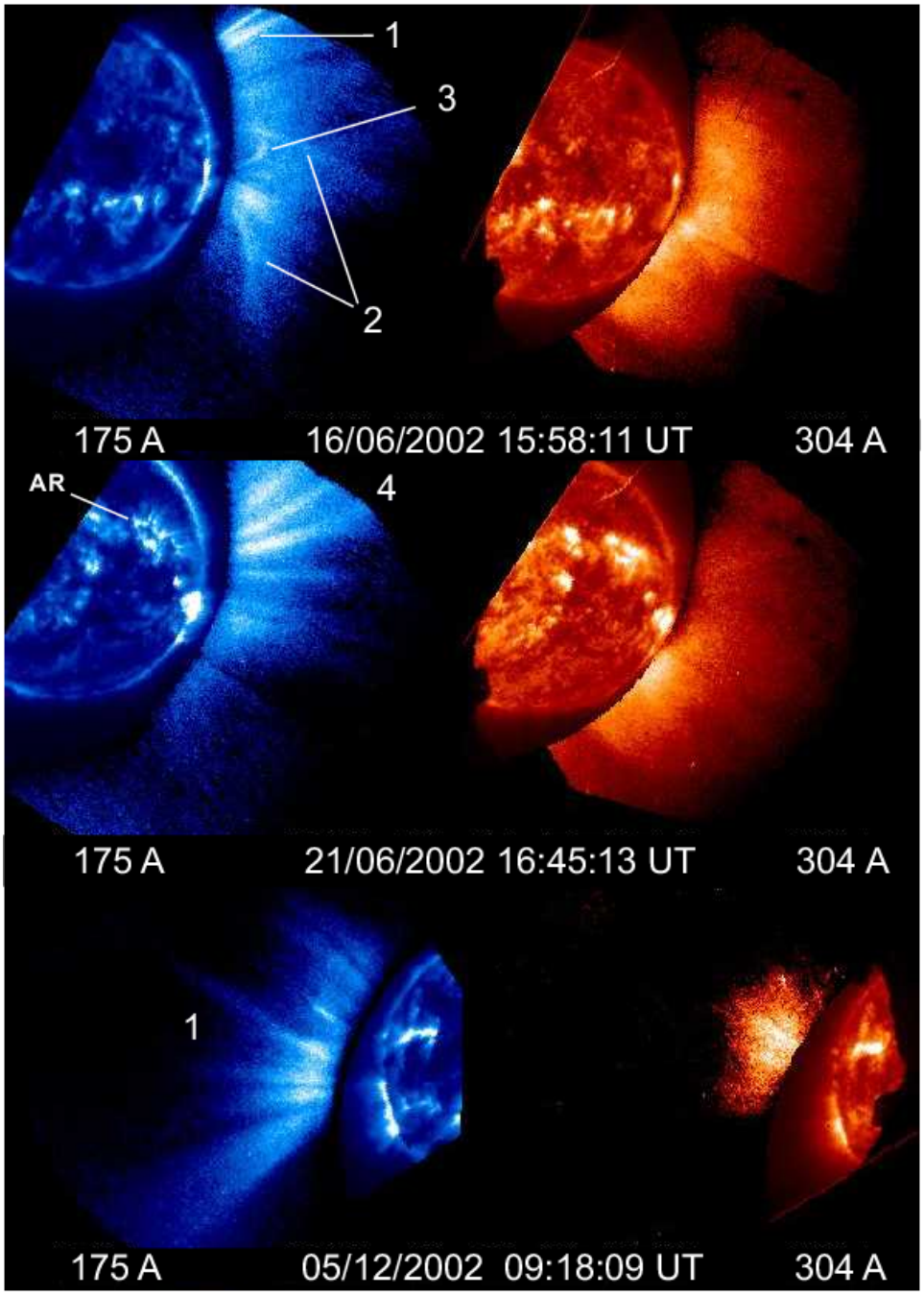

Figure 8: Specific coronal features observed by the SPIRIT EUV coronagraph in the 175 and 304 Å bands: 1 — radial rays, 2 — non-radial rays, 3 — a rising loop, 4 — a fan of rays linked with the active region at the disk (solar wind streams).

Dynamics of solar flares hard X-ray emission spectra according to the data IRIS/CORONAS-F

The data obtained with the IRIS/CORONAS-F instrument have been used to study the dynamics of the energy spectra of the hard X-ray emission from solar flares of different importance. As a result, time variations have been revealed in the shape of the spectra, which reflect variations in the distribution function of the flare-

accelerated electrons. The high-sensitivity flare X-ray spectrometer IRIS allowed a detailed study of the spectral and time characteristics of soft X-rays (2–15 keV) from major and minor solar flares, as well as from the quiet Sun, when the emission intensity did not exceed ~10^{-5} erg $sm^{-2}.s^{-1}$ (~10 nW/m^2). The evolution of the X-ray energy spectra was studied using the 64-channel instrumental spectra (2–150 keV) obtained with a time resolution of 1 s. Shown below are the results of the analysis of the X-ray spectrum dynamics for four solar flares of importance C and M recorded with the IRIS spectrometer during 2001-2002.

The time profile of the hard X-ray emission generated in the most intensive flare of importance M1.2 on April 15, 2002 (commencement at 2305 UT) was obtained with a second resolution in five energy ranges (fig.9a). On the profile, one can clearly see the emission pulses of the order of 10–20 s. The spectral analysis of this emission in the energy range of 15–24 keV corroborates the existence of a periodic component with a period of 22 s.

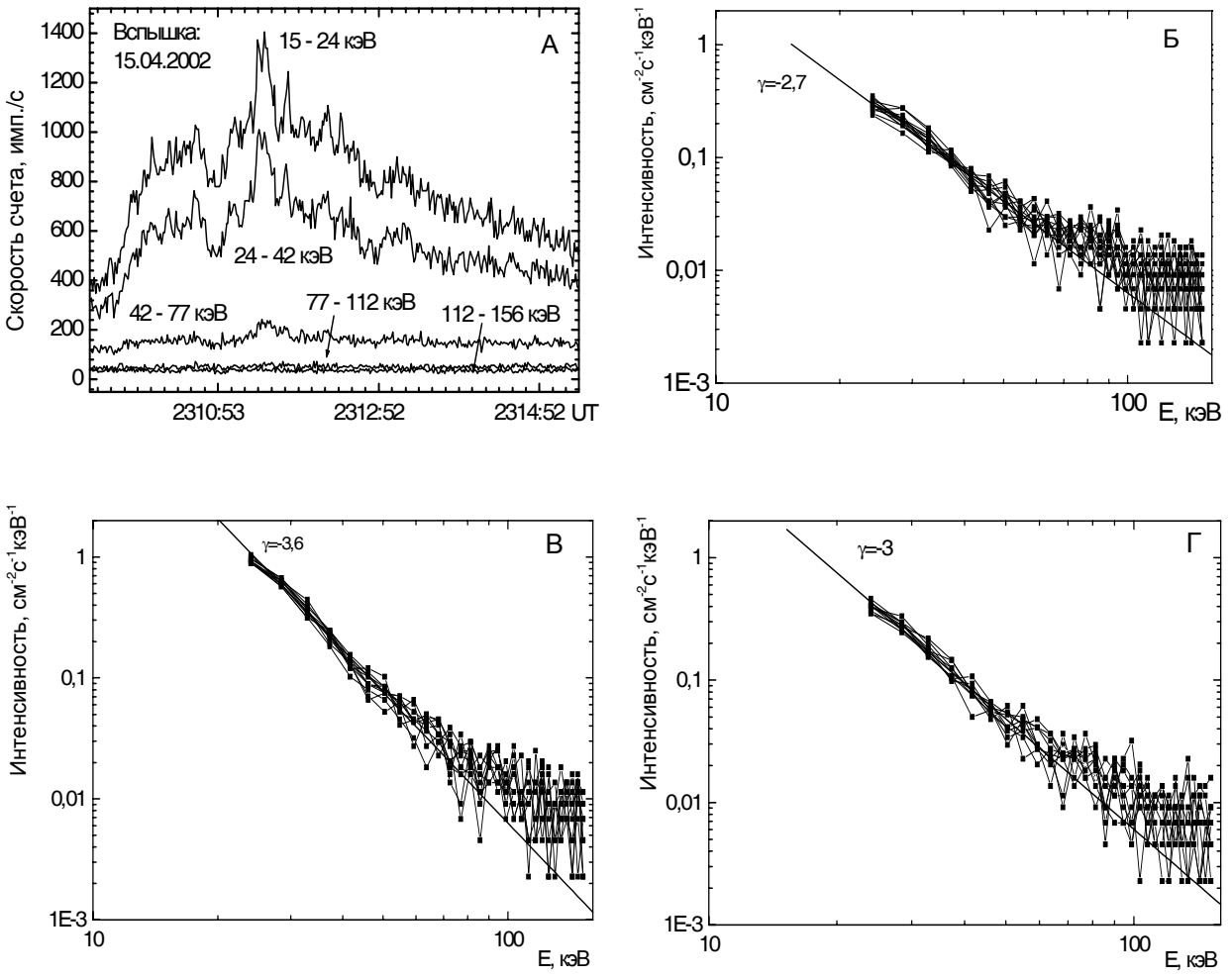

Figure 9: The emission time profile (a) and energy spectra at the maximum (c) and decline (d) of the X-ray flare on April 15, 2002, and the background spectrum before the flare (b).

Figure 9 represents the background spectrum before the flare (b) and the hard X-ray spectra measured at one-second intervals at the flare maximum (c) and decline (d). As seen from the figure, the spectrum of the flare emission at all stages of the flare evolution can be approximated with a high accuracy (except for the high-energy background) by a power-law function with the power index changing in time. Thus, the background spectrum before the flare can be described by the power-law function with index $\gamma \approx -2.7$ (Fig. 9b), which decreases in the impulsive phase reaching the value $\gamma \approx -3.6$ at the peak of the flare (Fig.9c) and, then, increases in the flare decline phase (Fig. 9d).

The hard X-ray emission spectrum from the minor flare of July 26, 2002 (commencement at 09:20:31 UT) differs from the spectrum of the previous flare by its shape changing during the flare evolution. At the flare onset (stage I in Fig.10), the shape of the spectrum is unstable, being described alternately by power-law or linear dependence. In the impulsive phase (stage II in Fig. 10), the spectrum becomes stable and is pronouncedly linear (Fig. 11a) owing to a large number of quanta with the energy less than 40 keV. The linear shape persists at the maximum and, partly, in the decline phase, after which (stage III in Fig.10) the shape of the spectrum changes and can again be described by a power-law function (Fig. 11b). Such behavior of the flare spectrum, obviously, manifests the evolution of the distribution function of the emitting electrons.

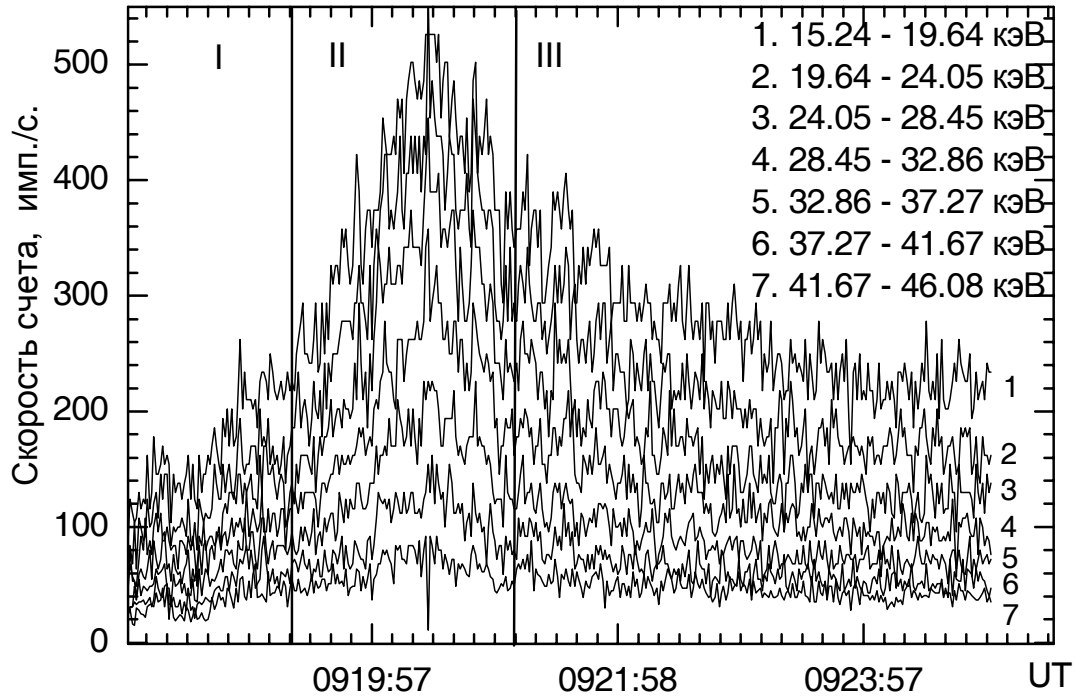

Figure 10: Time profile of the hard X-ray emission from the flare of July 26, 2002.

For the flare of December 19, 2001, which belonged to the X-ray class C4.9 (commencement at 0230:40 UT), the X-ray energy spectrum had a linear shape in

the impulsive, maximum, and decline phases (Fig. 12). The quantum counting rate at the energies above 110 keV for that flare did not exceed the background value. This spectrum can be described by both the thermal and nonthermal models, so that the choice between the models is difficult. The sole argument in favor of the nonthermal model is that the other one would require the heating of plasma to extremely high temperatures (above 10^8 K), which are hardly realistic in the events of this X-ray class.

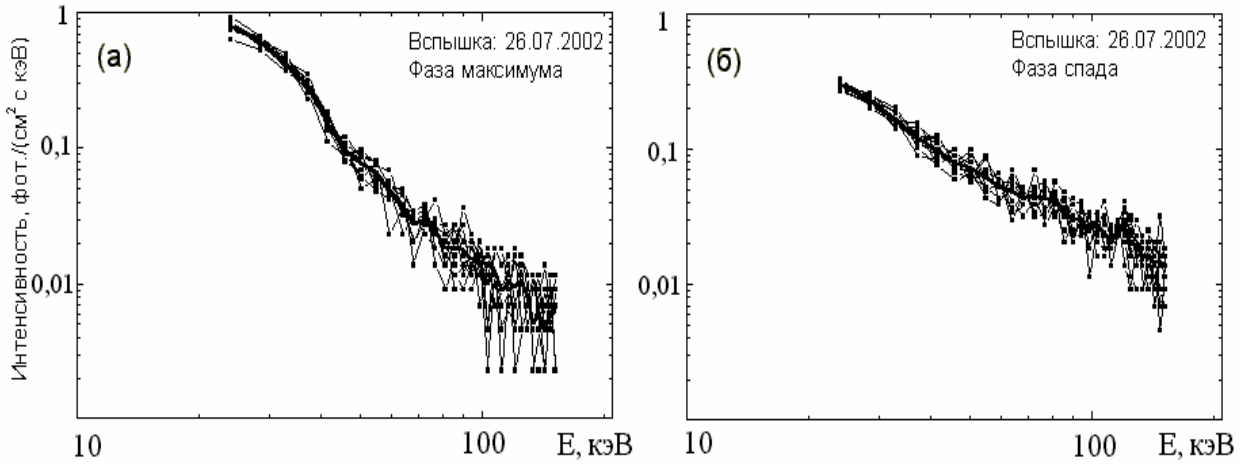

Figure 11: Energy spectra of the hard X-ray emission from the flare of July 26, 2002 at the maximum (a) and decline (b) of the event.

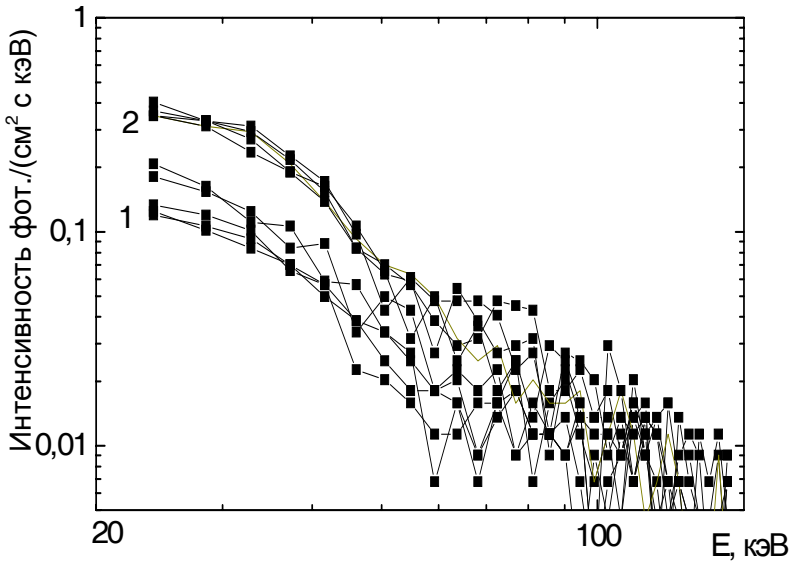

Figure 12: Hard X-ray energy spectra measured with a resolution of 1 s in the impulsive phase (1) and at the peak (2) of the flare of December 19, 2001.

The time profile for the flare of October 29, 2002 (commencement at 2147:02 UT) in the energy range of 24–160 keV summarized from four energy channels of the

instrument is represented in Fig. 13a. The total duration of the flare-generated X-ray emission was about one minute. The flare importance was C1.8. The emission time profile consists of a slowly changing component with the distinct fine structure of multiple pulses. The pulsed structure was best pronounced at the maximum and decline of the flare emission. This flare differs from those described above by a "bend" in the energy spectrum in the range of «45 keV. Fig.13b shows the spectra measured at one-second intervals in the impulsive, maximum, and decline phases, averaged over 10 s. As seen from the figure, the spectrum formed in the impulsive and maximum phases of the flare has a complex shape, which can be conventionally divided into two components with a "bend" at <<45 keV. The low-energy part of the spectrum before the bending point is, probably, due to the thermal emission of hot plasma, and the high-energy spectrum after the bend is accounted for by the bremsstrahlung emission of fast electrons. The spectrum keeps this shape in the declining phase, too. Another typical feature of the spectrum of the October 29, 2002 flare is its steepness that increases with the increase of the energy. This behavior can be explained if the distribution function of fast electrons generating the bremsstrahlung emission has a discontinuity at some maximum velocity corresponding to the energy of <<160 keV.

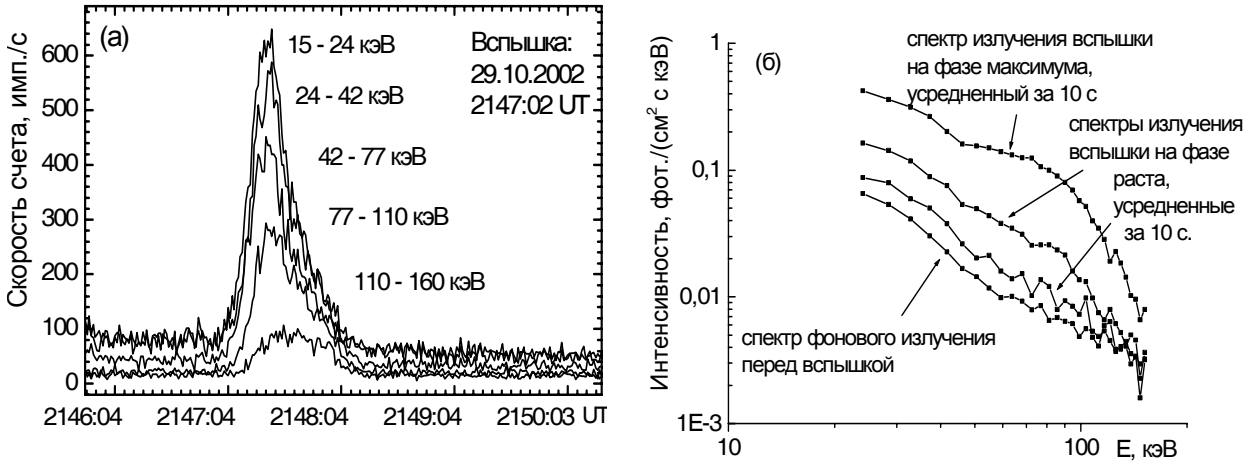

Figure 13: Time profile (a) and spectra (b) of the X-ray emission from the flare of October 29, 2002.

Thus, the analysis has shown that the energy spectrum of hard X-ray emission from the major X-ray flare of importance *M* was power law all over the flare duration. For the weaker flares of importance *C*, the spectrum was linear, possibly, with a bend in the energy range of «45 keV. Variations in the flare emission energy spectra reflect the evolution of the distribution function of the flare-accelerated electrons.

Spectrometry of the solar X-ray emission and X-ray nightglow of the Earth atmosphere according to the data of RPS-1/CORONAS-F

The data obtained with the CORONAS-F/RPS-1 device have been used to analyze the energy spectra of some minor solar flares at different stages of their evolution, as well as the spectra of the pre-flare X-ray background. The X-ray nightglow of the Earth atmosphere has been studied, and the Earth contour maps have been plotted to visualize the global pattern of the glows in the energy ranges of 3–5; 5–8; 8–16, and 16–31.5 keV averaged over the time interval selected.

Spectrometry of the solar X-ray emission

The solar X-ray flares are classified on the basis of patrol observations of the Sun in the soft X-ray emission range (1.5–24.8 keV) carried out onboard the GOES satellite (Geostationary Operational Environmental Satellite). The class of the flare is determined by the emission flux at the peak of its evolution. This classification does not provide information on the energy spectra and detailed time characteristics of the flares. The CORONAS-F/RPS spectrometer was measuring solar X-rays in the energy range of 3–31.5 keV and provided vast experimental data on the spectra of soft X-ray emission of solar flares.

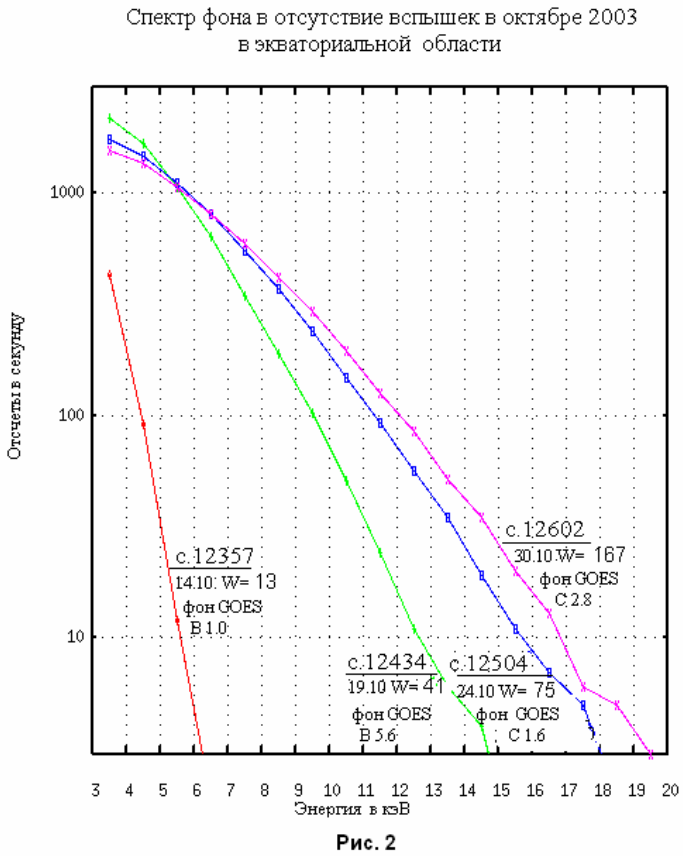

Figure 14: Background X-ray spectra in October 2003 in the absence of flare. The date of observation, Wolf number (**W**), and GOES class are shown alongside.

Figure 14 shows the spectra of the background emission of the Sun recorded in October 2003 as the satellite was passing over the Earth equator. The date of observation, Wolf number (W), and GOES background class in the same units as the flare emission are specified for each spectrum. One can see that, according both to GOES and to RPS-1 devices, the background flux and rigidity of the solar radiation grow with the increase of solar activity.

Figure 15 illustrates the time profiles of three flares and their spectra at points 1-5. The flares were recorded on October 13, 2004 against a low background level (point 1). The first increase was identified as a minor flare of class B1.0 according to the GOES classification. The following two increases were not included in the catalog. Since the signal counting rates at the maximum of the first and third flares (channels 3–5 and 5–8 keV) are virtually equal and their spectra are identical (points 2, 5), the third flare may be also classified as B1.0. The second, much weaker, flare with the maximum flux $<10^{-7}$ W/m^2 can be assigned to class A. The source temperature for all three flares was determined (Fig. 16) by comparing the measured spectra with those calculated with the CHIANTI 5.2 model. These three flares are likely to display fast and appreciable changes of temperature (from 9 to 10 MK) in one source.

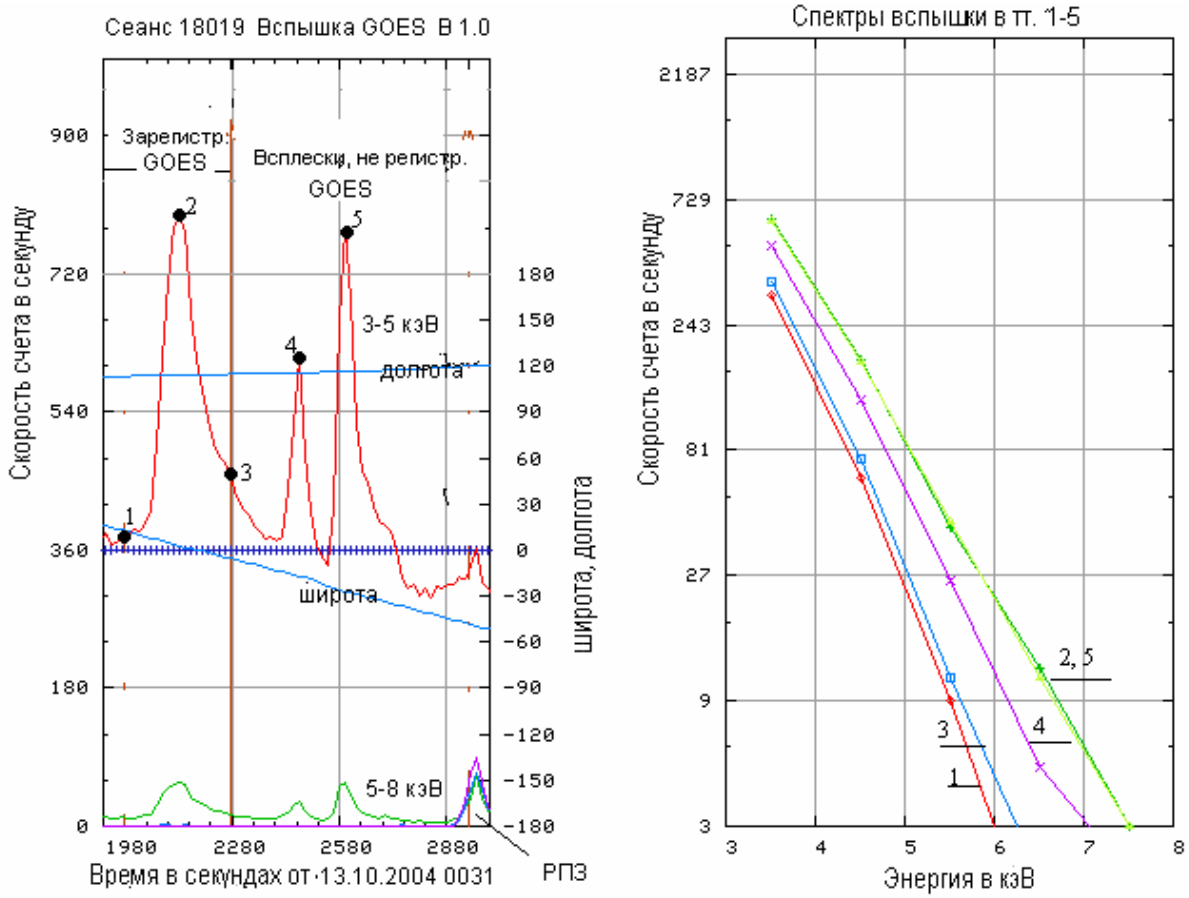

Figure 15: Time profiles in the energy ranges of 3-5 and 5-8 keV (GOES) and spectra at points 1–5 for three flares recorded on 13.10.2004 (RPS-1/CORONAS-F).

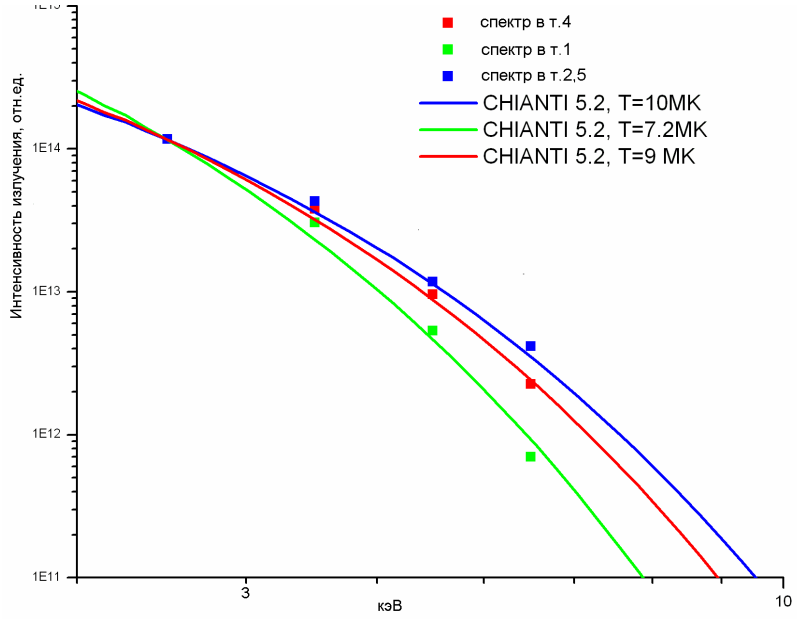

Figure 16: Comparison of the spectra in Fig. 15 with the CHIANTI 5.2 model.

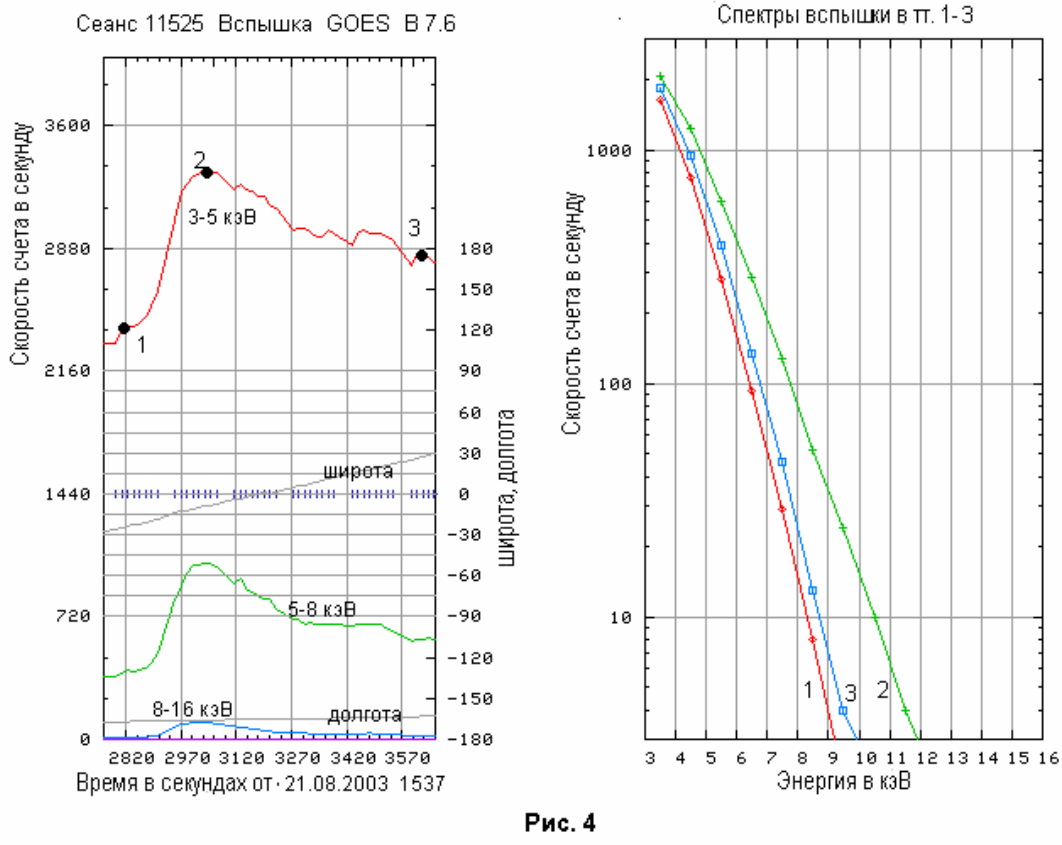

Figure 17: Time profiles in the energy ranges of 3–5, 5–8, and 8–6 keV (GOES) and spectra at points 1–3 for the flare of class B7.6 recorded on 21.08.2003 (RPS-1/COEONAS-F).

The time profiles and spectra at points 1–3 for a more intensive flare of class B7.6 recorded on 21.08.2003 are presented in Fig. 17. This event occurred against a more intensive and harder pre-flare X-ray background (point 1) than the one

illustrated in Fig. 15. The flare was characterized by a typical long ("stepwise") decay; the spectrum at the maximum (point 2) was much harder than the spectrum of the B.1.0 flare (Fig. 15, point 2).

As the activity in cycle 23 was decreasing, the flares were observed at a lower background level. Fig. 18 shows the time profiles and spectra of the class B9.5 flare recorded on 02.05.2005. The commencement, maximum, and ending of the flare (points 1, 3, 4) are marked according to GOES. RPS-1 did not register the end of the flare, because the satellite entered the Earth's shadow. The maximum quantum energy recorded in that flare (spectrum at point 3) exceeded the upper energy limit of the GOES instrument.

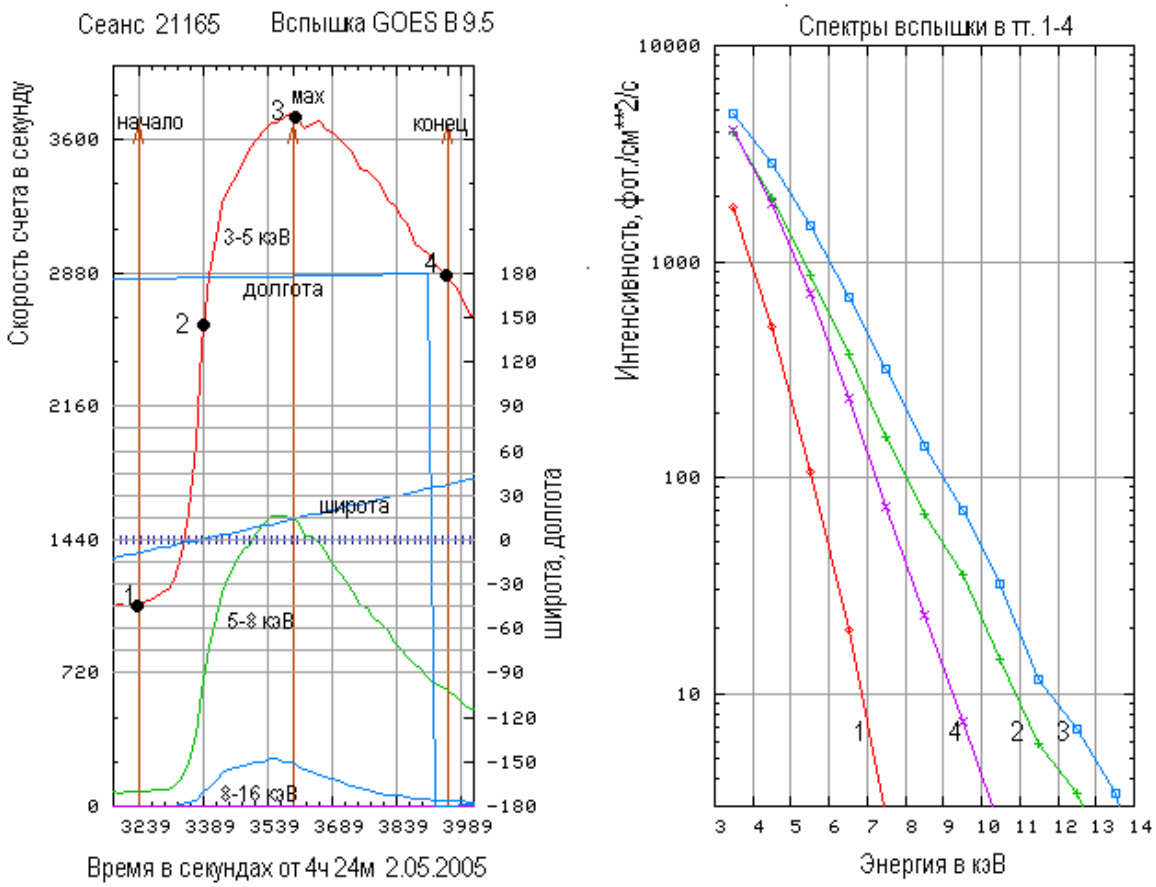

Рис. 5

Figure 18: Time profiles in the energy ranges of 3–5, 5–8, and 8–16 keV (GOES) and spectra at points 1–4 for the flare of class B9.5 recorded on 02.05.2005 (RPS-1/CORONAS-F).

Figure 19 demonstrates a still more intensive flare C1.2 ($1.2 \cdot 10^{-6} W/m^2$), which occurred on 08.11.2005 also against a relatively low background. The commencement, maximum, and ending of the flare are marked according to GOES. RPS-1 could not register the end of the flare because of entering the Earth's shadow. The flare had two maxima, the spectrum of the second maximum being

more rigid than the spectrum of the first one. The increase in the highest energy range (8-16 keV) started approximately a minute after the flare began. The second increase is characterized by simultaneous arrival of soft and hard X-rays.

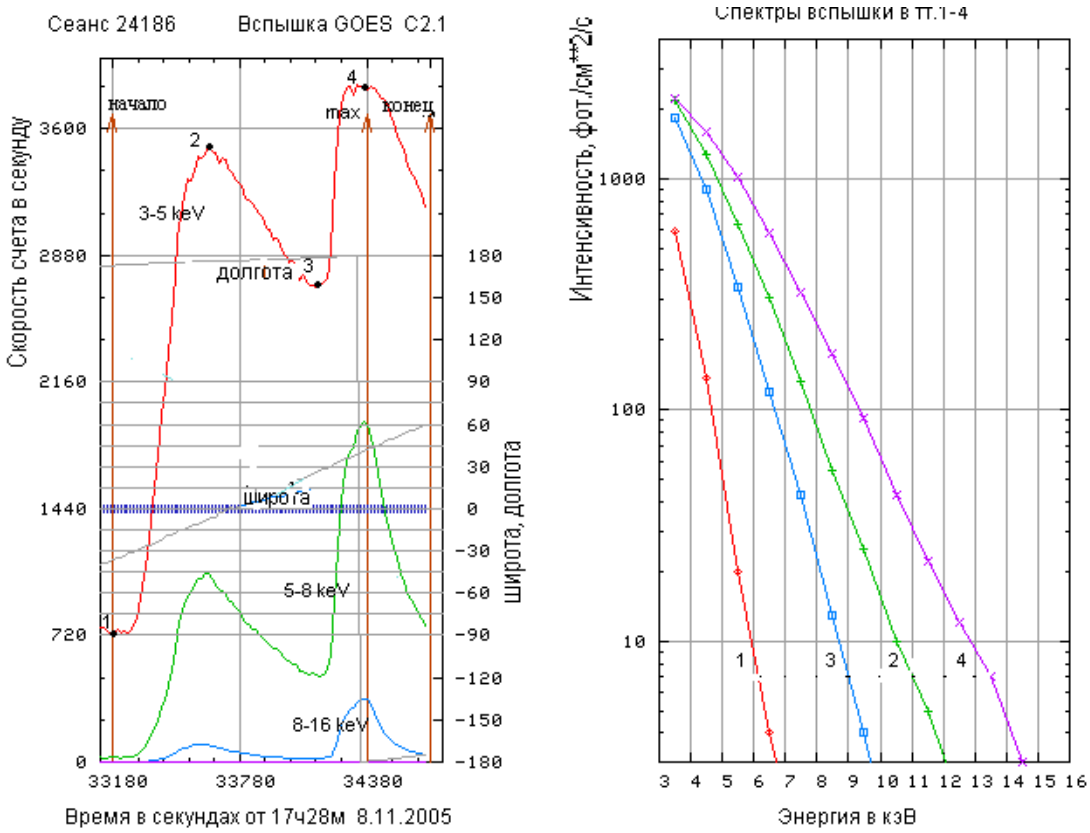

Figure 19: Time profiles in the energy ranges of 3-5, 5-8, and 8-16 KeV (GOES) and spectra at points 1–4 for the flare of class C1.2 recorded on 08.11.2005 (RPS-1/CORONAS-F).

Upper atmosphere nightglow

While the CORONAS-F mission was in the Earth's shadow, the RPS-1 instrument was recording the soft X-ray emission of the upper nighttime atmosphere, as well as the signals from charged, high-energy particles of the Earth's radiation belts that were detected when passing the high-latitude regions and the zone of the Brazilian magnetic anomaly (BMA). The X-ray emission in the Earth's upper atmosphere is secondary by its nature. In the energy range under consideration, it is mainly due to the bremsstrahlung radiation of the precipitating magnetospheric electrons. Long-term (07.2001-12.2005) high-sensitivity observations of the nighttime atmosphere with RPS-1 provided us with a global radiation pattern in the form of the X-ray maps of the Earth and revealed its seasonal dependence.

Figure 20 represents the maps of nighttime emission of the atmosphere for the period from 23.03.2002 to 23.03.2003 in the energy ranges of 3–5; 5–8; 8–16, and 16–31.5 keV and for the periods of northern summer (23.03.2002-23.09.2002, Fig. 21) and winter (23.09.2002–23.03.2003, Fig. 22).

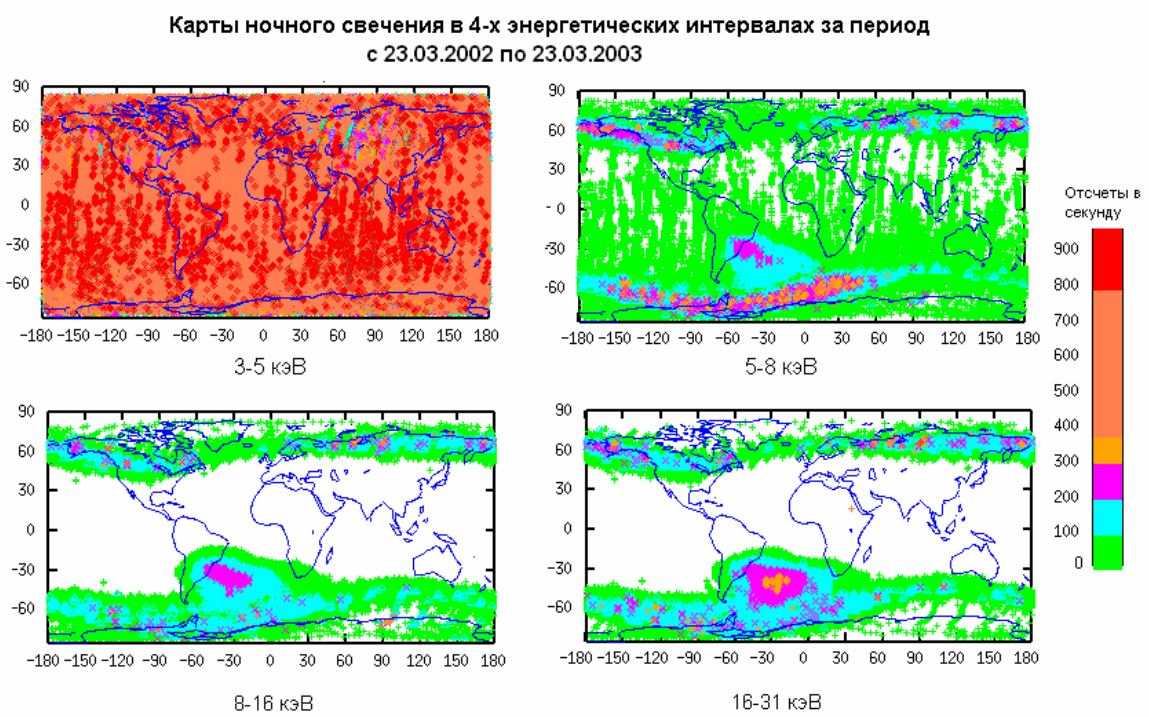

Figure 20: Maps of the nighttime atmospheric emission in the energy ranges of 3–5, 5–8, 8–16, and 16–3 keV based on the CORONAS-F/RPS-1 data for 23.03.2002-23.03.2003.

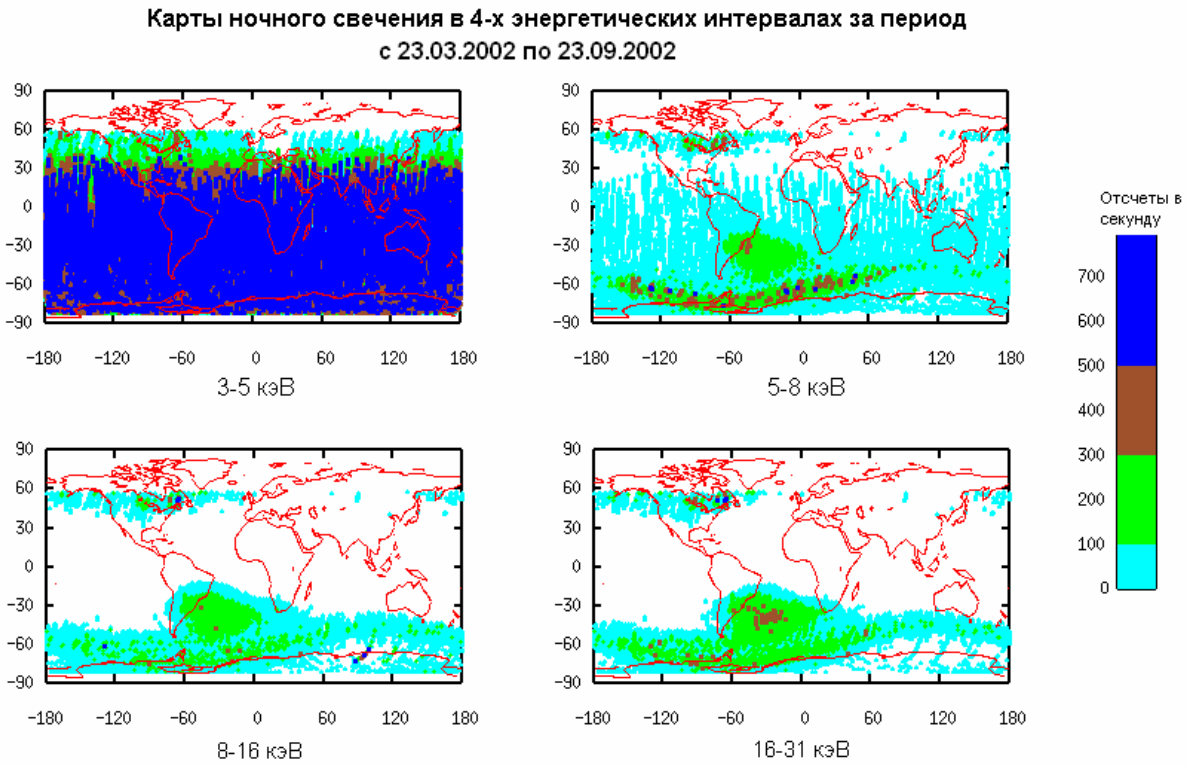

Figure 21: Maps of the Earth's atmospheric nighttime emission in the energy ranges of 3–5, 5–8, 8–16, and 16–31 keV based on the CORONAS-F/RPS-1 data for 23.03.2002-23.09.2002 (north summer).

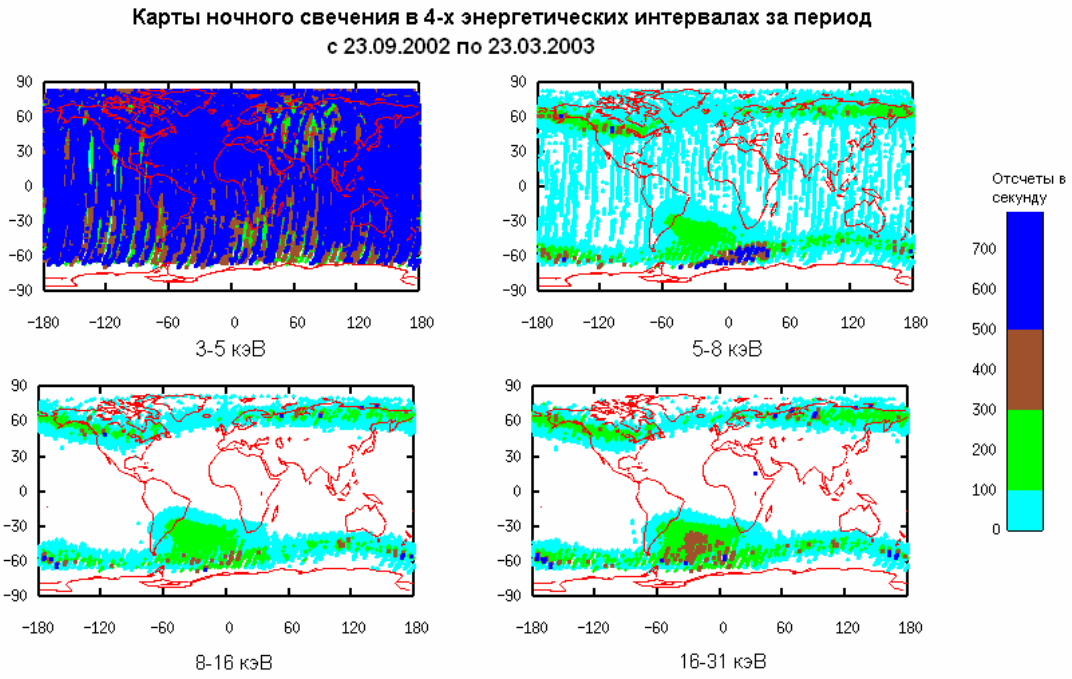

Figure 22: Maps of the Earth's atmospheric nighttime emission in the energy ranges of 3–5, 5–8, 8–16, and 16–31 keV based on the CORONAS0-F/RPS-1 data for 23.09.2002–23.03.2003 (northern hemisphere, winter).

Figure 20 shows that the intensity of the nighttime atmospheric emission decreases with the increase of the quantum energy. In the energy range of 3-5 keV, the nighttime glow is observed all over the atmosphere, being the brightest in the southern hemisphere over the Pacific and Indian Oceans. In the northern hemisphere, the brightest glow is observed at high latitudes. At lower latitudes, it fades, vanishing completely in some regions on the map in the range of 5–8 keV. At >8 keV, the instrument detects signals only in the Earth's radiation belts, whose boundaries are clearly seen on the maps for 8–16 and 16–31 keV.

The nightglow intensity changes during the year in various atmospheric regions. The maps for 3–5 keV display the limits of the polar day in summer (Fig. 21) and in winter (Fig.22). In summer, the atmospheric nighttime emission at 3–5 keV in the latitude range of 30°-60° north is much weaker than in the other regions.

On the maps for 5-8; 8-16, and 16-31 keV in Fig. 21 (northern hemisphere, summer 2002), the decrease of the emission intensity from the Earth's radiation belt in the northern hemisphere from the Atlantics to Chukotka is seen as a "break" in ERB. In summer, the ERB maximum at the height of 500 km at these latitudes is in the polar day zone and, therefore, is invisible on the map. However, areas of lower intensity might be observable. The "break" (Fig. 22) is not observed in winter, and, in the vicinity of the cycle minimum, it is absent even in summer (2004). In the southern hemisphere, no break is revealed at the change of season. The effects observed may be due to the high level of solar activity, when the

density of the upper atmosphere increases leading, together with the seasonal warming, to reduction of the ERB particle fluxes at those altitudes. A weak glow at the energy <5 keV in the "break" zone (Fig.21) is, most likely, caused by the galactic cosmic rays.

Conclusion

Thus, detailed spectral and time characteristics of minor solar X-ray flares were obtained for the first time during the CORONAS-F/RPS-1 experiment. This allowed the precise source temperature to be determined by comparing the measured spectra with those calculated by up-to-date models, such as CHIANTI 5.2. Quantitative estimates were obtained to characterize the increase of the X-ray background spectrum rigidity with the increase of solar activity.

It is shown by observations that, in the energy range of 3-5 keV, the nightglow is observed all over the atmosphere; in the range of 5-8 keV, there are regions where the nightglow is absent; and at >8 keV, it is only present in the zones of the Earth's radiation belts. In summer 2002, in the northern hemisphere (from the Atlantics to Chukotka), the glow in the ERB zone was observed to decrease.

2.1.2.2. COMPASS-2: Ionosphere and Natural Hazards

Experimental small satellite «Compass-2» — results of flight tests

The experimental small satellite «Compass-2» was created within the framework of the Federal Space Program of Russia. It was the pilot project in a series of satellites intended for space experiments on detection of the precursors of strong earthquakes with the aim of creating a space system for monitoring natural and man-caused catastrophes. The primary goal of launching the microsatellite was the test and adjustment of all basic elements of the space system.

Figure 1: Small satellite «Compass-2» in flight.

The newly developed special-purpose scientific equipment, its operating modes and characteristics, the facilities for real-time gathering, processing, and analysis of information, as well as the new service systems of the microsatellite, such as the central onboard processor, equipment of the telemetry radio channels and radio-control, systems of orientation and maintenance of the thermal mode, and power supply system were tested during the realization of the pilot project.

The Makeev Design Bureau of the State Rocket Center was in charge of the space rocket complex comprising the «Compass-2» satellite platform and the conversion rocket RSM-54 («Shtil») launched from a submarine in the Barents Sea.

The Pushkov Institute of Terrestrial Magnetism, Ionosphere and Radio wave Propagation (IZMIRAN) of the Russian Academy of Sciences was in charge of the scientific and methodical development of the project and delivery of the onboard scientific equipment in cooperation with Ukraine, Hungary, Poland, and Sweden.

The control of the "Compass-2" satellite was carried out by the Space Mission Control Center TSNIIMASH (Korolev), State Rocket Center (Miass), and IZMIRAN (Troitsk).

On 26 May 2006, the experimental small satellite «Compass-2» was launched into near-Earth orbit with the inclination of 78.90º, apogee of 519.0 km, perigee of 412.3 km, and cycle time of 93.59 min. The total weight of the satellite was 80 kg (including the weight of the scientific payload equal to 20 kg). The dimensions of the satellite in the closed status were 1694×766×500 mm. The launch was carried out by a conversion rocket-carrier «Shtil» – a converted submarine rocket RSM-54 (underwater start).

The flight tests of "Compass-2" were completed in July 2007.

The scientific payload comprised five devices intended for monitoring the near-Earth space with the purpose of detecting and recording abnormal physical phenomena in the Earth atmosphere, ionosphere, and magnetosphere caused by the seismic and human activity.

The set of the scientific equipment of "Compass-2":

- two-frequency (1.2 and 1.5 GHz) GPS receiver of the satellite navigation system (ASN) intended for global monitoring of the ionosphere and atmosphere by the method of trans-ionospheric sounding;
- two-frequency transmitter RBE 150/400 "Mayak" intended for radiothomographic reconstruction of the ionosphere and local ionospheric anomalies;
- radio-frequency analyzer RFA in the frequency range from 100 kHz to 15 MHz intended for registration of plasma frequencies in the ionosphere used to determine the key local parameters of the ambient plasma;
- low-frequency wave analyzer VLF/ULF in the frequency range of 0.1–20 кHz intended for registration and analysis of abnormal low-frequency noises in the near-Earth space caused by the seismic activity;

• radiation and ultraviolet sensor DRF intended for measuring electrons and protons of the Earth radiation belts and cosmic rays, as well as the ultra-violet radiation of the Earth's top atmosphere.

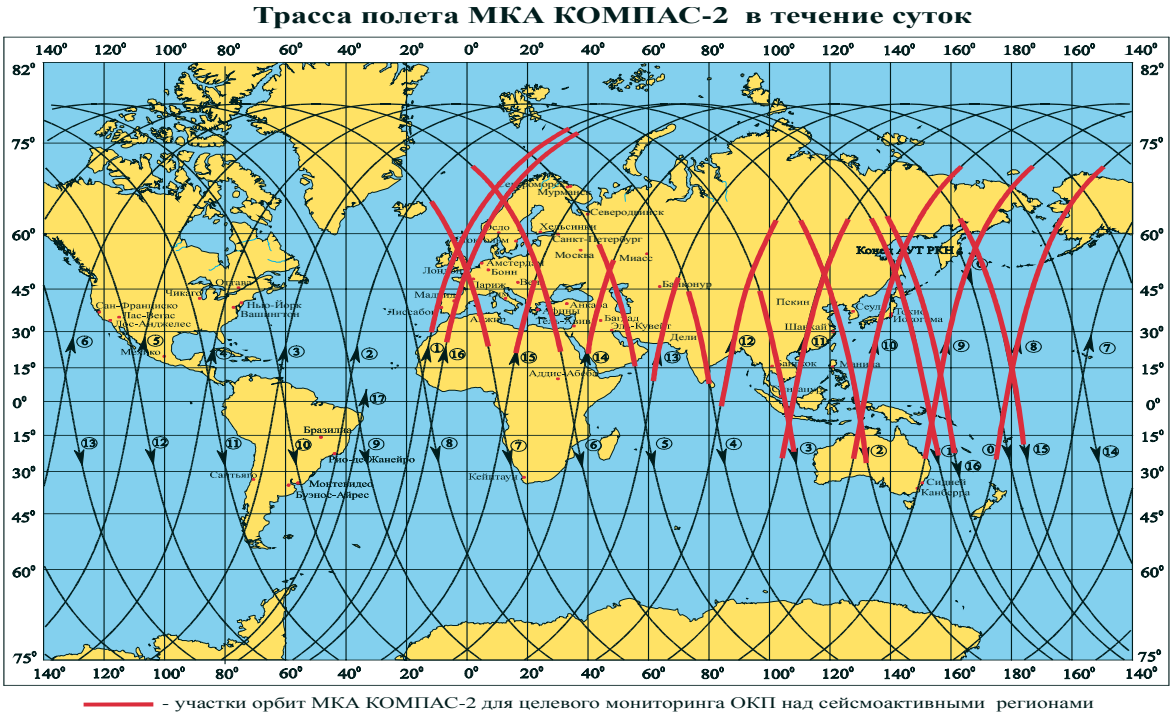

Figure 2: Trajectory of the "Compass-2" orbits over the world seismic zones.

During a day, the "Compass-2" orbiter repeatedly passed over the zones of enhanced seismic activity (Fig. 2). That was where all scientific devices were switched on for measuring and recording the abnormal phenomena. One can see that virtually all seismic regions on the Earth could be covered by measurements.

Results of the flight tests of the "Compass-2" payload

The flight tests of the "Compass-2" platform revealed some problems and significant restrictions in its operation associated with malfunctioning of the service systems (the channel of radio-control and power supply system). Because of these restrictions, the necessary performance conditions could not be provided, and the devices did not fulfill their target tasks completely. However, the primary goal of the flight tests – the trial operation and adjustment of the scientific equipment – was achieved. The basic characteristics of the scientific devices were checked up and confirmed. A few cycles of measurements and monitoring of the near-Earth space parameters over the seismic zones were performed.

In the process of the flight tests and trial operation of the scientific equipment, the background conditions in the ionosphere were measured, a powerful storm activity was observed in the top atmosphere, streams of accelerated protons and electrons

were recorded in the near-Earth space (due to the solar activity during a large geomagnetic storm on December 15, 2006), positioning of the satellite by GPS signals was performed with the ASN device. The whistler registration was carried out. The passage of strong whistlers from the Earth surface to the satellite by a short way (partially-dispersed whistlers) and the spectrum spreading of the signals from ground-based ULF radio stations were recorded. The whistler signals accompanying the seismic processes were detected.

Some results of the tests and measurements for each device of the complex are given below.

The positioning of the satellite was fulfilled with the ASN device. It was shown that the onboard two-frequency GPS receiver could be used for determining the spacecraft orbital characteristics and timing the measurements with a high accuracy. This is important when unique synchronous experiments with ground-based and orbital facilities are carried out in a uniform system of time.

The two-frequency transmitter RBE 150/400 “Mayak” was checked under the conditions of wrong-oriented satellite. This allowed a qualitative estimate of the regular functioning of the device, but did not allow radiotomographic measurements of the ionospheric structure.

Figures 3–7 illustrate radio-frequency analyzer RFA measurements taken in different time intervals.

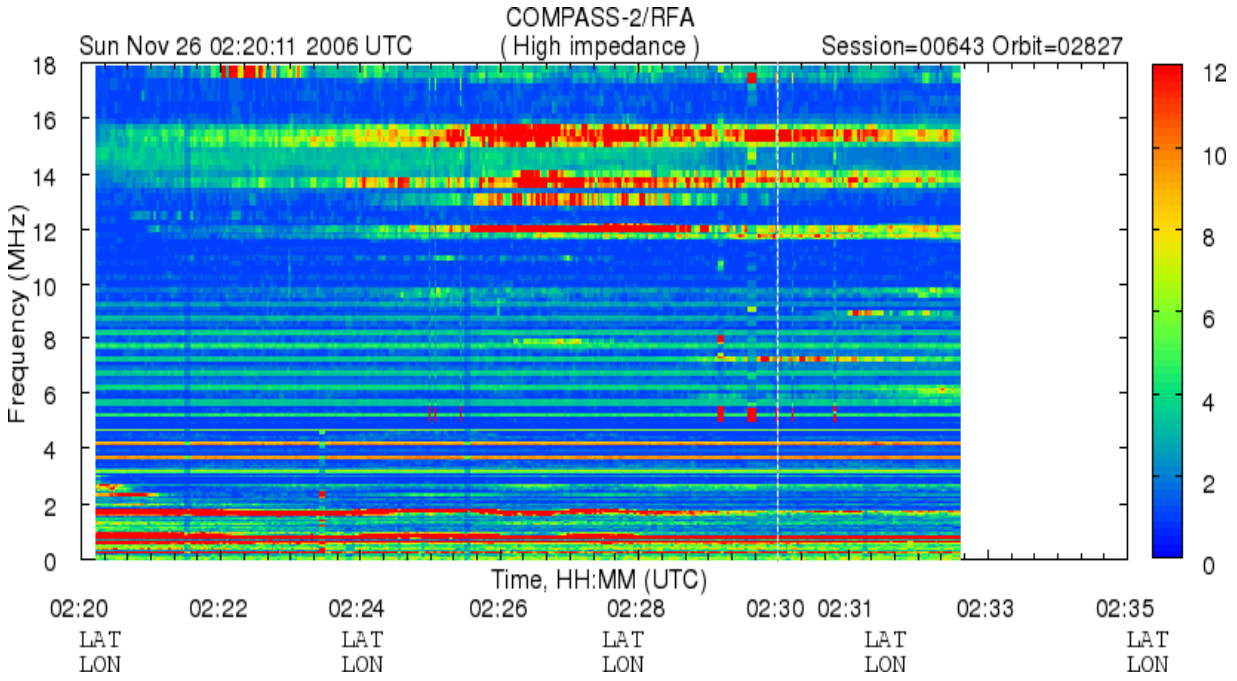

Figure 3: A radio-frequency dynamic spectrum of plasma radiations in the ionosphere measured with the RFA device. The **x** axis shows the time, and the **y** axis shows the radiation frequency. The color denotes the radiation intensity. The spectrum provides information on the parameters of the ionosphere and phenomena therein.

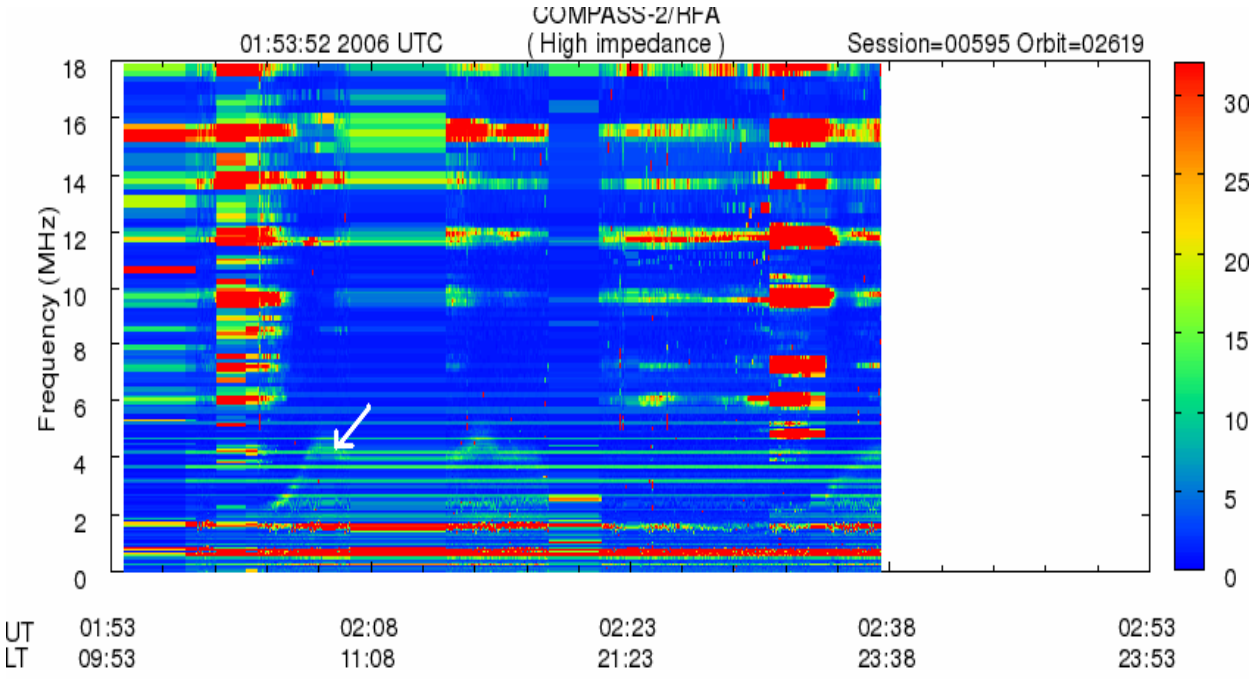

Figure 4: A dynamic spectrum obtained with the RFA device during the flight over the equatorial anomaly. One can clearly see a resonance at the local plasma frequency in the frequency range of 2–4 MHz (green color and arrow).

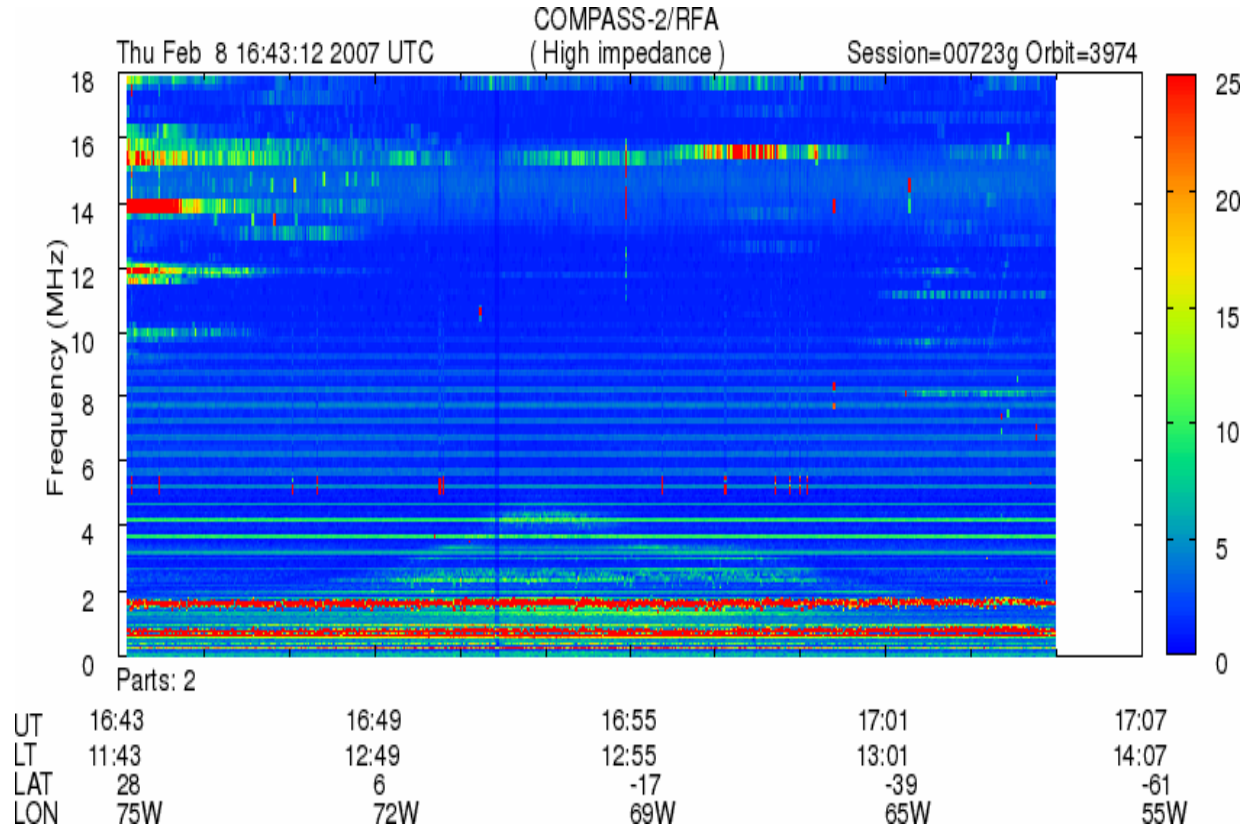

Figure 5: Stretched representation of the dynamic spectrum of plasma radiations recorded during the flight over the western coast of the South America on February 8, 2007.

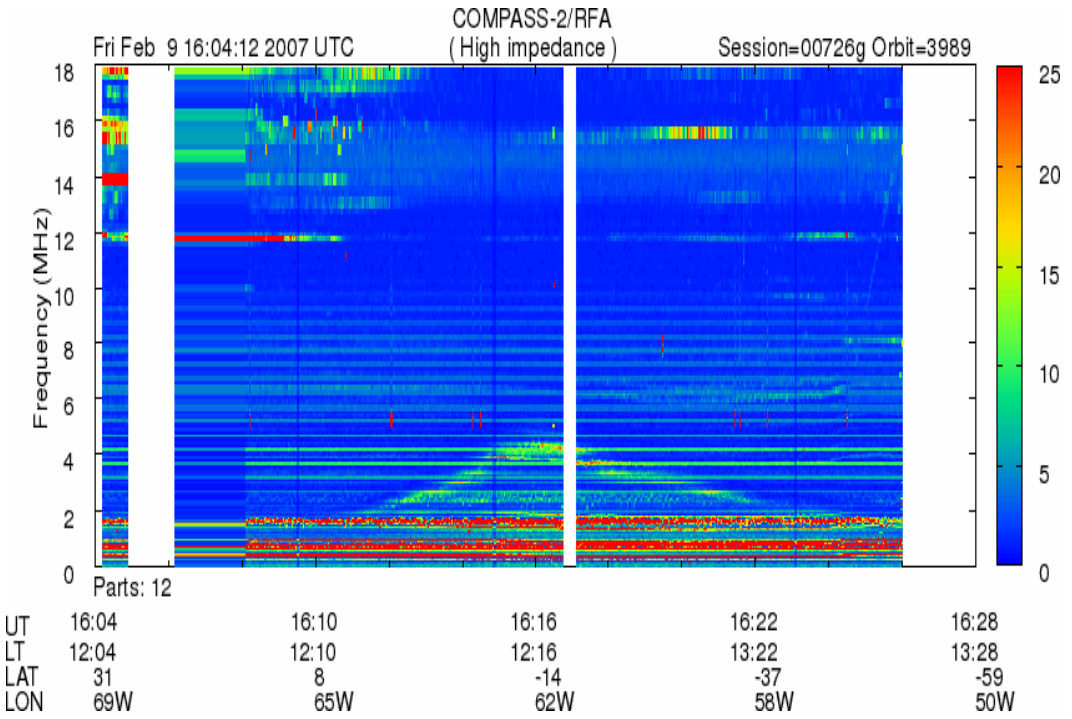

Figure 6: Plasma resonances at the frequencies of 2–4 MHz recorded with the RFA device over the equatorial anomaly on February 9, 2007.

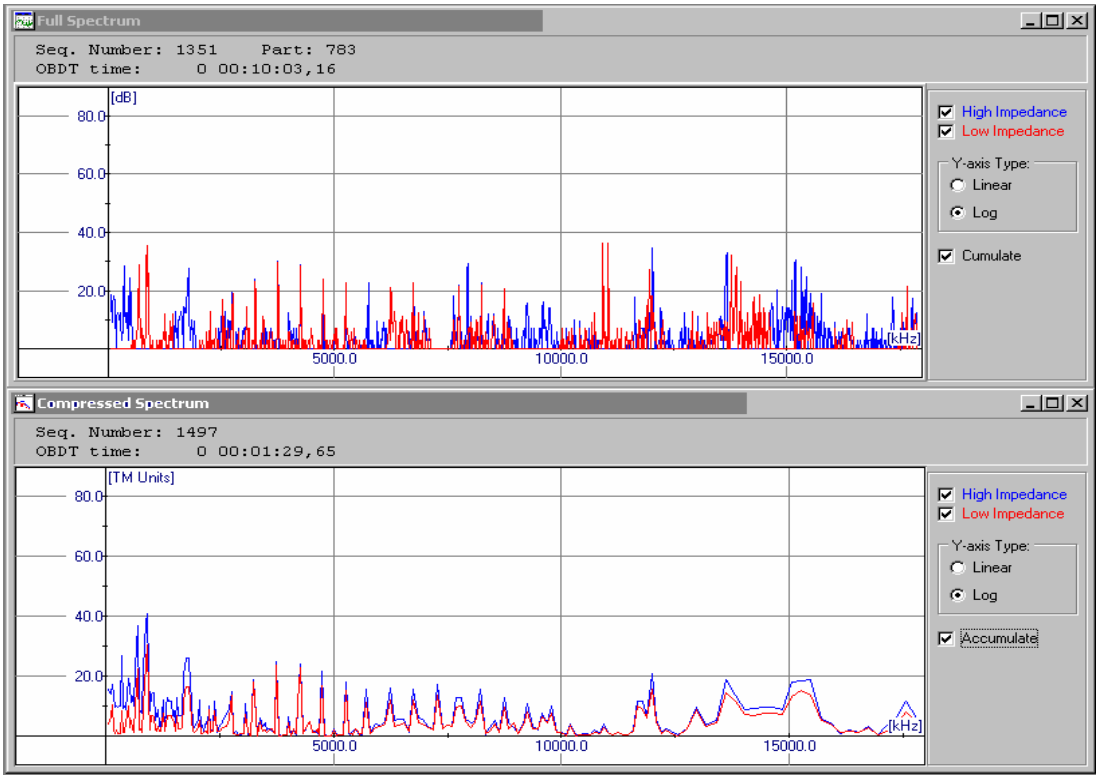

Figure 7: The peak radio emission spectrum obtained with the RFA device. One can see the peaks of radiation at the fixed frequencies corresponding to the characteristic plasma frequencies of the ionosphere.

The radiation and ultraviolet sensor DRF was measuring high-energy particles and various kinds of luminescence. These measurements ensured the monitoring of geophysical conditions along the spacecraft orbit, which is highly important to the interpretation of data and separation of the background and abnormal events. Fig. 8 illustrates the measurements of energetic particles. Besides the measurements of the radiation background along the orbit, one can see the moments, when the satellite entered the polar caps, as well as the associated increases of the radiation level (Figs. 8–10).

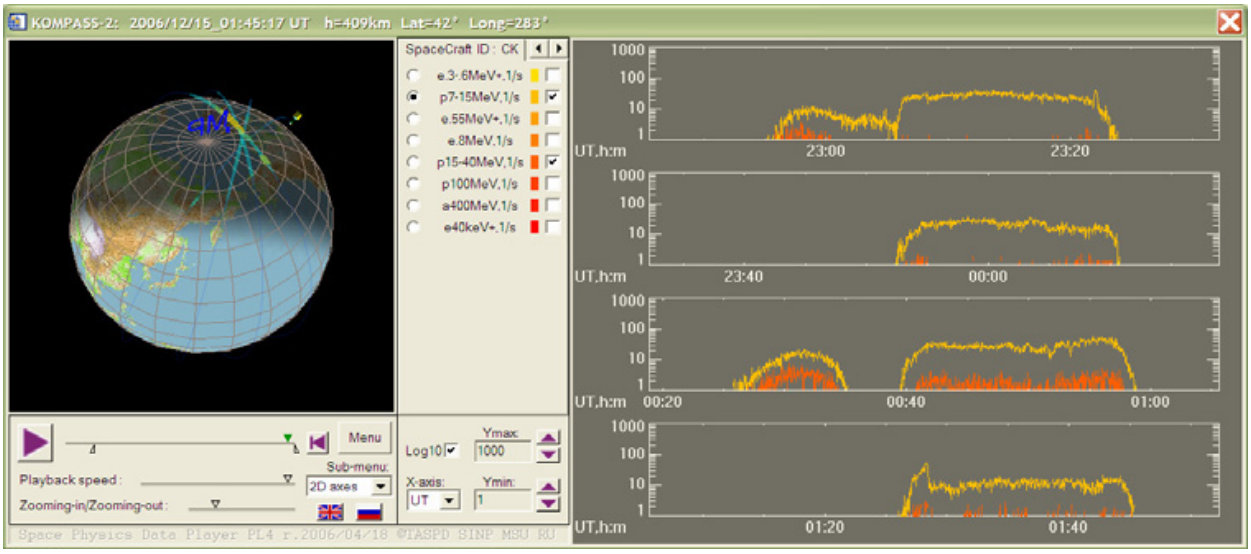

Figure 8: Charged particle streams recorded with the DRF device during the geomagnetic storm of December 15, 2006. The view of the Earth from the North Pole is shown on the left panel.

The yellow and orange curves in the right-hand part of Fig. 8 show the results of measuring proton streams with the energies of 7–15 MeV and 15–40 MeV in four consecutive flights through the southern and northern polar caps of the Earth. The X axis shows the world time UT; the Y axis is the logarithm of the detector counting rate. The plateau curves indicate that particles in the energy ranges under discussion penetrate the magnetosphere down to the heights of 400–450 km along the quasi-open magnetic field lines in the polar areas. The recorded protons had been accelerated and appeared in the vicinity of the Earth as a result of the solar flares of December 13 and 14, 2006. The increases to the left of the polar plateau (on the first and third graphs) correspond to the passage of the satellite over the South-Atlantic magnetic anomaly.

Figure 9 is similar to the previous one except for an additional red curve showing the records obtained in the channel of the discharge counter. The last but one plot in Fig. 9 displays an increased level of the 15–40 MeV protons, probably, associated with the arrival of particles from the flare of December 14, 2006. The left panel represents the view of the Earth from the South Pole with significant radiation streams indicated over the Atlantic coast of Brazil.

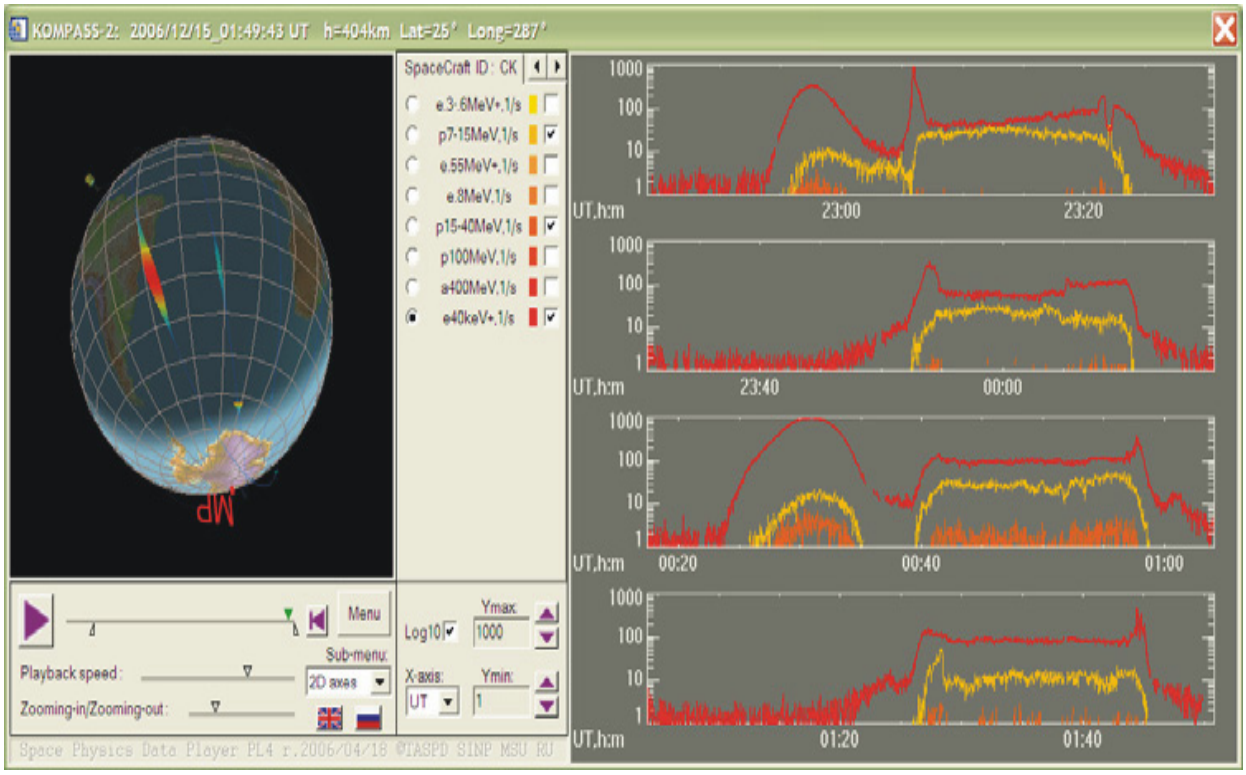

Figure 9: The view of the Earth from the South Pole (left panel). The charged particle streams (protons, 7–15 MeV) recorded with the DRF device and the records obtained in the channel of the discharge counter (red) during the geomagnetic storm of December 15, 2006 (right panel).

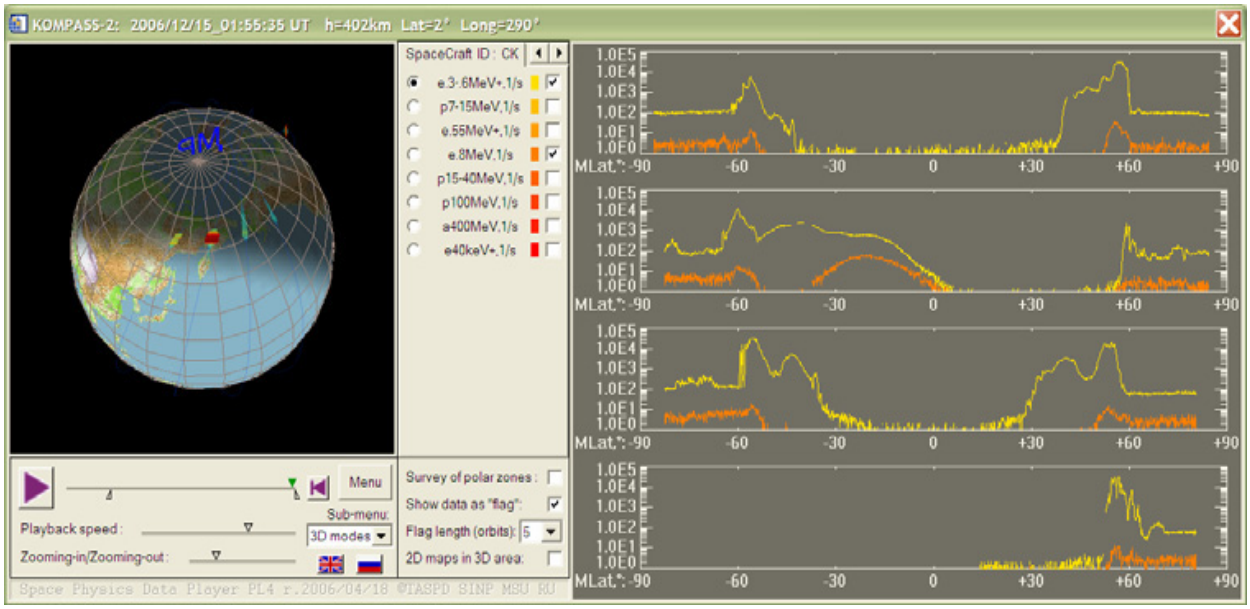

Figure 10: Charged particle streams recorded with the DRF device during a geomagnetic substorm of December 15 2006. The left panel shows the view of the Earth from the North Pole.

Figures 11 and 12 represent the oscillograms obtained with the ultraviolet detector DRF on the night side of the Earth.

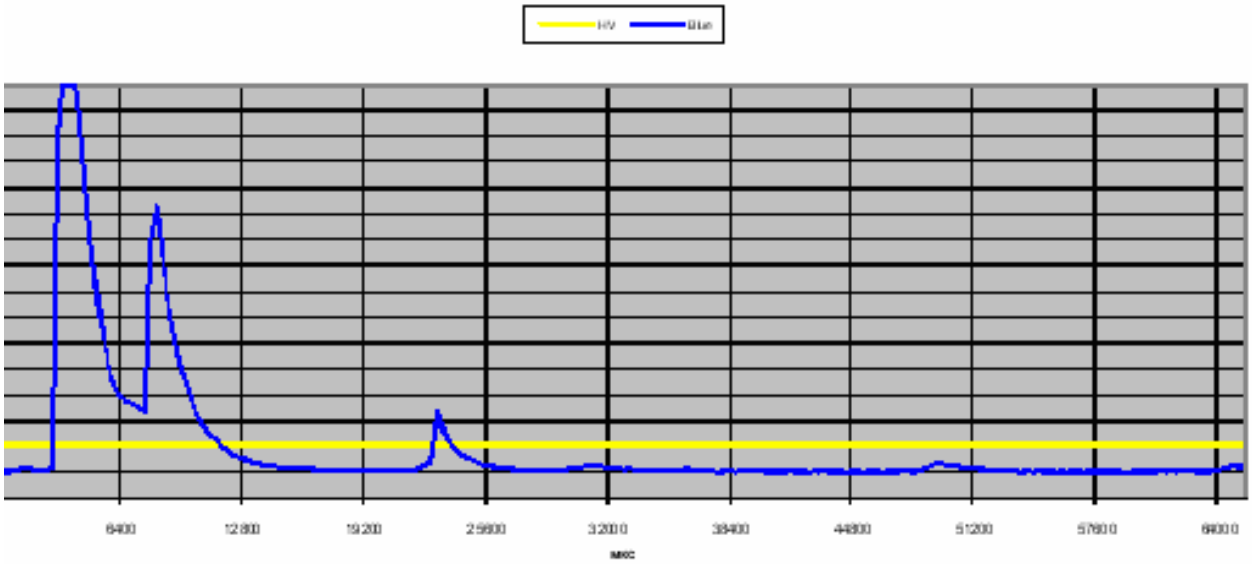

Figure 11: The oscillogram displays a powerful storm phenomenon recorded with the ultraviolet detector DRF over Kenya on the night side of the Earth at 21:04:41 UT on 02.12.2006. One can see a double initial pulse, which, apparently, is the result of two nearly simultaneous discharges.

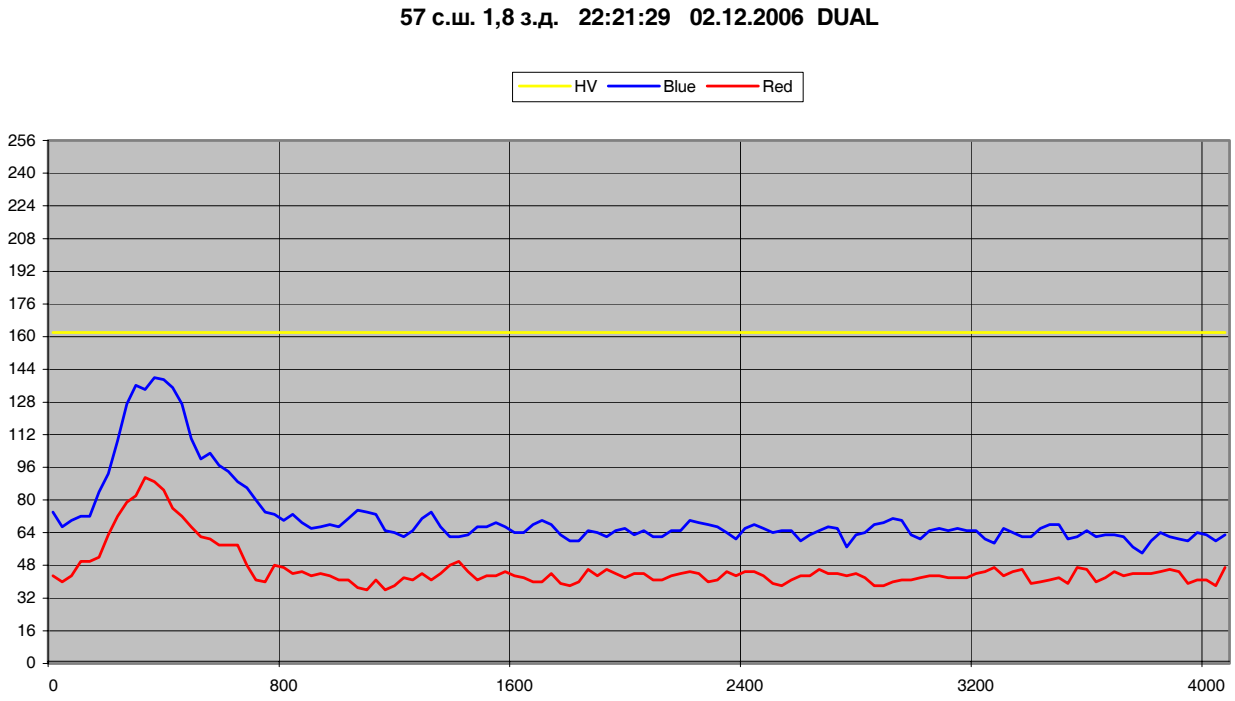

Figure 12: Oscillograms of radiations recorded with the ultraviolet DRF detector on the night side of the Earth at 22:21:29 UT on 02.12.2006. The oscillograms represent measurements in the UV (dark blue curve) and red (red curve) wavelength channels — a fast optical phenomenon recorded over Scotland at 22:21:29 UT on 02.12.2006.

Figures 13–22 illustrate the results of measurements with the low-frequency wave complex (NVK).

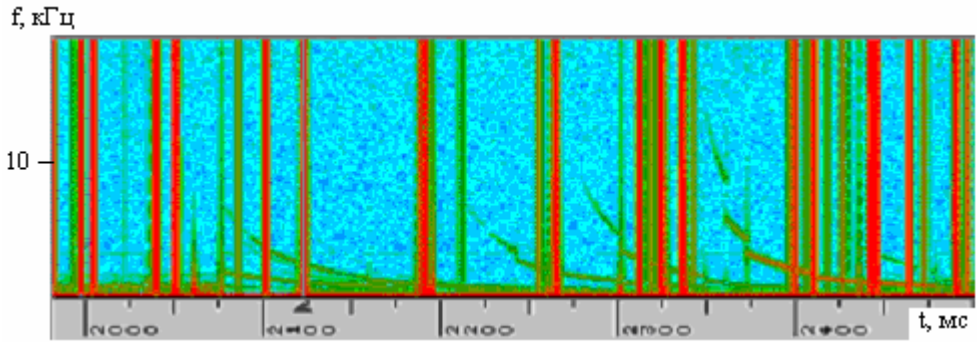

Figure 13: An example of the measurements taken with the low-frequency wave complex in the VLF frequency range (about 10 kHz). This is a so-called sonogram, i.e., the same dynamic radiation spectrum as that yielded by the RFA device, but in the range of low frequencies. The X axis is the time, and the Y axis is the radiation frequency. The color represents the radiation intensity. One can see the tracks due to the propagation of whistlers in the ionosphere.

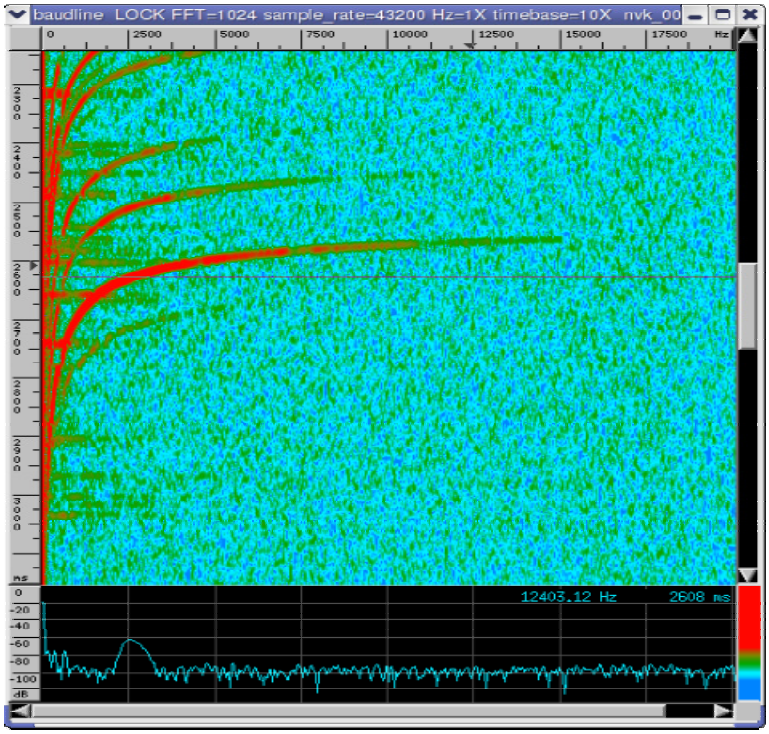

Figure 14: A record obtained onboard the satellite with the NVK device. The top fragment represents a dynamic spectrum, i.e., a sequence of the Fourier spectra of the ~20 ms time realizations shifted by ~0.2 ms. The time scale is in ms and the frequency scale, in Hz. On the spectrogram, one can see traces of discrete signals with the frequency decreasing in time. The intensity scale of the traces is given on the right of the bottom fragment. The signals have a duration of ~200–400 ms. They are the so-called partially-dispersed whistlers generated by lightning discharges in the "Earth-bottom ionosphere" waveguide tube and propagating by a short way up to the height of the satellite. The vertical green lines on the spectrogram are traces of the service information of the satellite. The bottom fragment represents the full spectrum of the time realization of duration of 2608 ms where the vertical bars on the abscissa axis coincide with the frequencies on the ordinate axis on the top fragment. The spectral maximum falls on the frequency of ~2500 Hz characteristic of the whistler spectra in the vicinity of lightning discharges.

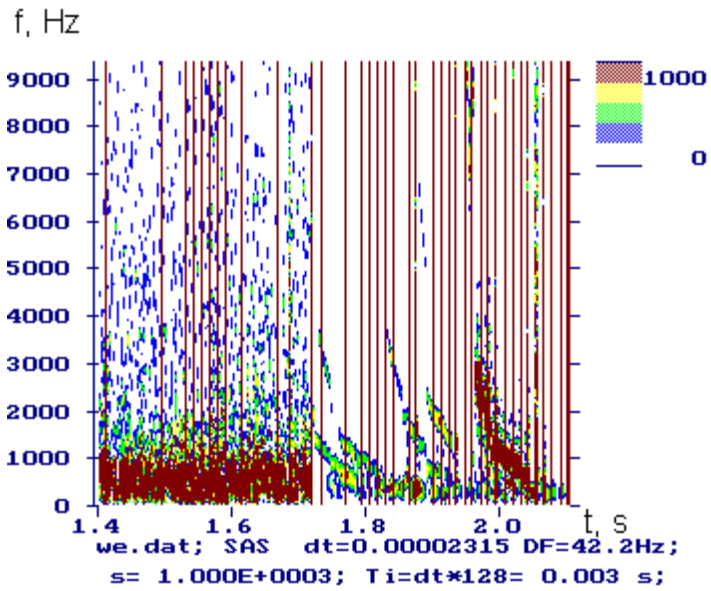

Figure 15: An example of the electric component of radiation measured with the NVK device in the range of very low (VLF) and ultra-low frequencies (ELF), orbit 00655, 29.11.06, t = 09:55:36 UT.

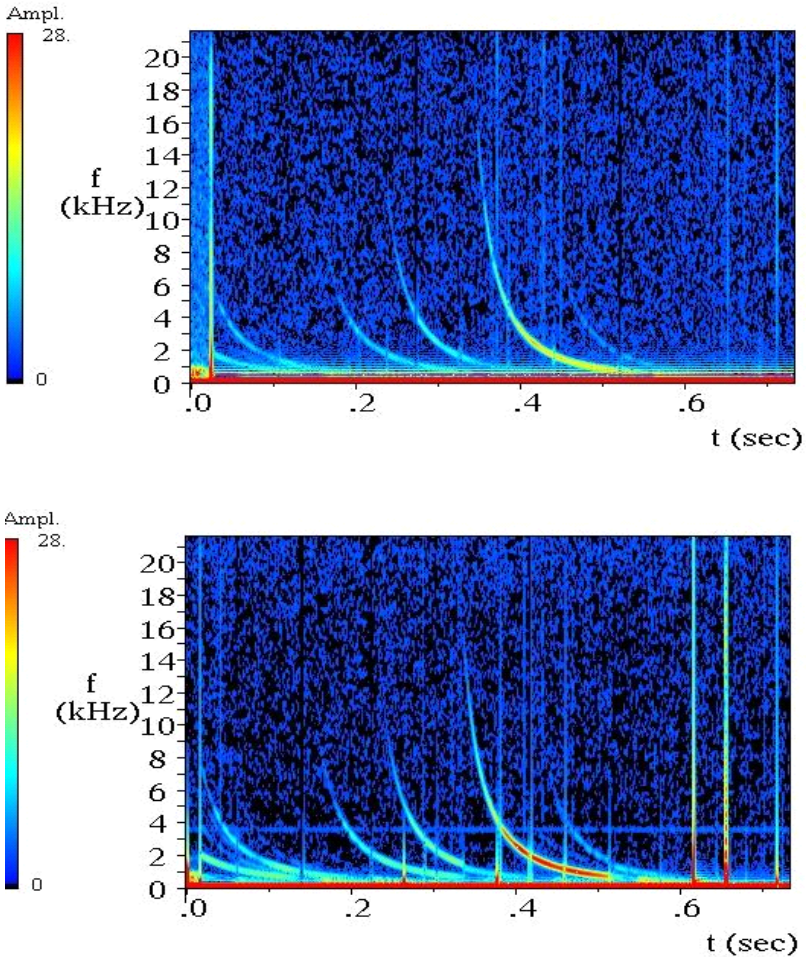

Figure 16: Whistlers in the ionosphere recorded with the VLF/ELF device on 29.11.2006, at 05:00:00 UT.

The spectrogram in Fig.16 displays the traces of discrete signals with the frequency decreasing in time. The intensity scale of the traces is shown on the left. The electric components are shown at the top of the spectrogram and the magnetic ones, at the bottom. The signal duration is ~200–400 ms. These signals are the so-called partially-dispersed whistlers. The maximum in the spectrum falls on the frequency of ~2500 Hz characteristic of the whistler spectra in the vicinity of lightning discharges. The dispersion of signals D~5 was evaluated. Ground-based observations with the TOGA system revealed a great number of strong lightning discharges in the areas over which the satellite was passing and NVK registrations were conducted. A detailed analysis of the observed VLF phenomena is carried out on the basis of exact models of distribution of whistler waves.

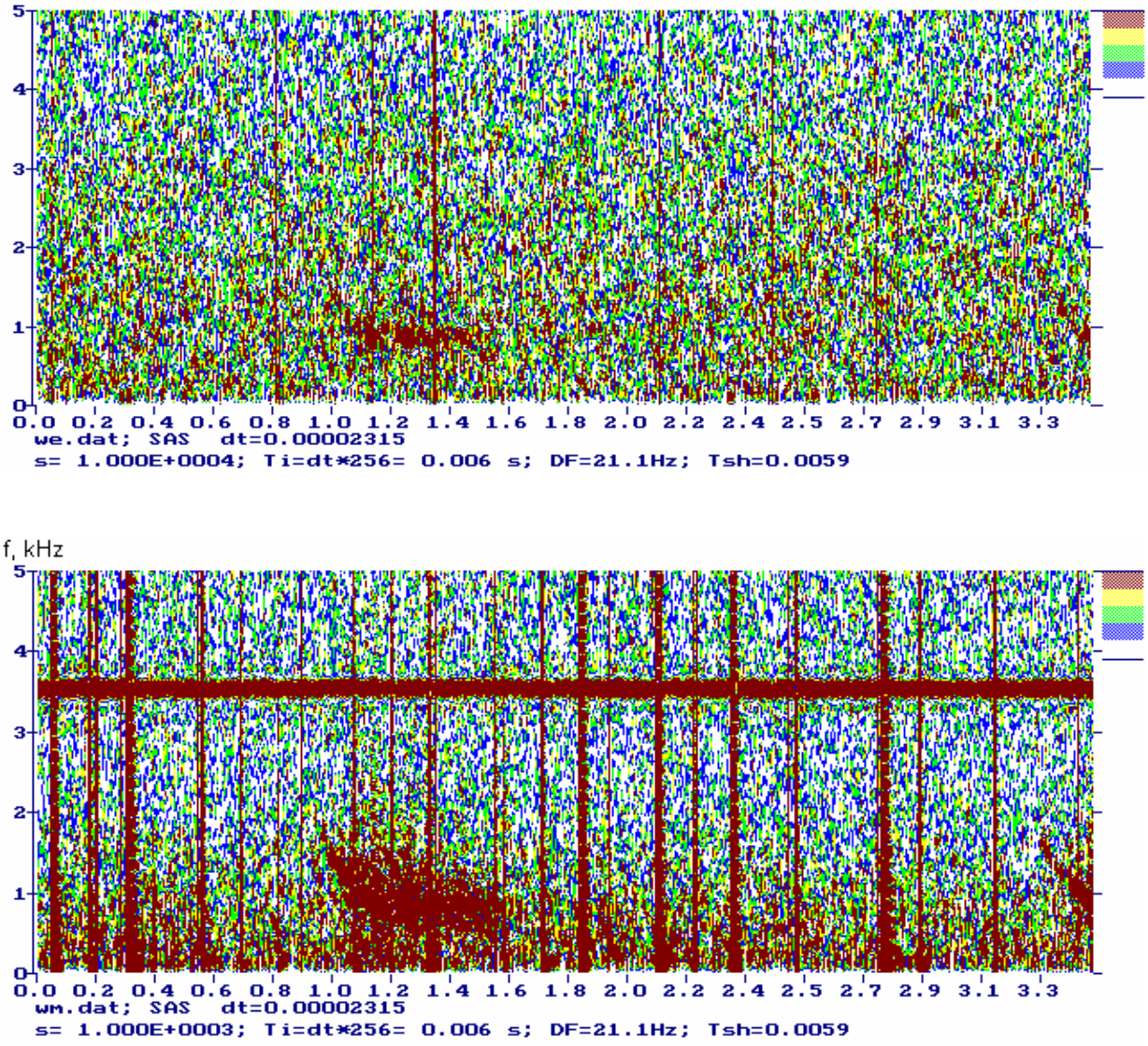

Figure 17: Low-frequency noise associated, probably, with particle precipitations recorded with the NVK device over the Central Europe on 11.02.2007 at ~10:02 UT.

As the satellite was passing over the Central Europe, an unusual high-level signal was recorded in a narrow frequency range of 500–2000 Hz. This signal is seen on the sonogram. It resembles a low-frequency partially-dispersed whistler with a subsequent noise radiation at the frequency of maximum in the spectrum of partially-dispersed whistlers. Otherwise, this might be a series of nearly undivided partially-dispersed whistlers. At the same time, the TOGA localized a few whistlers in the Mediterranean.

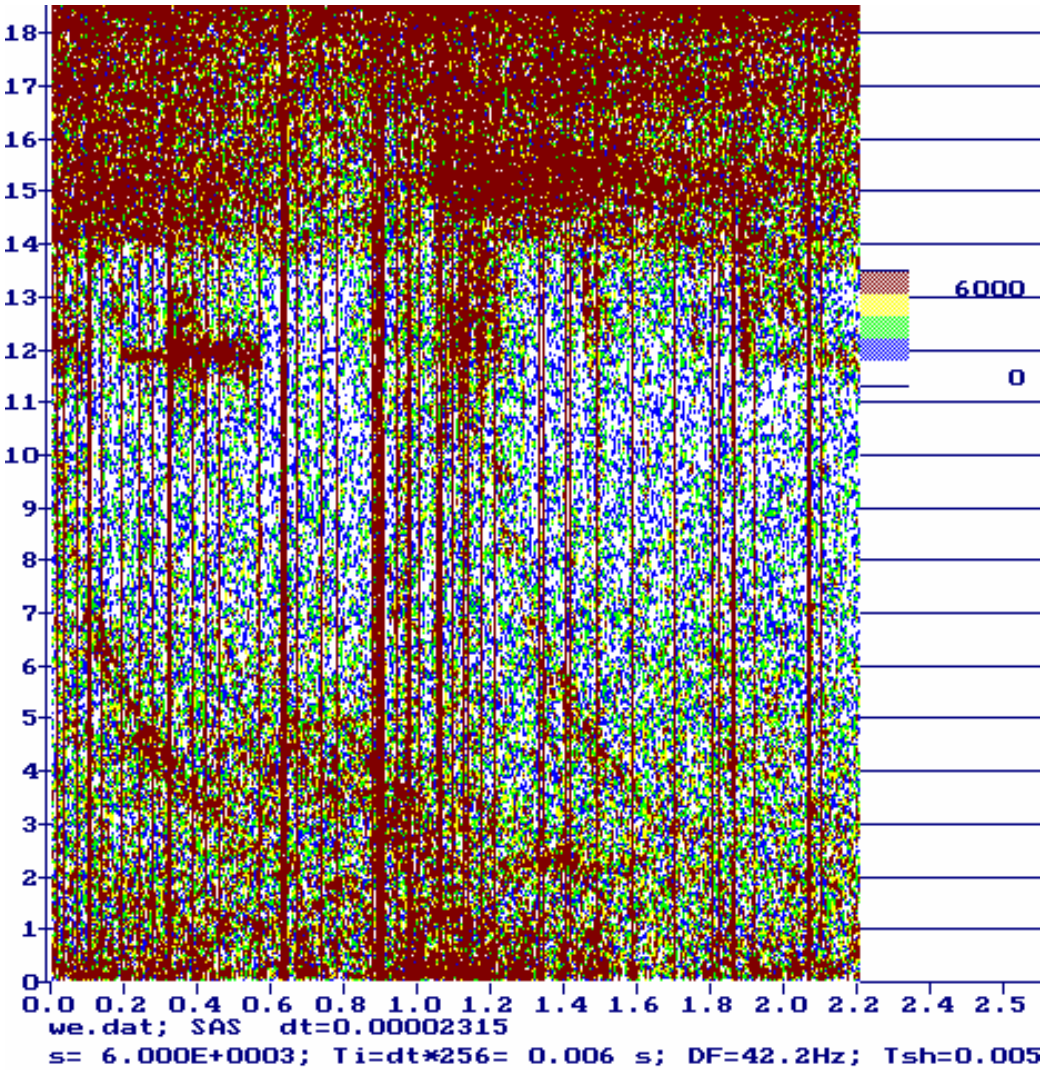

Figure 18: Supervision of the spreading frequency range of a signal of ground VLF transmitters (record of electric a component on 18.03.2007 at 17:09:17 UT).

At interaction of monochromatic waves with magnetospheric plasma there are trigger radiations or spreading frequency spectrum of these signals (fig.18). Trigger radiations, apparently, are connected to resonant interaction of VLF waves with electrons of radiating belts in a non-uniform magnetic field. Effects of spreading frequency spectrum can be caused by magnetospheric interaction of whistler waves.

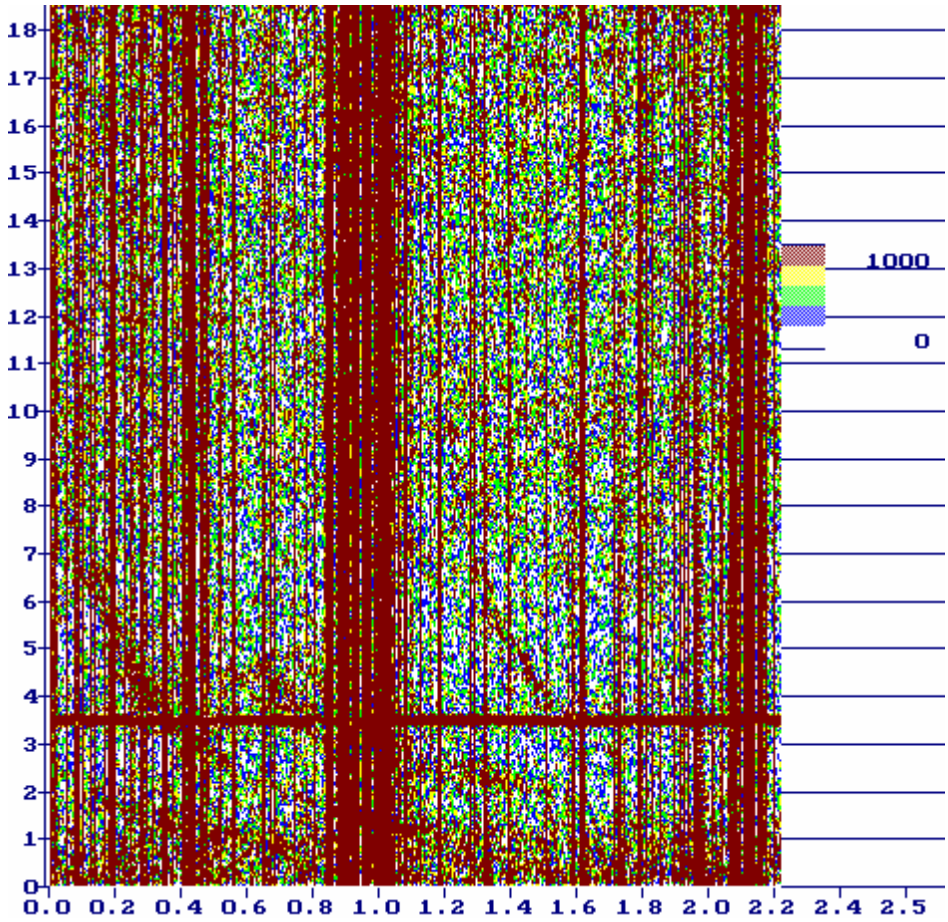

Figure 19: Whistlers registration by onboard satellite device NVK on March, 18 2007 at 17:09:17 UT, above Kamchatka (magnetic component, session 859).

Registration ordinary whistlers on satellite “Compass-2” has allowed to approve system of registration and processing of the VLF data.

Characteristics of the whistler, registered on 18.03.07 at 17:09:17 UT, are resulted in the table below: (including parameters — nouse frequency *fn*, *L*-shell on which whistler and a *D*-dispersion of whistler were propagated). Calculation of these parameters was carried out by a standard technique of processing whistlers. Characteristics of whistler correspond to the data for area of supervision (Kamchatka).

1 s — 6,57 cm

f_1 = 6 kHz; Δt_1 = 0,7 sec м = 0,1065449 sec

f_2 = 4,5 kHz; Δt_2 = 2 sec м = 0,304414 sec

f_3 = 3 kHz; F(x) =$\Delta t_1/\Delta t_2$ = 0,35; x = 0,163

$x = f_1/f_{H1}$; f_{H1} = 6/0,163 = 36,8098 kHz

f_n = 0,387·36,8098 = 14,245398 kHz

$$L = (880/36{,}8098)^{1/3}=(23{,}906677)^{1/3} =2{,}88$$

$$D_1 = \Delta t_1 f_1^{1/2}/\Phi(\beta x);\ D_2 = \Delta t_2 f_1^{1/2}/\Phi(\alpha^x)$$

$$D_1 =0{,}1065449\cdot 77{,}459666/0{,}116 = 71{,}146$$

$$D_2 = 0{,}304414\cdot 77{,}459666/0{,}33 = 71{,}454$$

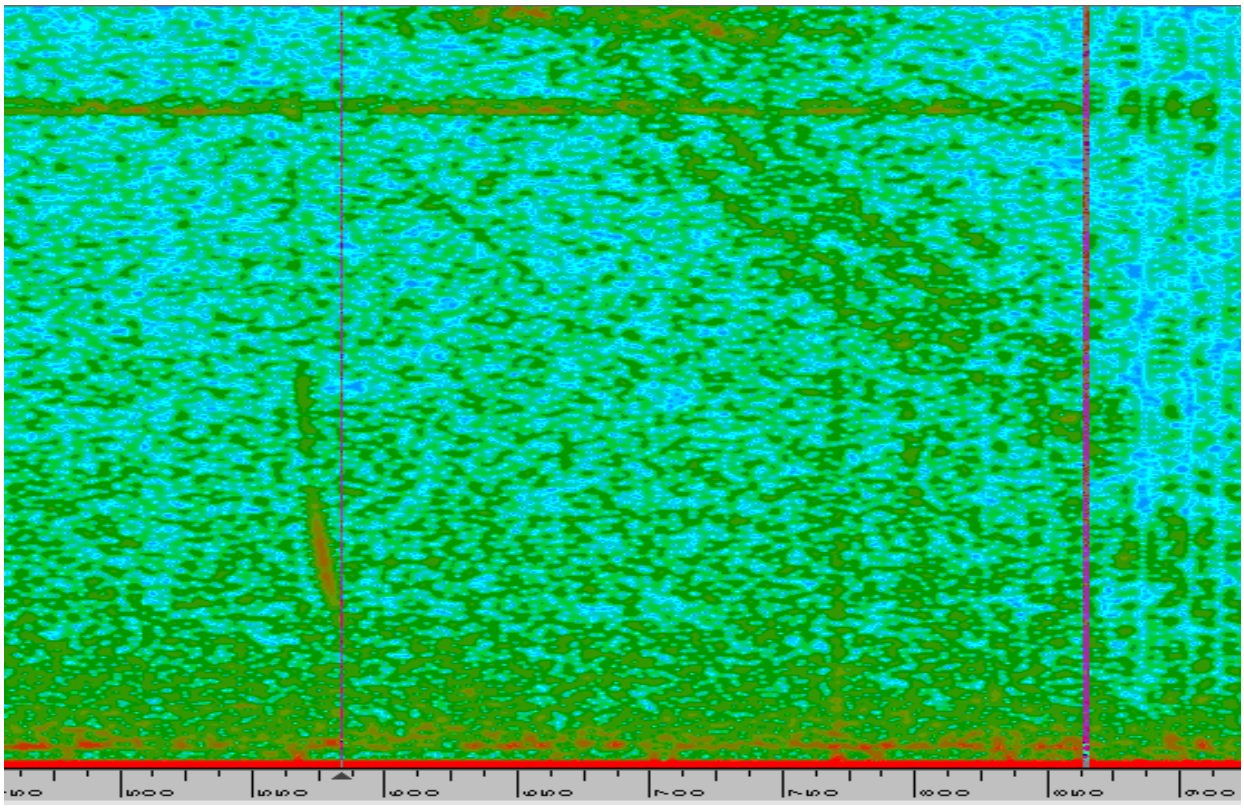

Figure 20: Whistlers registered above Kamchatka on 27.02.2007 at 21:35:49 one day prior to the earthquake.

The dynamic spectrum of low-frequency wave VLF/ULF radiations, received at flight above Kamchatka on 27.02.2007 at 21:35:49 is resulted on Fig. 20. Found out abnormal signals, are probably connected with preparation of earthquake which has taken place in area of Kamchatka on 28.02.2007 and had magnitude 4.2 (Fig. 21). At first half of plot it is well seen partly dispersed whistler with a maximum in a spectrum ~5 kHz. That specifies that it can be result of passage to the satellite whistler, which have come from distance ~1000–1500 km. On Fig. 20 a series of traces whistlers, which parameters did not manage to be estimated by standard method because of complexity of structure of a signal, also is observed. However, it is possible to estimate area in the opposite hemisphere, whence could pass signals to the satellite along force lines of the geomagnetic field. System TOGA has located group of signals in a southeast of the Australian continent at the same time.

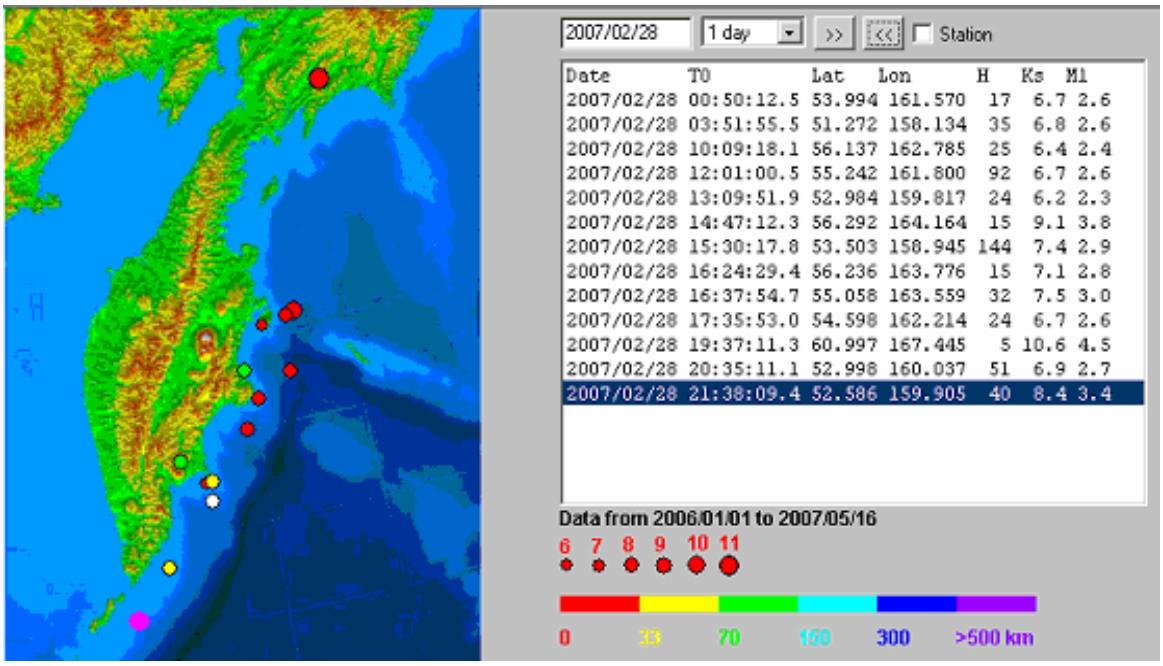

Figure 21: Distribution of earthquakes to Kamchatka 28.02.2007.

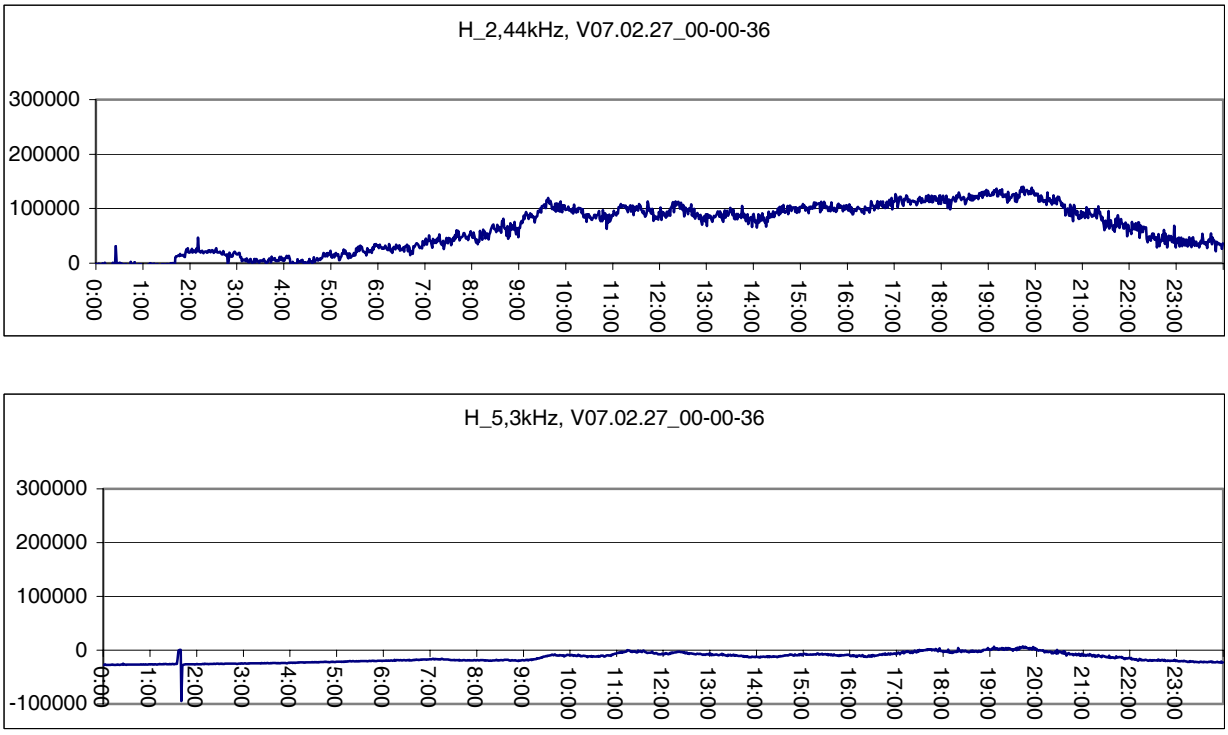

Figure 22: The ground data of reception VLF radiations on 27.02.2007 at Paratunka on Kamchatka. Above — a daily distribution of angles of arrival VLF signals (whistlers) is shown. Below — a daily course of output signals amplitude is shown. The UT time is specified.

The red circle in the top right corner of the map Fig. 21 corresponds to earthquake of class $K = 11$, and a pink circle below — position of the satellite during registration of VLF signals on 27.02.2007 at 21:35:49 (session 790).

The ground data at Paratunka on Kamchatka have shown, that during flight of the satellite above Kamchatka on 27.02.07 at 21:35:49 powerful enough radiation was observed from a southwest direction and small quantity of whistlers come from other directions. On analog record, during flight of the satellite above Kamchatka at 21:35:49 on 27.02.07 was downturn of a level of a signal on all registered frequencies, the maximal value of radiation was observed at 19-20 h. The plane of the frame aerial settled down in a direction the East – West.

The conclusion

The flight tests and operation of the scientific equipment of “Compass-2” have shown that it can be used as a basis for creating a complex of scientific devices for the future space missions intended for monitoring the near-Earth space with the aim of detecting, recording, and studying the abnormal phenomena in the ionosphere associated with earthquakes and other natural and man-caused catastrophes.

2.1.3. V.A. KOTELNIKOV INSTITUTE OF RADIO ENGINEERING AND ELECTRONICS OF THE RAS

2.1.3.1. Investigation of the coronal mass ejections by radio sounding method

1. At the basis of the experimental data of the German and American research centers the method of the multi-probe radio sounding was elaborated for an investigation of the properties, dynamics and evolution of the coronal mass ejections (CME) at the different distances from the Sun.

Both remote sensing and *in situ* observations are presently used for determination of the characteristics of a CME. Measurements available at small heliocentric distances (less than 25 solar radii — R_S) include X-ray flux (e.g. GOES-10), white-light images of the corona (e.g. SOHO/LASCO coronagraphs), and coronal radio sounding (spacecraft near solar conjunction). Only the radio-sounding method can also provide information on the solar wind plasma at intermediate heliocentric distances (30–180R_S). Beyond these distances, solar wind monitors may be located in interplanetary space, usually near the Earth or other planets. We report here the first instance of multi-probe radio sounding of a CME using the spacecraft GALILEO and CASSINI in the period from 12 to 24 May 2000. The CME was first detected on 13 May 2000 at 22:22 UT and moved into interplanetary space with very high velocity (>1080 km/s at distances of 2.3–16.6R_S). This is supported by the high velocity derived from the transit time between the maximum of the X-ray flux (at ~1R_S) and the maximum of the spectral bandwidth of the Cassini signals (at r ~2.3R_S). The lower bound on the velocity between 1R_S and 2.3R_S is determined to be $V_{\text{low}} = 340$ km/s. The average velocity of the CME between 16.6R_S and the Earth's orbit is ~740 km/s and the *in situ* plasma velocity there is ~450 km/s, implying strong deceleration of the CME at distances greater than 16.6R_S.

Figure 1 describes a sequence of the events, recorded after the generation of the coronal mass ejection on 13 May 2000 at 22:22 UT. In this time at the spacecraft GOES-10 was observed the maximum of the radiation flux S_X in the X-band (Fig. 1a). With the time delay about of 0.92 hr were recorded the two maxima of the bandwidth of the spectral broadening of the radio signals of the CASSINI spacecraft at the radio ray path spaced 2.3 solar radii from the Sun (Fig. 1b). Within 2.35 hr after a registration of the spectral broadening maximum (or 3.27 hr after S_X maximum) was observed the maximum of the intensity of the frequency fluctuations of S-band signals of the GALILEO spacecraft, which sounded the plasma flows at heliocentric distances about of 16.6 solar radii (Fig. 1c). Finally, in Fig.1d are presented the measurements results of plasma density N, which were carried out by the plasma instruments of the fourth spacecraft – the WIND satellite. The real times of the each event (days of 2000) are shown along the horizontal axis.

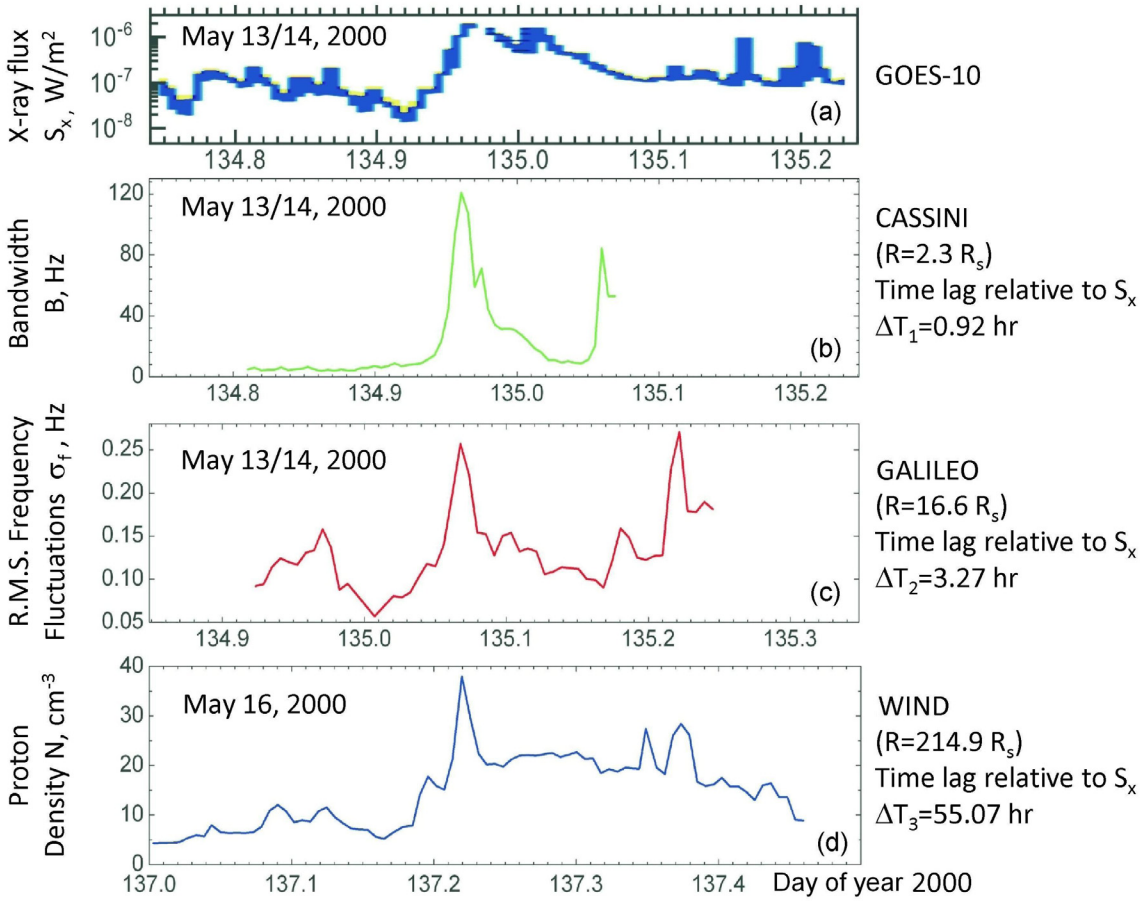

Figure 1: Variations of the X-ray flux of the Sun S_X (a), spectral broadening bandwidth B (the spacecraft CASSINI) (b), intensity of the frequency fluctuations σ_f (spacecraft GALILEO) (c) and plasma density near the Earth (spacecraft WIND) (d).

GOES-10 data: http://www.swpc.noaa.gov/ftpdir/warehouse/2000/2000_plots/

WIND data: http://ftpbrowser.gsfc.nasa.gov/wind_swe_2m.html

The presented in Fig. 1 data show that the temporal changes of the spectral broadening bandwidth B, intensity of the frequency fluctuations of the GALILEO S-band signals σ_f and plasma density N exhibit the same behavior: there is a strong maximum in the leading part of the plasma formation and after 2.3–2.6 hr is registered the second maximum of lesser level. Finally, at time lag about of 3.6 hr relative to main maximum the frequency fluctuations σ_f and plasma density N display the third maximum (the spectral broadening in this time interval was not investigated). A similarity of the temporal dependencies presented in Fig. 1 suggests the qualitative conservation of the radial structure of the coronal mass ejections for the wide range of the heliocentric distances at its motion from the Sun. The time lag between events provides a possibility to determine the velocity of the perturbed plasma formation classified as the coronal mass ejection for different heliocentric distances.

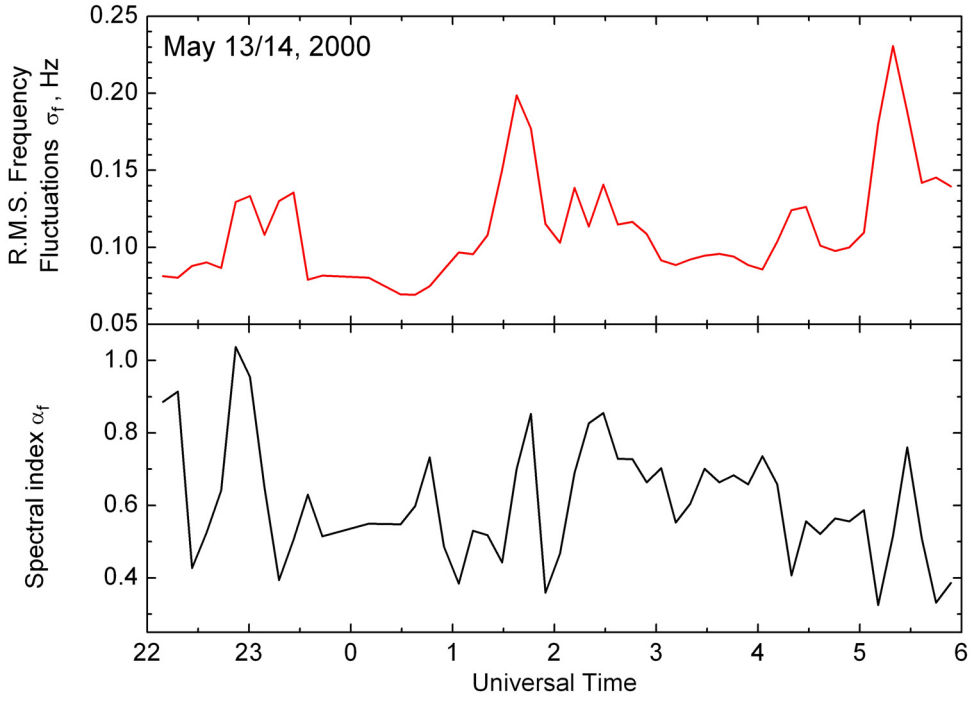

Figure 2: Intensity of the frequency fluctuations (upper panel) and spectral index of the temporal spectra of the frequency fluctuations of the GALILEO signals on 13 and 14 May 2000.

The time lag $\Delta T_1 = 0.92$ hr between maxima of the spectral broadening bandwidth and flux of the X-ray radiation S_X gives the average velocity of the CME motion $V_1 = 340$ km/s for the heliocentric distances between 1 and 2.3 solar radii R_S. A comparison of the fluctuation effects for radio ray path *CASSINI-EARTH* and radio ray path *GALILEO-EARTH* permits to conclude that the velocity of the CME for heliocentric distances between 2.3 and 16.6 solar radii was very high: $V_2 = 1180$ km/s. The spectral analysis of the frequency fluctuations of the GALILEO signals permitted to reveal a further feature of the plasma flows, concerning to coronal mass ejection. In Fig. 2 are presented temporal dependencies of the intensity of the frequency fluctuations σ_f and spectral index α_f of the temporal spectra of these fluctuations. It is seen that the enhanced values of the frequency fluctuations σ_f are accompanied by the enhanced values of the spectral index α_f.

2. Measurements of frequency fluctuations in radio signals generated by the GALILEO spacecraft from January 6 to 11, 1997 were analyzed . The passage of a coronal mass ejection observed by the SOHO/LASCO coronograph on January 6, 1997 through the radio-communication path between the spacecraft and ground station was recorded. This ejection is of particular interest, since it was the first event of this kind to be traced in real time, from the generation of the ejection on the Sun to its intersection with the Earth's magnetosphere and ionosphere. The disturbance was accompanied by a global compression of the Earth's magnetosphere, a strong density increase in the magnetospheric plasma sheet, the

approach of this sheet to Earth surface, substantial increase in the plasma density, which reached a maximum value of 185 cm^{-3} – unprecedented for Earth's orbit.

The transit of a CME across the path between the Earth and the GALILEO spacecraft in mid-January 1997, when the path had a heliocentric distance of about 32Rs, was accompanied by a number of radio effects:

- an increase by a factor of two to three in the frequency fluctuation intensity, which persisted 3 hr;
- an increased index for the temporal energy spectrum of the frequency fluctuations immediately behind the leading front of the ejection;
- a reduced spectral exponent after the passage of the leading part of the disturbance;
- the presence of two peaks in the cross-correlation function of the fluctuations;
- an increased mean frequency of the signals.

The maximum density in the leading part of the plasmoid exceeded the background value by more than an order of magnitude. The existence of two maxima in the cross-correlation function was due to the simultaneous presence of a quiescent and a disturbed stream in the line of sight, whose density and turbulence maxima were spatially separated. The radio-sounding observations of plasma disturbances in a region located east of the Sun preceded the recording of the corresponding disturbances in near-Earth space by 2–2.5 days.

It was established a tendency for an increase of the spectral index of the frequency fluctuations at an increase of their intensity, connected with the emergence of the disturbed plasma formation at the radio ray path. It is shown that the comparison of the coronal sounding data with the optical observations near the Sun and *in situ* plasma measurements near the Earth provides a possibility to determine the velocity of the CME at different distances from the Sun.

2.1.3.2. Radiophysical methods for satellite remote sensing of layered, wave, and turbulent structures in the atmospheres of the Earth and Venus

1. Determination of the absorption in the trans-ionospheric *satellite-to-satellite* communication links and method for location of the plasma layers in the lower ionosphere

A connection between the phase acceleration, Doppler frequency and intensity variations of radio occultation (RO) signal is discovered by means of the theoretical consideration and experimental analysis of the radio-holograms registered during CHAMP, FORMOSAT-3 and other low orbital satellites missions. The radio-holograms have been obtained by means of registration of the high-precision signals of satellites of the GPS navigational system during the radio occultation experiments. The discovered connection gives a possibility to

recalculate the phase acceleration (or Doppler frequency) to the refraction attenuation. This is useful for estimation of the absorption of radio waves in the trans-ionospheric communication links. A method is presented for estimation of the absorption coefficient in the radio occultation communication links satellite-to-satellite (Fig.1). The experimental investigation of the absorption of the centimeter radio waves by clouds and water vapor has been provided and the attractive potentialities of RO method for monitoring of the vertical distribution of water vapor and clouds has been demonstrated. A new phase acceleration/intensity ratio technique is developed for locating the tangent point on the ray trajectory in the ionosphere. This technique allows one to determine the height and inclination of layered plasma structures (including sporadic Es layers) in the ionosphere. This method is validated by measuring the location of the tangent points and estimation of the electron density in the atmosphere and ionosphere by means of analysis of the CHAMP RO data (Fig. 2–4).

Presented phase acceleration (Doppler frequency)/intensity ratio technique appears to provide a new method to locate layered structures in the ionosphere. This method is validated by use of FORMOSAT3 RO data. Recent GPS/MET, SAC-C, and current CHAMP, GRACE, FORMOSAT-3 RO missions provide a growing database for determining the location and estimation of the electron density distribution in the layered plasma structures in the ionosphere. Comparison with ionosondes data is desirable for further derivation and revealing the boundary of application of the suggested method. The application of this and other new techniques will generate a more extensive body of information on plasma structures and natural processes in the ionosphere and their connection with processes in magnetosphere and in interplanetary space.

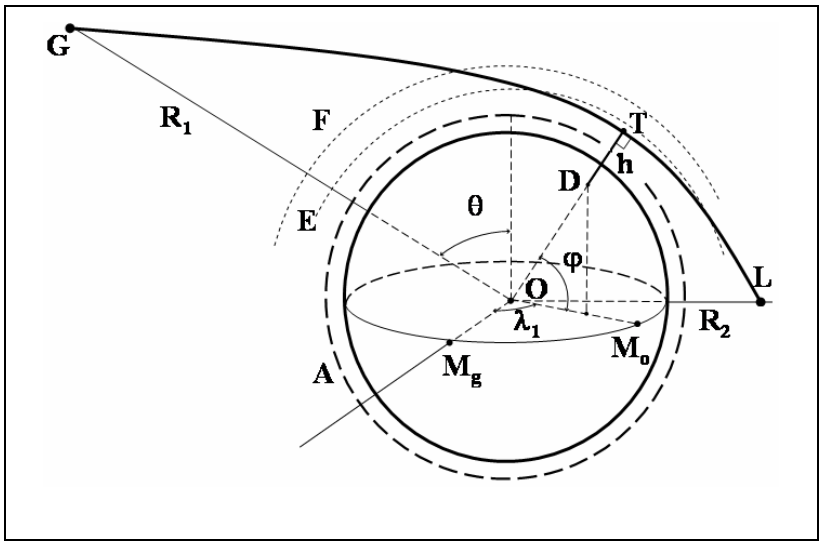

Figure 1: Geometry of RO experiment: *O* is the Earth center; *L* is the receiving satellite, *G* is the navigational satellite; *h* is the altitude of the tangent point of the ray trajectory GTL; *DT* is the altitude interval for measurements of vertical profiles of physical parameters in the atmosphere (A) and ionosphere (E, F).

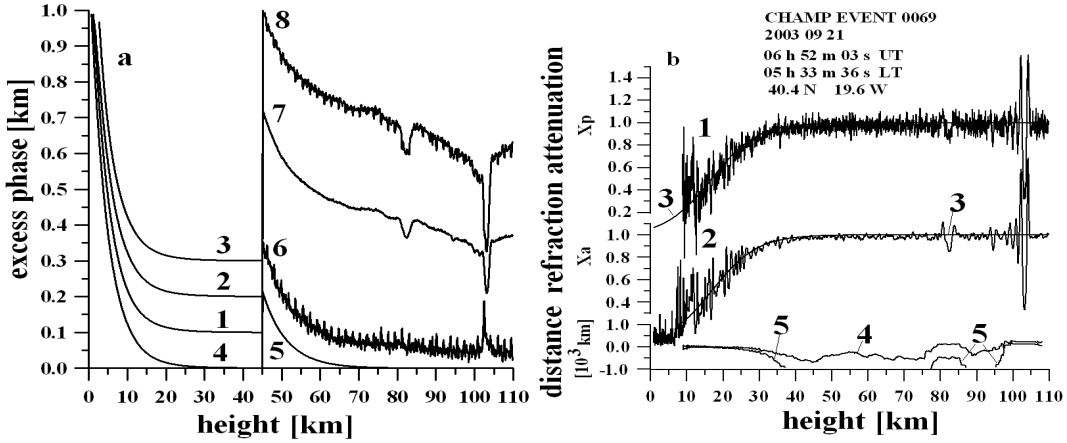

Figure 2: *a* — the excess phase changes at frequencies F1 and F2 (curves 1 and 2), connected with influence of the ionosphere and atmosphere, as functions of the perigee height of the ray trajectory GTL. The curves 1 and 2 are displaced for comparison, respectively, on 100 and 200 m, curve 3 is obtained from the phase excesses at frequencies F1 and F2 by use of ionospheric correction. Curve 3 describes the phase path excess, corresponding to the neutral atmosphere, and displaced by 300 m for comparison with curve 4, calculated for a standard model of the atmosphere. Curves 1–4 describe changes of the phase path excess below 45 km altitude. Curves 5–8 describe variations of the phase path excess at altitude above 45 km. Curves 5–8 are scaled by factor 1000. Curves 5 and 6 describe the contributions of the standard neutral atmosphere, calculated by use of the standard model of the atmosphere and by means of the ionospheric correction of the experimental data, respectively. Curves 7 and 8 correspond to the experimental altitude dependence of the phase path excess at frequencies $F1$ and $F2$. Curves 6, 7 and 8 are displaced for comparison on 5, 30 and 50 cm, respectively; *b* — comparison of the phase acceleration variations, recalculated to the refraction attenuation X_p (curve 1), and refraction attenuation, found from intensity of the RO signal X_a (curves 2), at the first frequency $F1$ of the navigational system GPS.

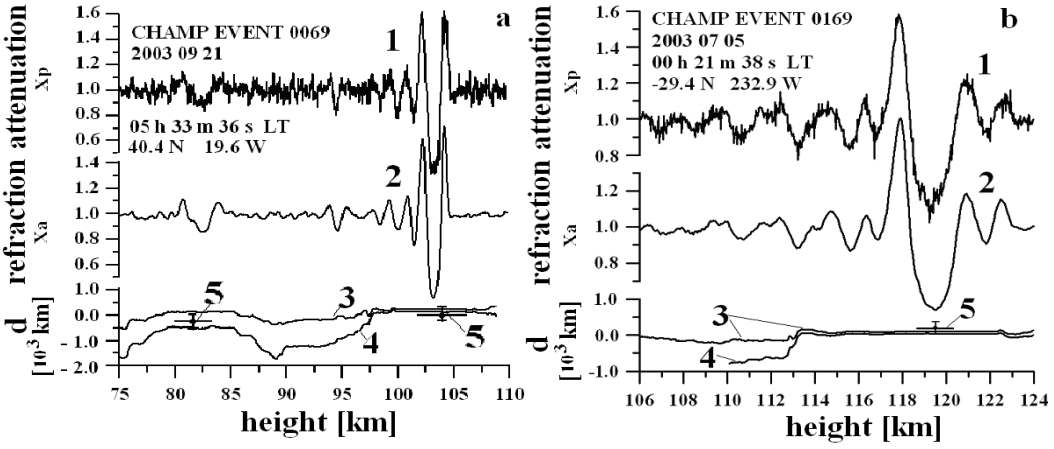

Figure 3: Comparison of the refraction attenuation X_p, recalculated from the phase acceleration variations *a*, and refraction attenuation X_a, found from the amplitude data at the frequency $F1$ of the navigational system GPS (curves 1 and 2), and results of determination of the distance *d* from the tangent point to the ray perigee T (curves 3 and 4). The data correspond to the CHAMP events N 0069, September 21, 2003, 40.4° N 19.6° W (panel a) and N 0169, July 05, 2003, 29.4° S, 232.9° W (panel b). Vertical and horizontal short length 5 correspond to the experimental errors.

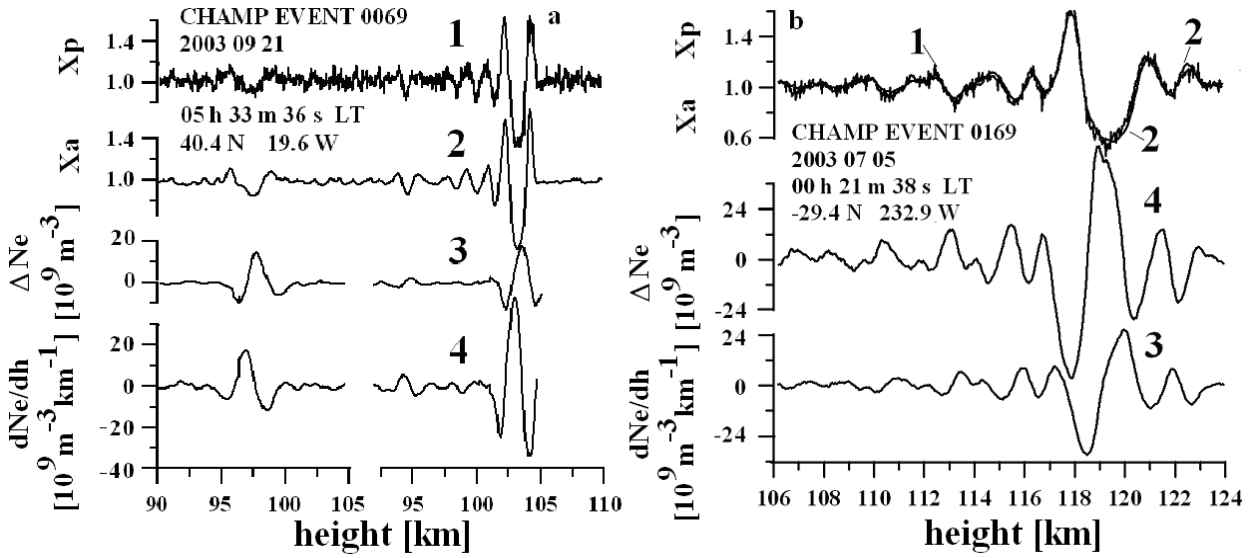

Figure 4: Comparison of the refraction attenuation X_p, recalculated from the phase acceleration variations a, and refraction attenuation X_a, found from the amplitude data at the frequency F1 of the navigational system GPS (curves 1 and 2), and the retrieved variations of the electron density and its vertical gradients as function of the corrected altitude in the ionosphere. The data correspond to the CHAMP events N 0069 and 0169.

2. Geographical distribution of the intensive sporadic E_S layers during period of reducing in solar activity in 2003-2007 by use of CHAMP and FORMOSAT-3 satellites data

The geographical distributions of the intense ionospheric events (with the S_4 index greater than 0.12) for all types of the amplitude scintillations in the CHAMP RO signals at 1575.42 MHz are demonstrated in Fig. 5 and 6. Note that these distributions may be linked to changes in sampling by CHAMP. Our analysis showed that the satellite coverage over relevant periods was nearly regularly distributed. Therefore these distributions contain important information on the spatial dependence of the strong ionospheric events during the considered time intervals. The distributions of the ionospheric events indicate that they are concentrated in some regions (e.g., the equatorial and geomagnetic North and South polar zones in Fig.5 and 6. High activity in some equatorial regions may be connected with the evening ionospheric disturbances that arise after sunset, 20–24 hrs local time, in accordance with the earth-based measurements reviewed earlier. Note that geographical distributions of the night- and day-time events are very different. The daytime events prevail in the North and South Polar zones. The nighttime events are concentrated mainly in the equatorial and moderate latitude areas. The most significant difference in the geographical distributions of night-time (open circles) and day-time (closed circles) events is observed in April 2004 (Fig. 6, right bottom panel), and in October 2002 (Fig. 5, right top panel). This indicates the different origin of the daytime and nighttime plasma disturbances in the ionosphere. The number and geographical distributions of intense ionospheric events depend on time. The maximal number of events can be seen in May-July, October-December 2001 (Fig. 5, left top panel, Fig. 6, left and right top panels,

respectively). The minimal number of events corresponds to October 2002 (right top panel in Fig. 5), and April and July 2004 (bottom right panels in Fig. 5 and 6, respectively). As seen in Fig.5 and 11, the number of intense ionospheric events and their intensity decreases as time from May, July, and October 2001 to April-July 2004. This is possibly connected with a gradual diminishing in solar activity from maximal values in 2001 to minimal values in 2004.

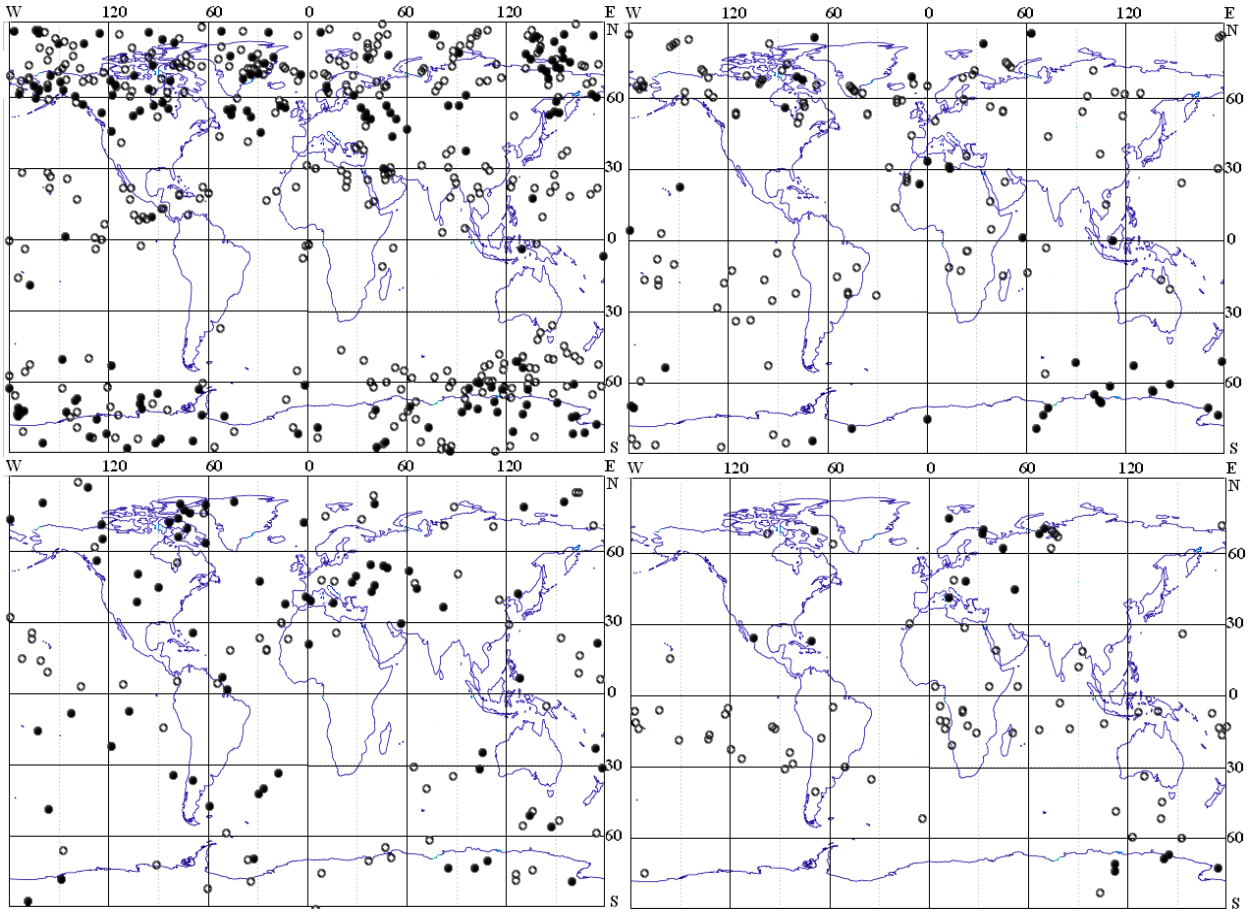

Figure 5: Maps of intense ionospheric events with S_4 index greater than 0.12 for October 2001 (left top panel), October 2002 (right top panel), October 2003 (left bottom panel), and April 2004 (right bottom panel). The circles show the geographical position of the tangent point *T* (Fig. 1). The daytime events are marked by closed circles (local time 08–20 hours) and the nighttime events are indicated by open circles (local time 20–08 hours).

One can estimate the seasonal dependence in the geographical distributions of intense ionospheric events registered by the CHAMP satellite (Fig. 6). The seasonal displacement of the regions with intense ionospheric events in the south and north directions during the periods from May-July 2001 (Fig. 6, left top panel) to November-December 2001 (Fig. 6, right top panel), and to September 2001 (Fig.5, left top panel) can be noted. The number of intense ionospheric events increases in the North Polar Region with latitudes greater than 60º N as the time changes from May-July 2001 to November-December 2001. Also the number of

intense ionospheric events decreases at the moderate latitudes in the 30º-60º N interval for the same time interval. The possible cause of the seasonal dependence may be connected with two important mechanisms governing the ionospheric disturbances. The first one is the ionizations caused by energetic electrons in the Polar Regions; the second is due to solar radiation. The influence of solar radiation has a seasonal character because ionization in the ionosphere follows annual and diurnal motion of the ionospheric sub-solar point. As follows from this consideration, the amplitude part of the RO radio holograms is appropriate for studying the geographical and seasonal distributions of the ionospheric disturbances with global coverage and establishing their connections with solar activity.

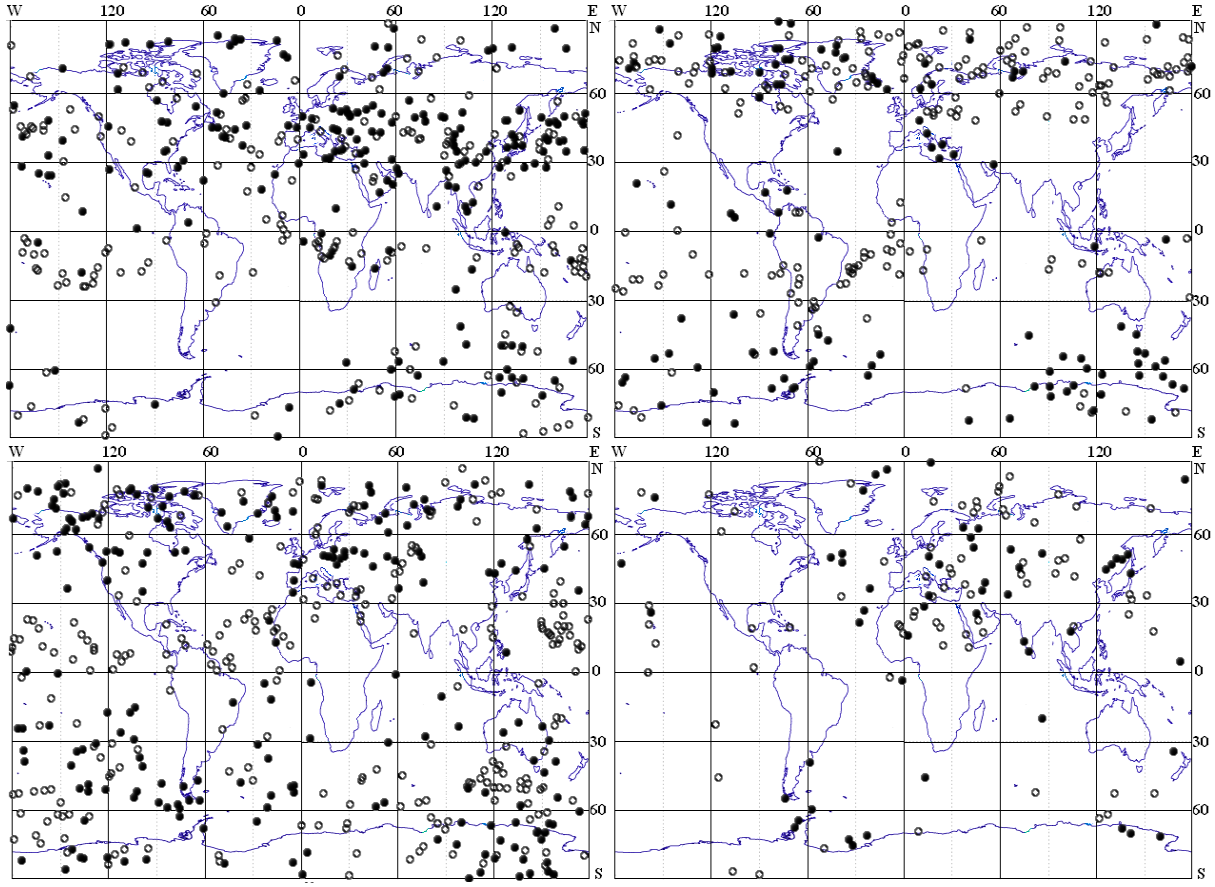

Figure 6: Seasonal dependence of the global distribution of CHAMP RO events with intense amplitude variations (with magnitude of S_4 index greater than 0.2) for periods May 14 – July 14, 2001, (left top panel), November–December 2001 (right top panel), October 28 – November 26, 2003 (left bottom panel), July 2004 (right bottom panel). The daytime events are marked by closed circles (local time 08–20 hrs); the nighttime events are indicated by open circles (local time 20–08 hrs).

An example of geographical distribution of FORMOSAT-3 RO events with intense amplitude variations (with magnitude of S_4 index greater than 0.12) for period 01, 11 and 12 June 2006 is shown in Fig. 7. The concentration of intensive sporadic *Es*

layers is seen in the moderate latitudes of the Northern Hemisphere, where the zenith solar angle is minimal. Therefore the main mechanism of the origin of intensive sporadic Es layers is the ultraviolet solar emission. The geographical distribution of intensive sporadic *Es* layers is nearly uniform, this indicates on different mechanism connected with plasma transportation in the ionosphere.

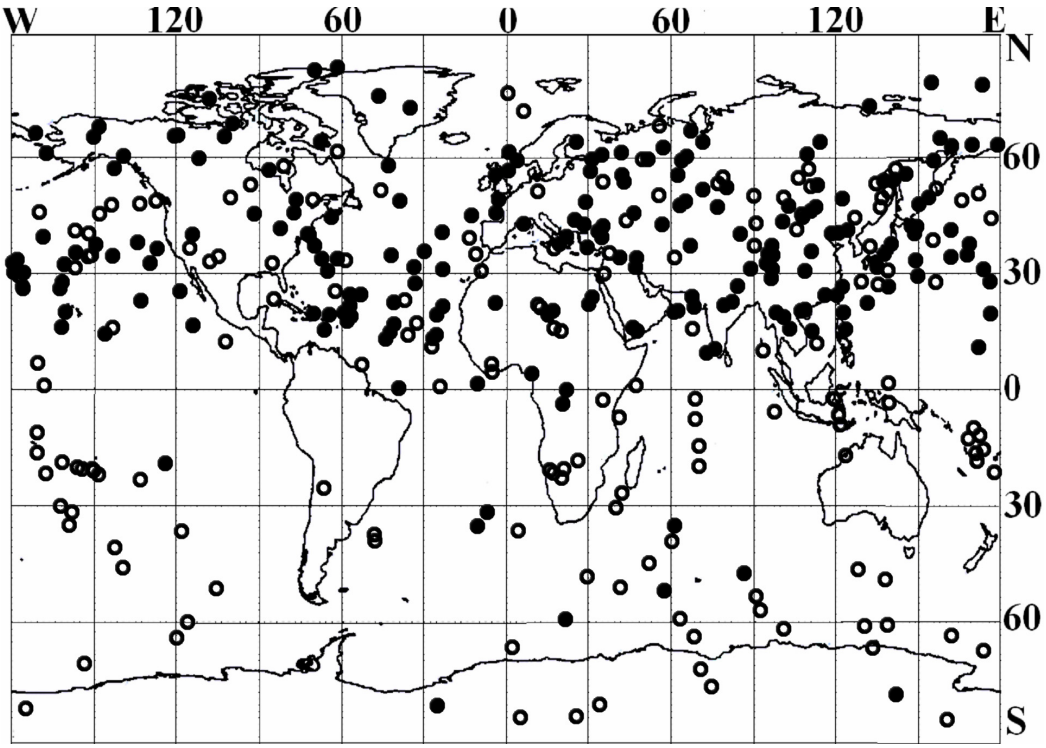

Figure 7: Geographical distribution of FORMOSAT-3 RO events with intense amplitude variations (with magnitude of S_4 index greater than 0.12) for period 01, 11 and 12 June 2006. The daytime events are marked by closed circles (local time 08–20 hrs); the nighttime events are indicated by open circles (local time 20–08 hrs).

The scintillations of the amplitude and phase of decimeter radio waves in the radio occultation satellite-to-satellite links have been studied and the features of the plasma small-scale irregularities in the equatorial and polar regions are analyzed. The vertical profiles of the electron density and statistical characteristics of sporadic Es in the different regions are obtained. It is shown that the intensive small-scale plasma irregularities and intensive sporadic Es layers in the lower polar ionosphere are observed immediately after arriving of the bow shock wave in the solar wind.

3. New method for global monitoring of internal atmospheric waves

Internal gravity waves (IGW) play a crucial role in determining the circulation and mean state of the atmosphere. IGW can occur at all altitudes in the Earth atmosphere and are important for several reasons: They can transport energy and

momentum from one region of the atmosphere to another; they can initiate and modulate convection and subsequent hydrological processes; they disturb the balanced state through injection of energy and momentum into the mean flow; and, when the waves break, turbulence hazardous to aviation is generated and chemical species are mixed; IGW and wave breaking may be responsible for the formation of the ionospheric sporadic E layers.

The advantage of using radio occultation satellite measurements for gravity wave research is their extensive geographic and temporal coverage. It allows seasonal and latitudinal variations of gravity wave activity to be identified. It was assumed earlier that it is impossible to estimate gravity wave parameters such as the intrinsic frequency or phase velocities that are necessary to quantify the IGW effects because the observed quantities are only temperature and atmospheric density. We have proposed a new technique that can be used to derive all wave parameters from only a single vertical temperature profile without requiring any additional information not contained in the profile.

The criterion for the positive identification of the observed temperature fluctuations as wave-induced has been formulated. An analysis technique for the derivation of the IGW intrinsic frequency and other wave parameters has been proposed. This technique is based upon a comparison of the experimental and theoretical values of the relative amplitude threshold, which is defined as the wave amplitude required for shear instability in the atmosphere. In the case when the analyzed fluctuations are positively identified as wave-induced, then the intrinsic frequency of the monochromatic gravity wave can be determined from only a single vertical temperature profile. The practical application of the proposed method has been demonstrated by using the GPS/FORMOSAT radio holographic retrievals of temperature profiles in the Earth stratosphere. We assume that this method can be applied for the analysis of vertical temperature profiles measured by other techniques (Rayleigh lidar, rocket and radiosonde soundings etc.).

4. Layering in the upper cloud region of the Venus from radio occultation data

An essentially new method for the analysis of radio occultation data has been developed that can be used to identify and separate fluctuation radio effects related with the influence of thin regular atmospheric layers and random irregularities (turbulence). This method was used for the analysis of 32-cm radio wave amplitude fluctuations observed during the radio occultation experiments conducted in the Venus northern polar atmosphere by the spacecraft VENERA-15 and -16 (October 1983). The following results about small-scale structure parameters and their time evolution inside the upper cloud region of the planet atmosphere were obtained:

- Layering of the upper cloud region has been observed in the Venus northern polar atmosphere in the period from 23 to 25 October 1983. This has been confirmed by the physically significant correlations of amplitude fluctuations (correlation coefficients ~0.5-0.7) revealed in the three sounded regions at

altitudes between 59.0 and 61.5 km. It was found that the vertical thickness of the thin regular layers ranges from 0.5 to 0.9 km, their horizontal extension in the meridional direction can exceed 180 km, and the lifetime of small-scale irregularities is 2 days or more.

- The separation of total amplitude variances and power spectra on the regular and random components allowed studying the time evolution of small-scale structures in the Venus atmosphere. The random variances were 14, 45 and 58 % from the total variances 23, 24 and 25 October, respectively, and they indicate on the large temporal variability of the random environment. The regular variances had remained nearly constant for the three radio soundings, and these showed that both the layer growth and layer decay were not observed in the period from 23 to 25 October 1983.

2.1.3.3. Determination of the ionosphere electron concentration by the radio sounding method

The radio sounding method for a study of the Earth ionosphere based on use of global navigating systems and the decision algorithms of inverse problems is developed. It is shown, that the radio sounding method can be used for construction of modern system monitoring of the ionosphere intended for the decision of the forecasting tasks of the radio wave propagation conditions and the subsequent application of these data for an estimation of operating conditions of radio engineering devices in communication systems and satellite systems of a radiolocation, space navigation and a geodesy.

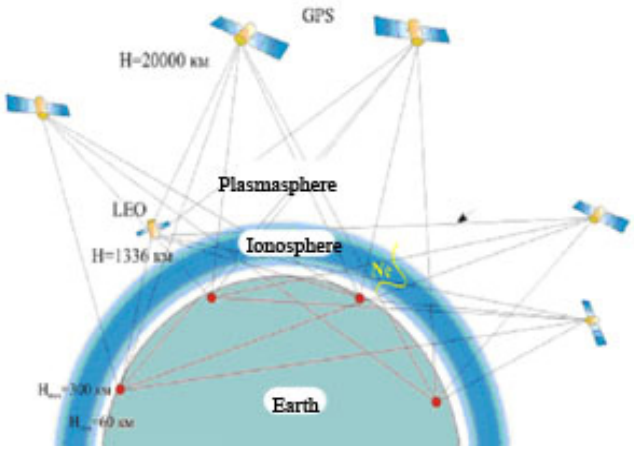

Figure 1: The configuration of satellites used in radiophysical methods of sounding.

Practical realization of a method is based on use of measurements of the signal parameters on a line «the satellite-ground» on observation from one point (Fig.1). In this case the corresponding integral equation of the first order has no analytical decision and demands development of the inversion technique in a class of the so-called ill-posed problems. The decision algorithm of the ill-posed inverse problem,

supposing reception of ionosphere parameters along subionospheric trajectory points is offered for an effective use of radio sounding method in system of the automated determination of high-altitude distribution of electron concentration.

On the basis of simulation results it is shown, that root-mean-square error of definition of high-altitude electron concentration distribution of the Earth ionosphere is equal $\delta N = 0.02$ NU ($1\text{NU} = 10^6$ cm^{-3}). It makes less 2ю5 % from value of the electron concentration maximum. Directly, maximum value of an ionosphere electron density is determined with accuracy better 2 %: the difference between modeled value and value, restored from the decision of an inverse problem makes $\delta N = 0{,}014$ NU. Algorithms and the software intended for the decision of a inverse radio sounding problem on a line the satellite-ground with the purpose of high-altitude distribution determination of the Earth ionosphere electron concentration with the resolution on height from 5 up to 40 km and with time step of 30 seconds along subionospheric trajectory are developed and approved on the real measurements (Fig. 2).

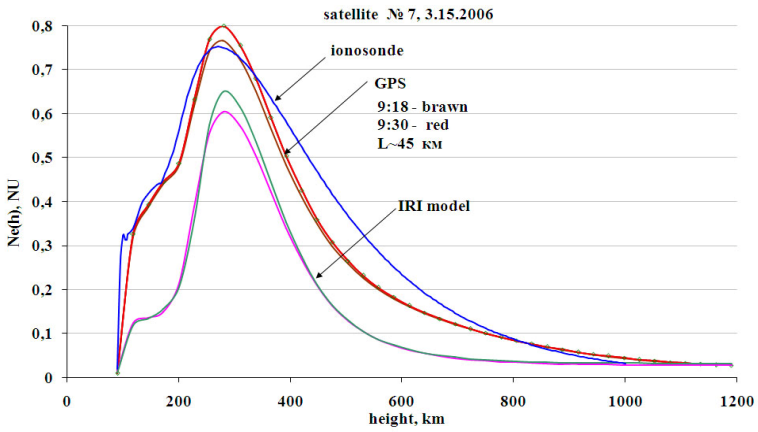

Figure 2: The results of comparison of restoration on GPS satellites observations with the ionosonde data (Grahamstown, South Africa)

It is shown, that signals application of navigating satellite systems enables to determine parameters of an ionosphere practically for any region of the Earth surface (Fig. 3). This opportunity is based on use of the universal geodetic receivers, allowing accept signals of navigating satellites practically in any point of a terrestrial surface. The operative range of one such receiver covers area which radius can make more than 1000 km.

The basic opportunity of determination of azimuth-time variations of the Earth ionosphere parameters on one-item ground measurements is shown by results experimental data processing of the GPS measurements (Fig. 4). The reconstruction opportunities of an existential structure of an ionosphere on the basis of radio sounding method are investigated. The opportunity estimation of

construction of two-three-dimensional structure of regular parameters of an ionosphere is given and results of experimental realization are presented.

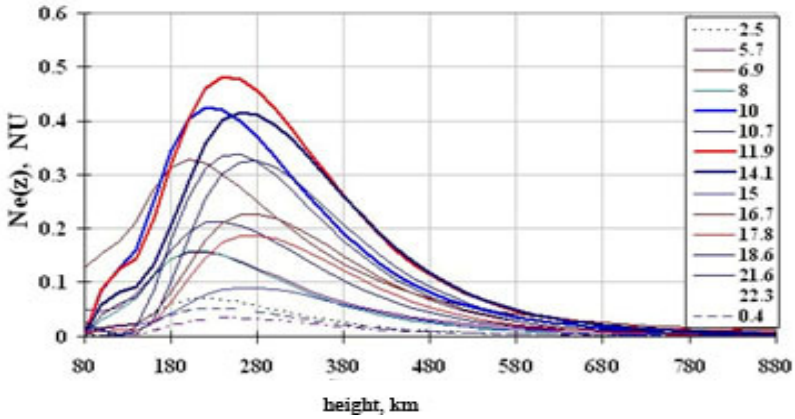

Figure 3: Temporal variations of high-altitude structures of the electron concentration, detected by GPS satellites data

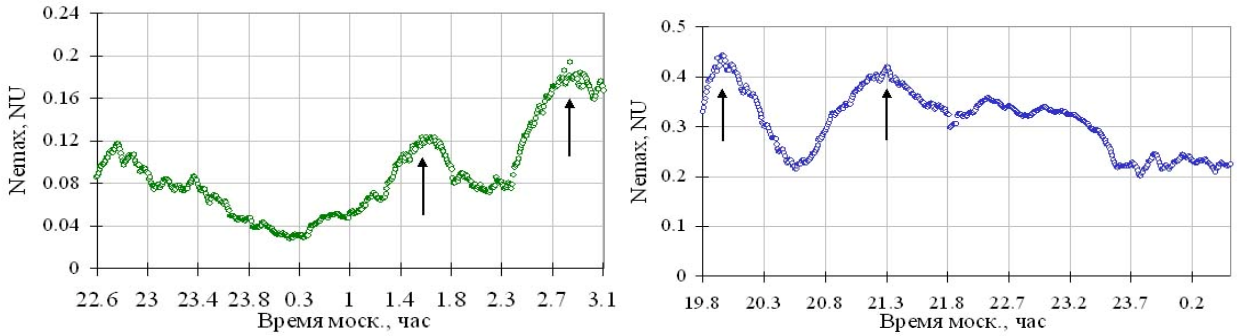

azimuth 286-290-182°°°°°°°°°°°°°°°°°°°°°°°°°°°°°°°azimuth 196-78-86°

Figure 4: Variations of an electron concentration maximum of the ionosphere received on observation of two satellites for crossed azimuthally directions.

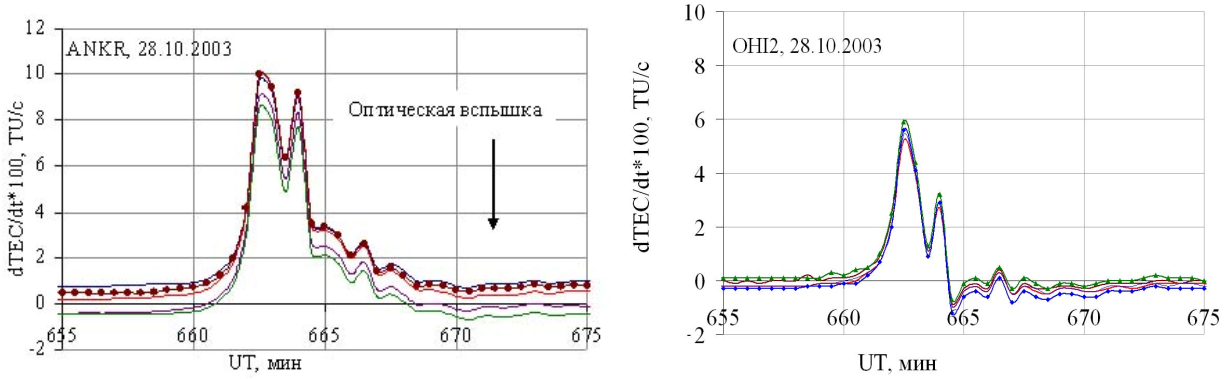

Figure 5: The ionosphere response to geomagnetic effect of solar flare on October, 28th, 2003 for northern and southern hemispheres.

The application efficiency of this method is proved at the ionospheric perturbation detecting during heliophysical processes on the Sun and anthropogenous effects on the Earth. It is shown, that the form of the ionosphere response on direct effect of solar flare has different structure in Northern and Southern hemispheres of the Earth (Fig. 5).

On the basis of real data processing the basic opportunity of ionospheric variations research by a radio sounding method is proved to variability during seismic events. Estimations of the space-time resolution of this method on a line the satellite-ground are obtained at ionosphere parameters definition with reference to a problem of seismo-ionospheric variations detecting. It is shown, that for localization of ionospheric variation area it is necessary to spend monitoring with the resolution on the Earth surface approximately 200 on 200 km.

The ionosphere monitoring during seismic events generation in the Earth various regions and at different level of geomagnetic activity are carried out. It is shown, that seismoionospheric variations can be effectively registered at use of radio sounding method on a line the navigating satellite-ground. On the results of data processing received with use of navigating systems, it is proved, that above an epicenter of the future earthquake there is the existential course disfunction of the ionosphere electron concentration. Such updating of a structure is observed 1-3 day prior to forthcoming event (Fig. 6, 7). It is shown, that on the basis of the analysis of existential electron concentration structure it is possibly to predict a place of the future earthquake epicenter.

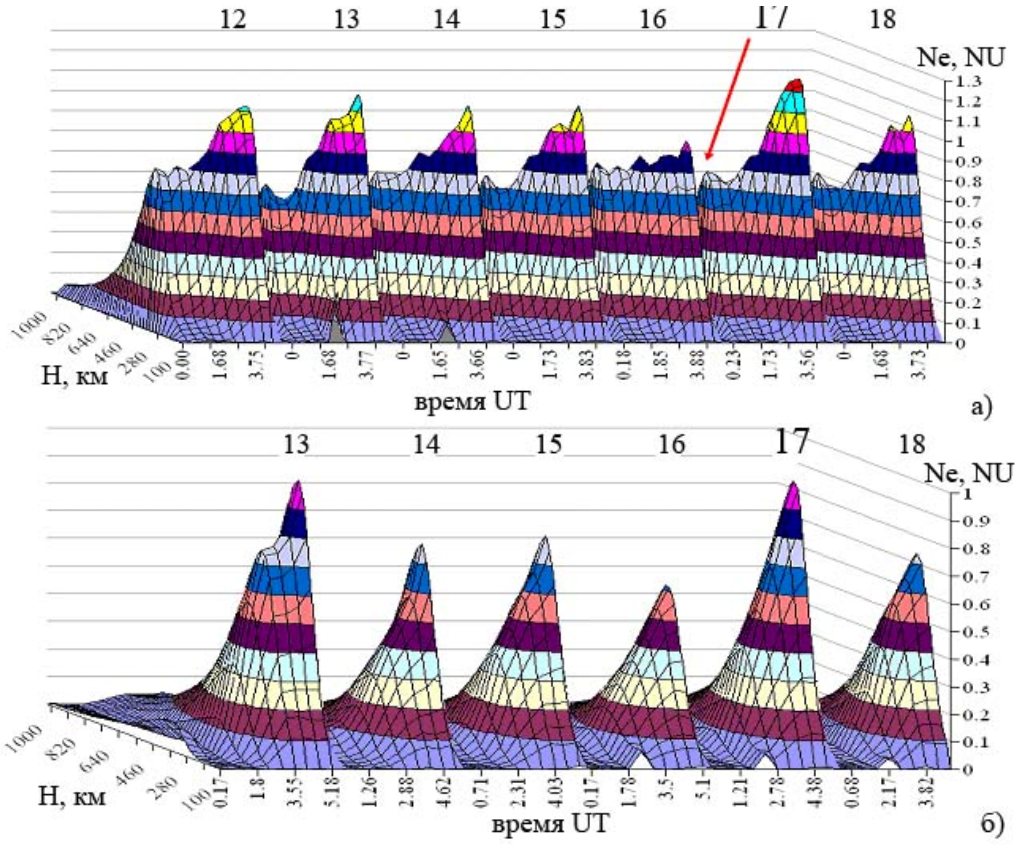

Figure 6: The electron concentration profile (3D-representation) near (a) and far away (b) an epicenter of earthquake (Turkey, Izmir, on August, 17th, 1999).

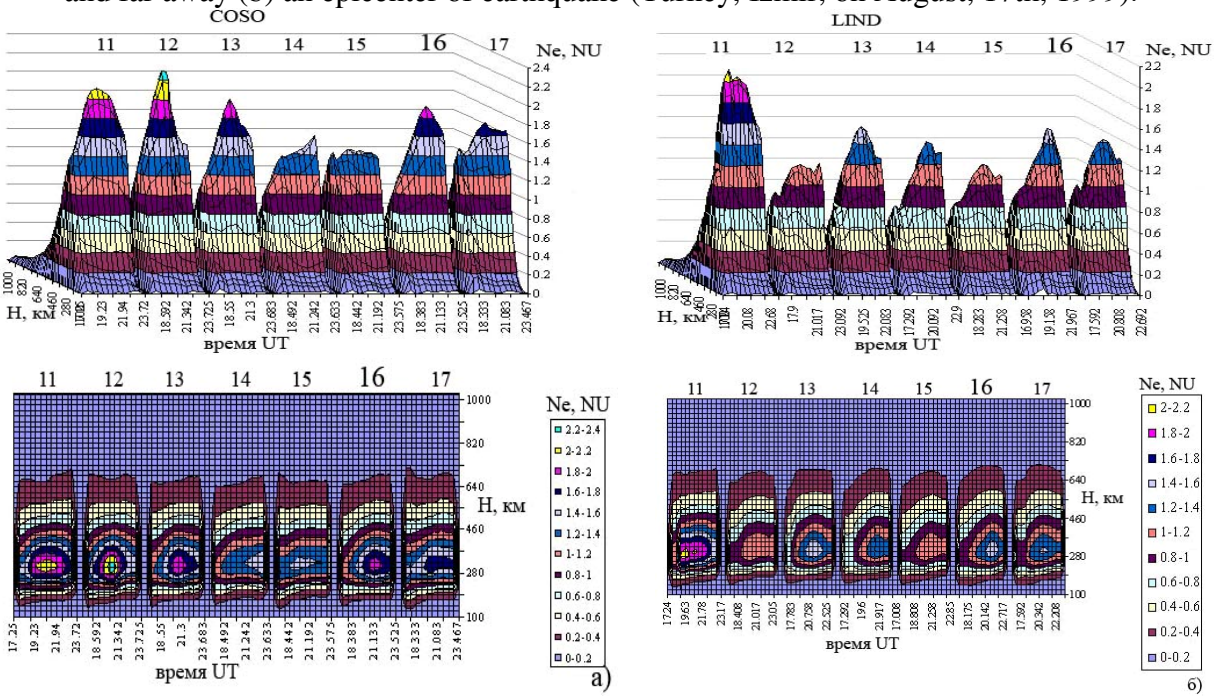

Figure 7: The electron concentration profile (3D-representation) and their bidimensional representation (2D) near (a) and far away (b) an epicenter (USA, Hector Mine, on October, 16th, 1999).

On the basis of the use of existing ground equipment and the decision method of a inverse ill-posed problem the construction efficiency of the automated data processing technology, intended for continuous monitoring an ionosphere by signals of navigating GPS and GLONASS systems in real time is shown.

2.1.4. V.I. VERNADSKIY INSTITUTE OF GEOCHEMISTRY AND ANALYTICAL CHEMISTRY OF THE RAS

2.1.4.1. Magellan: Mission of USA (1990–1994)

1.1. *Geological analysis and mapping of radar images of Beta Regio*, *Venus*, *has been done*. Beta Regio includes 2000×2500 km volcanic-tectonic uplift and the adjacent regional volcanic plains. In this work 8 material and 3 structural units have been identified and mapped. It was shown that their mutual relations are in agreement with hypothesis of formation of volcanic-tectonic uplift due to activity of large mantle diapir. Time duration of this activity has been estimated – several hundred million years. Results of this work have been published in international journal Icarus. The geologic map made as a result of this study (Figure 1) had been accepted for publication by the US Geologic Survay.

The work has been done jointly with Brown University, Providence, RI, USA.

1.2. *Geological analysis and mapping of radar images of Militta Regio*, *Venus*, *has been done*. Geology of this region is described by 11 material and structural units, stratigraphic contents of which are permanent within the mapping area. The main feature of this region is presence of one of the largest coronae on Venus (Quetzalpetlatl Corona, 800 km in diameter) which tops the domical uplift in the eastern part of Lada Terra. The uplift and the corona are powerful sources of young volcanism related to the mantle material upwelling. Volcanic centers are located at the edge of deep regional depression of Lavinia Planitia, formation of which was due to the mantle material downwelling, which predated the volcanism of the Lada Terra uplift. Results of this work have been published by the US Geologic Survey as the 1: 5 000 000 Map I-2832 (Fig. 2).

The work has been done jointly with Brown University, Providence, RI, USA.

1.3. *Based on multi-year studies of Venus geology a new approach has been suggested for selection of landing sites on this planet for spacecraft*, *which have to study composition of surface materials*. For that on the global map of the planet have been outlined zones, where in the surface material with high probability is present a material of ejecta from distant upwind (on Venus there are permanent strong east-west winds) impact craters. These ejecta contain materials of the geologic complexes about which nature and age we may only guess. Meanwhile to understand geological-geochemical processes on Venus, first of all, one needs to make geochemical analyses of the materials which are observed on the surface and for which morphologic evidence of their nature has been acquired. We have suggested 13 perspective landing sites (Figure 3) which are outside of zones of uncontrolled pollution and representing five most interesting and still not studied

geologic complexes. The work results have been published in the international journal Planetary and Space Science.

The work has been done jointly with University of Oulu, Finland, and Brown University, Providence, RI, USA.

2.1.4.2. Vega/Giotto, Deep Space, Stardust, Deep Impact: Missions of the USSR, ESA and USA

1.4. *Geologic-morphologic analysis of images of nuclei of four comets* (*Halley*, *Borrelly*, *Wild-1 and Tempel-1*) *showed presence of craters on them*, *probably formed by impacts*, *and a number of landforms with flat surfaces: flow-like features*, *mesas*, *terraces*, *flat floors of craters* (*Fig. 4*). Formation of these landforms was probably due to process of planation in which in a number of cases the key role played collapse of slopes provoked by the ice sublimation and subsequent spreading out the collapsed material. Continuous layers seen in the images of comet Tempel-1 were probably formed at the stage of accretion of protocometary bodies due to crushing of accreting very fluffy cometesimals. A conclusion has been made that surface material of cometary nuclei is essentially reworked by a number of processes that has to be taken into account in planning mission to comets. The work results have been published in Planetary and Space Science and in Solar System Research.

The work has been done jointly with Max-Planck Institute for Solar System Research, Katlenburg-Lindau, Germany.

2.1.5. THE RAS INSTITUTE FOR BIO-MEDICAL PROBLEMS

Research of a functional state of various systems in humans and animals under influence of space flight factors is one of the main questions of space biology and medicine. Significance of such research consists in necessity of building a scientific base in order to design future space flights of longer duration.

4 biomedical experiments in the field of space medicine and physiology — «Sprut», «Pulse», «Pilot», «Hematology» and 2 experiments in the field of space biology — «Cell-to-cell Interaction» and «Statoconia» have been completed in 2006-2007 under realization of the Long-term program of scientifically applied research on the Russian Segment of the International Space Station (ISS).

Experiment «Sprut» — research of liquid mediums' state in human organism under conditions of long-duration space flight (Fig.1). The purpose of this experiment was an obtainment of data on a state of liquid mediums in human organism under conditions of long-duration space flight with the aim of an assessment of adaptation mechanisms' state and improvement of countermeasures against unfavorable influence of weightlessness with reference to flight conditions onboard ISS.

12 Russian cosmonauts of the main ISS crews since the first main expedition have participated in experiment «Sprut».

Figure 1: Performance of «Sprut» experiment onboard ISS during flight.

Development of hypohydration in human organism under conditions of long-duration space flight is shown for the first time; with that the interrelation of intracellular and extracellular fluid volumes demonstrates an even development of fluid deficiency in these liquid sectors of an organism.

Experiment «Pulse» — research of a vegetative regulation of the cardio-respiratory system (Fig. 2).

The purpose of experiment was an obtainment of new scientific information which would deepen the knowledge about cardio-respiratory system's mechanisms of adaptation for conditions of long-duration space flight.

Research of a vegetative regulation of the cardio-respiratory system in flights ISS-6-ISS-13 have shown, that experiment «Pulse» has allowed to receive an important diagnostic and prognostic information on functioning mechanisms of this system under microgravity conditions.

Figure 2: Cosmonaut N.M. Budarin performing the «Pulse» experiment.

Experiment «Pilot» — research showing specific features in regulating psychophysiological state and reliability of cosmonaut's professional activity during space flight (Fig.3). Experiment «Pilot» was conducted with participation of the Russian and American crewmembers of ISS-7-14.

Figure 3: ISS-14 Flight Engineer M.V.Tyurin conducting «Pilot-R» experiment during flight onboard ISS.

At end of experiment recommendations for further perfection of ergonomic characteristics and fixation design of cosmonaut's workplace have been developed.

Experiment «Hematology» — research of morphofunctional properties of blood cells and intensity of erythropoiesis in humans under influence of space flight factors.

The purpose of «Hematology» experiment was an obtainment of new data on the impact of space flight factors on human blood system, an increase of diagnostic and prognostic possibilities, an identification of mechanisms of occurring changes in hematological parameters («space anemia») and development of recommendations for the necessity of usage of preventive and pharmacological means which would eliminate an unfavorable impact of space flight factors on human organism.

Starting from the 6-th expedition on ISS the research of erythrocytes condition has been conducted in the background period, during space flight and in the first two weeks after its completion.

Experiment «Cell-to-Cell interaction» — study of the broad spectrum of events in microgravity conditions related to cellular contacts and, in particular, the functional activity of natural killer lymphocytes (NK) during interaction with a target cell in cell cultures exposed onboard ISS. Experiment has been begun during ISS-7 expedition and continued during the five following visiting expeditions on the «Soyuz» vehicles (Fig. 4).

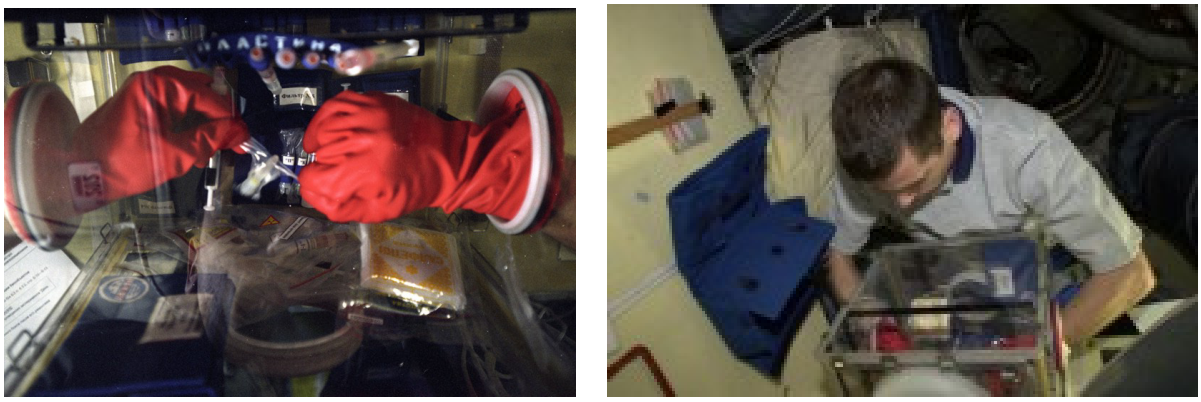

Figure 4: Performance of «Cell-to-Cell Interaction» experiment onboard ISS during flight.

The research task was to study intercellular interaction between natural killer lymphocytes and tumor cells in vitro under microgravity.

«Cell-to-Cell Interaction» experiment has been executed by the Russian cosmonauts of long-duration crews during ISS-7 – ISS-12 within the first and second day after docking. As a result of the conducted experiment it has been established that human NK lymphocytes can recognize and contact target cells (myeloblasts of K-562 line) in suspension during incubation in microgravity; NK lymphocytes can realize their cytotoxic effect during an interaction with highly specific target cells. It was established that human NK cells in microgravity tend to increase cytotoxicity in the process of in vitro incubation with K-562 cells.

Differences in the activity of donor lymphocytes may depend on initial potential capacities of natural killer cells and individual characteristics of the donor.

In «Statoconia» experiment — an assessment of character and dynamics of a neoplasm and growth of statoconia in gastropods (grape snail) in microgravity the solution of problems connected to study of ultrastructure and element structure, morphometry, generation and growth of statoconia after extraction of an «old» statoconia from statocysts was provided (Fig. 5).

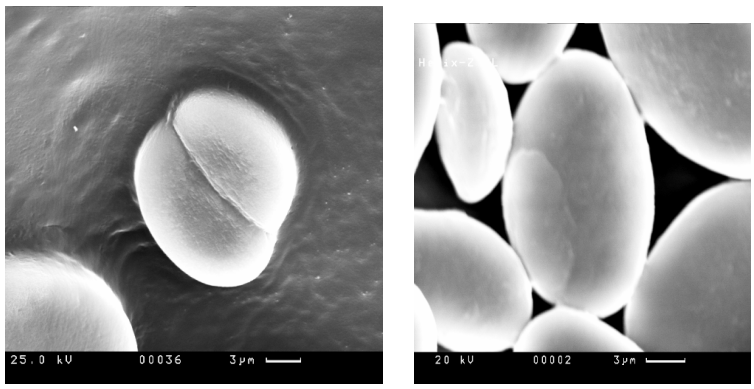

Figure 5: Long exposure in weightlessness (more than 100 days) has led to changes in morphological parameters of statoconia.

In all flight experiments the positive increase of basic morphological parameters in statoconia such as length, width, perimeter and area was shown. With an increase of exposure duration in weightlessness the tendency of their further increase in comparison with control values became apparent. It has been also shown that the basic mineral element giving weight to statoconia is a calcium carbonate in the form of aragonite crystals.

Biological experiments during flights of unmanned (automatic) space vehicles

In year 2007 the flight of SV «Photon-M» N 3 — 12 days (14.09.07-26.09.07) is completed. Launch of SV «Photon-M» №3 has been carried out from cosmodrome «Baikonur». The descent vehicle was landed in the area of Kustanai city (Kazakhstan).

Research in flights of SV «Photon-M» N 3 have allowed to have clear comprehension about laws of adaptation to microgravity for the living systems standing on various levels of phylogenetic development. Experiments with microorganisms, grape snails, newts, lizards and Mongolian gerbils have been conducted during flight. All these experiments were Russian and the Russian Federation State Research Center — Institute of Biomedical Problems, Russian Academy of Science was the executive of these experiments. Many Russian

scientific institutes took part in carrying out pre- and postflight research of biomaterial. The Russian side has also invited experts from NASA to participate in realization of four biological experiments («Receptor», «Regeneration», «Gecko» and «Plasmid» experiments).

Experiment «Rodentia». The number of studies focused on the trial of new biological test model — Mongolian gerbil (Meriones unguiculatus) has been conducted. During postflight research the data on a state of the nervous, muscular, skeletal systems, gastrointestinal tract, visual apparatus and water-electrolytic balance have been obtained. Some differences in reactions of various physiological systems to weightlessness adaptation have been found between rats and Mongolian gerbils with their ability for high osmotic concentration of urine.

Experiment «Receptor». In the experiment with grape snails (Helix lucorum L.) the important role of preproHPeP gene, coding regulatory peptides of hair cells in a statocyst — an organ of gravitation is established. The received results testify that such simple experimental model as a snail can be used for the description of subcellular mechanisms of adaptation in gravireceptors under microgravity conditions.

Experiment «Regeneration». Newts (Pleurodeles Waltlii) are well proved experimental model for studying an impact of space flight factors, first of all an effect of weightlessness and ionizing radiation on processes of regeneration and other functions of an organism. Modifying influence of weightlessness on a process of tissues and cells regeneration (crystalline lens, extremities, tail) is shown in newts through a change in expression of genes FGF and HSP90, which participate in mechanisms of division, differentiation and apoptosis of the cells.

Experiment «Gecko». Research of the oblongated marrow has revealed cytological changes in neurons of vestibular nucleuses in a flight group of lizards-geckoes (Pachydactylus turneri). The obtained results show that bone loss occurs only in animals which are sensitive to mechanical loads. The same laws of adaptation to weightlessness as in mammals are revealed in this experiment.

Experiment «Plasmid». During breeding of microbial strains of E.coli and Streptomyces lividans 66 (pIJ 702) in flight it is established, that in weightlessness conjugated transfer of plasmids pIJ 702 from E.coli cells to Streptomyces lividans 66 cells happens with greater intensity than on Earth and that leads to appearance of a breed with new genetical characteristics.

Following stages of biological experiments realization are planned for 2010 during 30 days flight of SV «Bion-M» №1 and for 2011 during flight of SV «Photon-M» №4. In the scientific program of these flights there will be experiments on various mammals (mice, gerbils), the lower vertebrates (geckoes), molluscums (snails), insects and microorganisms. There is a plan to expand research in biotechnology and astrobiology. At present time negotiations with experts of various space agencies are carried on for their possible participation in the program of implementation of the flight experiments.

2.1.6. D.V. SKOBELTSYN SCIENTIFIC-RESEARCH INSTITUTE OF NUCLEAR PHYSICS OF M.V. LOMONOSOV MOSCOW STATE UNIVERSITY

The results of experimental investigations of Space processes

Measurements of different types of space radiation are conducted on a number of satellites by different devices developed and constructed in NPI MSU on the phase of the solar activity minimum. Experimental investigations on the boards of "CORONAS-F", "Tatiana", "METEOR-3M", International Space Station and "GLONASS" satellites are produced. The great numbers of new experimental data have been obtained.

2.1.6.1. Project Coronas-F

Russian satellite Coronas-F was launched 30 June 2001 on the orbit with height ~ 520 km and inclination of the orbit to the equatorial plane 83°. The devices measured the fluxes of neutral radiation during solar flares: X-rays and gamma radiation with the energy 0.03–200 MeV, neutrons with energy >20 MeV; fluxes of electrons with energy 0.3–108 MeV, protons with energy 1–90 MeV and nucleus with energy 2–40 MeV/nucleon were installed by SINP MSU.

Results of solar cosmic ray (SCR) study

Main results were obtained in the study of SCR penetration into the magnetosphere and processes of trapping of SCR protons with energy 1–15 MeV into the magnetospheric trap during magnetic storms.

SCR penetration into the magnetosphere

Figure 1 shows the example of the motion of penetration boundary (PB) of SCR into the magnetosphere during series of great magnetic storms in the October 2003. Thick line shows changes of Dst variation. It was shown that shard displacement to the Earth of PB could take place before Dst minimum under action of solar wind dynamic pressure impulse. The action of substorm activity on PB is detected. Considerable displacement of PB takes place during chain of substorms in the absence of magnetic storm (see Fig. 1).

Trapping of SCR protons

Coronas-F measurements during some strong magnetic storms 2001–2004 give the possibility to detect and carefully investigate the mechanism of trapping of solar protons with energies 1-15 MeV during storm recovery phase. For the first time the

effect of low energy protons PB doubling shown on Fig. 2 was detected 30–31 October 2004. The effect of injection by Sc impulse was detected in none of such events.

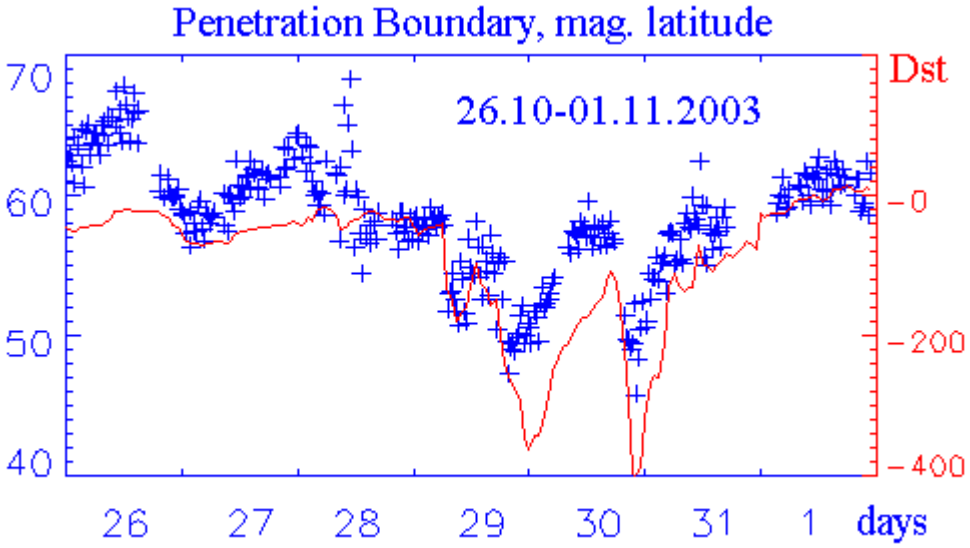

Figure 1: Dynamics of penetration boundary during substorms (26–27.10) and chain of magnetic storms 29-31.10.2003. Thick line is Dst index

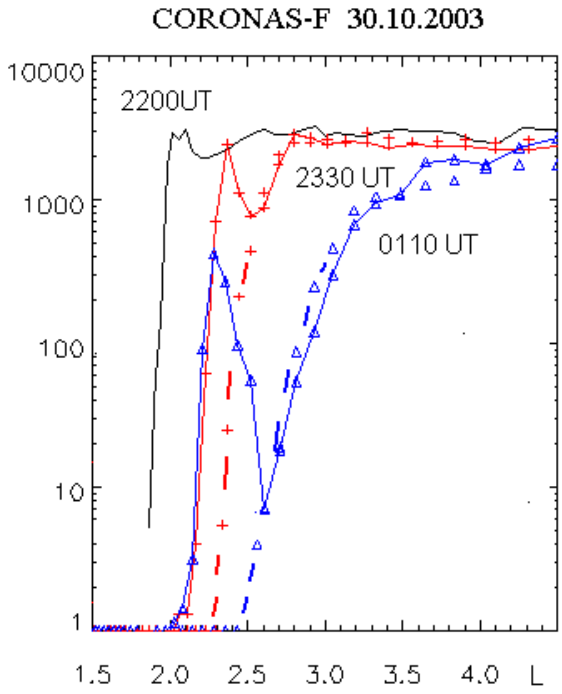

Figure 2: The effect of doubling of the penetration boundary in the channel 1–5 MeV (thick line) and single boundary in the channel 50–90 MeV: the outward displacement PB and trapping of 1–5 MeV protons at L = 2–2.5

Freshly trapped belt of solar protons was detected during crossing of Brazil anomaly (Fig. 3). Three such belts were formed during complicated disturbance 30 October – 4 November 2003.

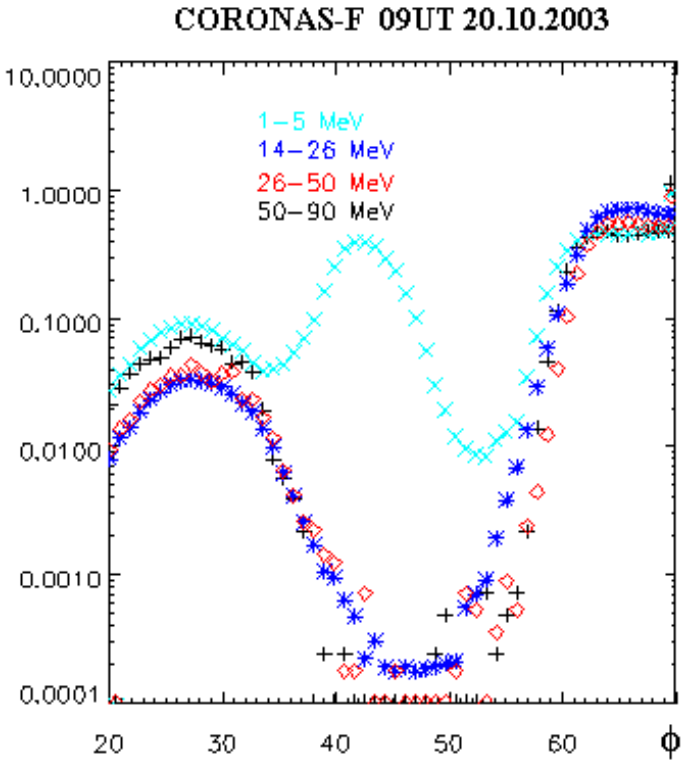

Figure 3: New solar proton radiation belt observed in the region of Brazil magnetic anomaly

Results of investigations of X-ray and gamma-ray emissions

The analysis of satellite "Coronas-F" data showed that the most energetic gamma quantum in solar flares with energies till 300 MeV are the result of neutral pion disintegration which borne in the solar atmosphere in the interaction of subrelativistic protons with the matter. The comparison of the time of high energy gamma quantum registration with the time of the beginning of the increases of solar cosmic rays on the Earth showed that proton acceleration can take place in compact region of solar flare.

The SONG instrument onboard CORONAS-F mission has observed X-ray and gamma-ray emission (see Fig. 8–10) with a high time resolution and with a sufficient energy resolution in the energy range 0.05–300 MeV in the powerful solar flares: namely 28.10, 04.11.2003 and 20.01 2005. The SONG data contribute unique information on the evolution of the flare electron and proton spectra. It is possible to show that in these flares:

(a) high-energy bremsstrahlung dominates and is lasting up to 30–100 MeV in the first acceleration episode;

(b) high-energy gamma-ray emission above 90 MeV in the later phases of the flare is undoubtedly produced by pion-decay. This emission marks a sharp appearance of the protons with energy >300 MeV that interact in the solar atmosphere;

(c) exact time of pion-decay radiation appearance was identified with accuracy ±2 s that provides in its turn the unambiguous time rule of accelerated particle appearance on the Sun. It makes possible to determine correctly time delay of GLE onset relative to the acceleration moment.

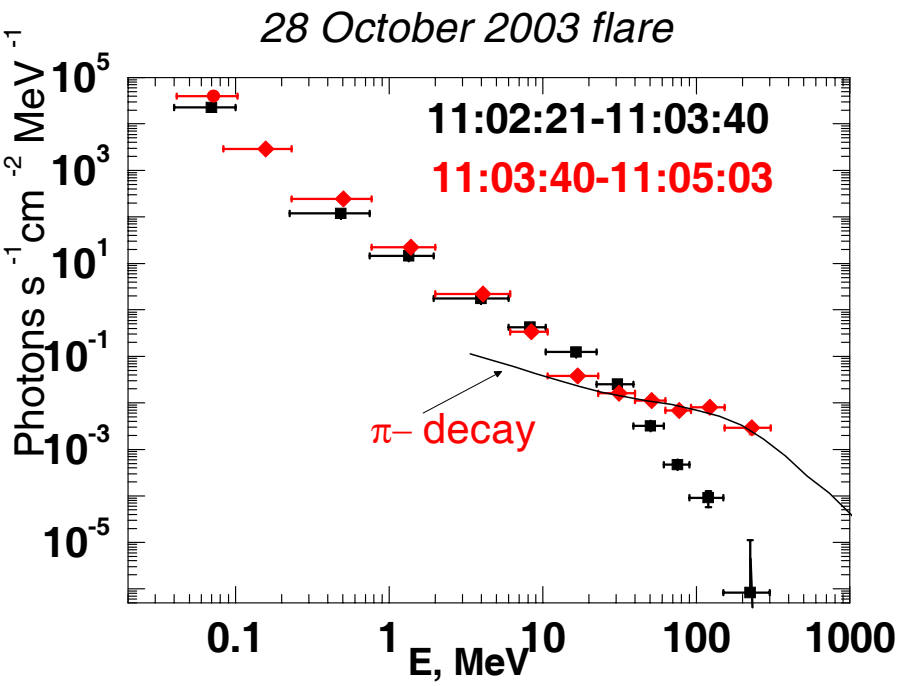

Figure 4: The gamma-ray spectrum dynamics measured by SONG. Black line shows the pion-decay gamma-ray spectrum used in our simulations

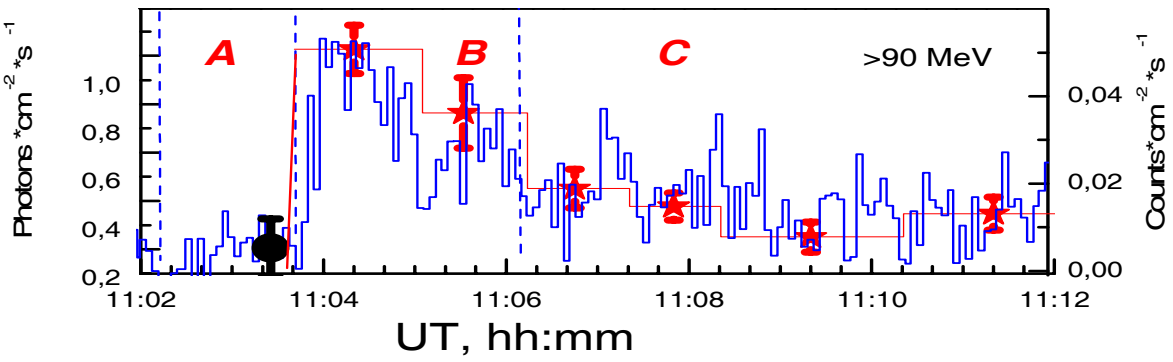

Figure 5: Time profiles of gamma-ray emissions of the 28 October 2003 flare. SONG count rate at energy >90 MeV (blue line, scale on the right) and calculated pion-decay gamma-ray flux (red line, scale on the left). Vertical dashed lines mark flare phases

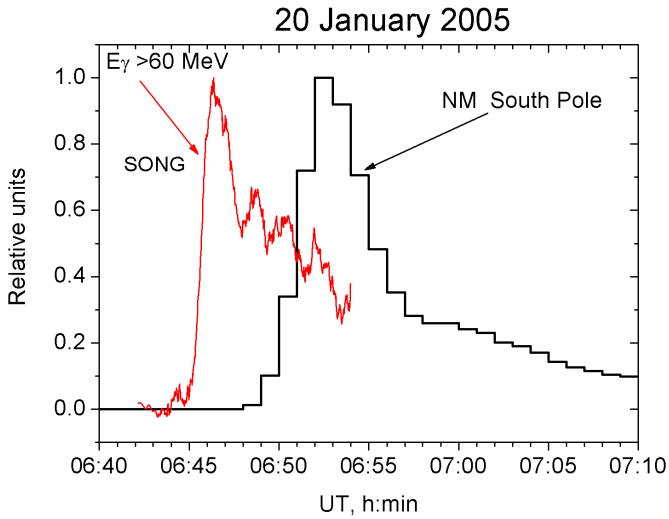

Figure 6: Time profile of gamma emission measured by SONG and time profile GLE, measured by South Pole Neutron Monitor.

2.1.6.2. Project "Tatiana"

Small satellite "University-Tatiana" launched to 250 anniversary of Moscow State University 20 January 2005 on the polar ring orbit with inclination 82° and height successfully worked. The satellite was equipped by scientific devices created in NPI MSU with the active participation of students and postgraduate students of the physical faculty of MSU. The great volume of experimental space physical information has been obtained. It became the basis for the creation of data base of space experiments in NPI.

In 2007 the "Universitetsky-Tatiana" satellite (the Tatiana satellite in short) data on near UV radiation (wavelengths 300-400 nm) from the atmosphere were processed and analyzed. In over globe analysis of the UV radiation intensity it was found that the maximal UV intensity was detected at high latitudes in the region of the aurora lights (intensity of the order of 10^9 photons/cm^2 s sr). The minimal intensity is measured near the geomagnetic equator: of about 3 10^7 photons/cm^2 s sr. At the same time on many Tatiana satellite circulations an intermediate intensity of the order of 10^8 photons/cm^2·s·sr was detected at latitudes 10–40° around the geomagnetic equator which forms 2 rather sporadic "belts".

The world map of the events having duration of 1-64 ms and an energy release in near UV in the atmosphere 10KJ-1MJ showed that they are concentrated near the equator (80 % of events at latitudes ±30°). They occurred with roughly equal probability over ocean and over continents. The Tatiana detector was able to operate not only at moonless nights but at full moon nights. Analysis of brightness (energy release) and rate of UV events detected in the Tatiana mission has shown that there is a correlation of UV transient event rate with lunar phase. There are 2 peaks of the event rate: at new moon and at full moon. The brightest events were detected at full moon nights.

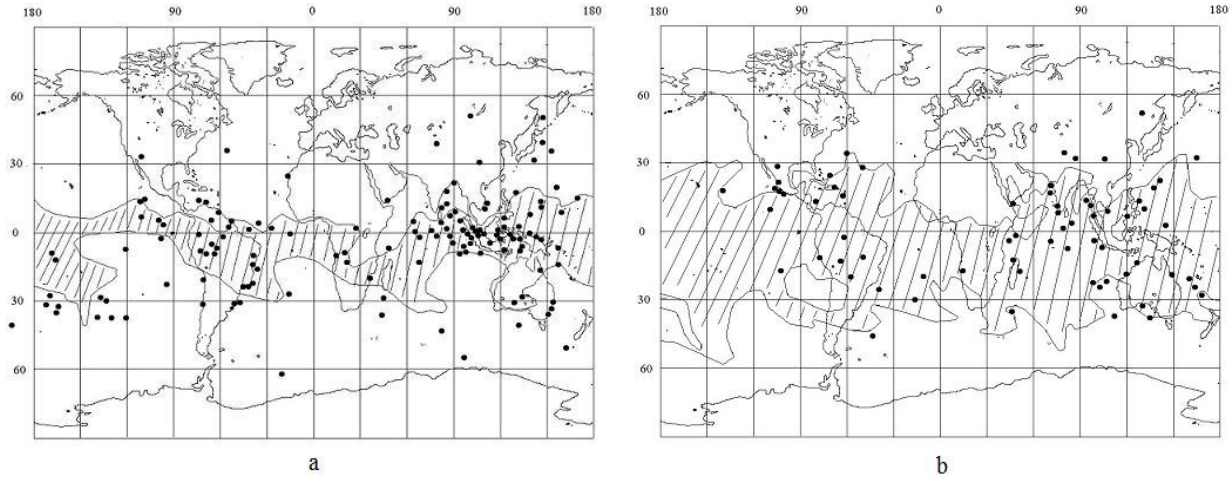

Figure 7: World map of UV events measured by the Tatiana detector. a-events at full moon nights (shaded is area with column water vapor density >5 g/cm^2), b- events at new moon nights (shaded is area with column water vapor density >3 g/cm^2).

2.1.6.3. Results of theoretical study and modeling processes on the Sun and in the magnetosphere of the Earth

Processes on the Sun

The modeling of "sell" MHD dynamo is conducted in the rotating spherical sell. Results are obtained for the cases thick and thin convective sell in the suggestion that convective sells may be the connecting chain between global and local solar MHD processes. The support of global magnetic field is observed in the first case. This field from time to time (however not regularly) has the inverse of polarity in addition with the formation of local in many cases bipolar magnetic configurations. It is ahown that local magnetic fields at such a case are deposited at definite not changeable latitude zones as large scale convective sells restore their positions. The process of local field generation in the second case have no such clear localization, inversion of whole field polarity does not take place.

The criterion is developed in accordance with which it is possible to select from observations cases of the action of two mechanisms of the formation of local magnetic fields in solar active regions — mechanism of flux tube emergence and convective mechanism. The comparison of the results of modeling with the data of experimental observations is conducted. Magnitograms of full vector of the field and doplerograms, obtained on the solar telescope and device SOHO MDI. The observed picture is compared with the conclusions of computer modeling of MHD convection. It is shown that obtained results are in better agreement with the convective mechanism of magnetic field formation in comparison with the idea of tube emergence. Investigations of the images of solar granulation give the possibility to conclude that the convective flows of roller type are present in subphotospheric regions of the Sun.

The series of computer calculations is conducted and solutions of the full system of equations of single fluid dissipative magnetic hydrodynamics taking into account Hall effect is obtained for natural matter. The structuring of rarified solar plasma in the process of evolution of axisymmetric plasma magnetic configuration is investigated. The magnetic field in the beginning of modeling was considered as localized in limited volume of infinite matter. Joint using of analytical and digital methods of study leads to the conclusion about existence in solar plasma specific magnetic structures consisted from two very thin magnetic tubes with inversely directed magnetic flux deposited clause to each other along all length.

In the investigation of solar corona theoretically and from the analysis of observations it is shown that coronal mass injections and solar flares can take place without visible changes of large scale magnetic field topology. Simple and clear scenario is developed giving the possibility to explain main observed features of eruptive events on the Sun observed in SOHO experiment and satellites TRACE and GOES-12. It is shown that global coronal mass injections includes injection of complicated systems of magnetic flux distributed on the large space scales which are larger than a number of active regions and comparable with half of solar disk.

New method of visualization of magnetic field in solar corona is developed. Coefficients of harmonic analysis in the potential approximation calculated on the results of field observations on the photosphere level are used as the input information. Three dimensional equations for the lines of field are digitally integrated. The results are presented as the project on picture plane. The method is comfortable for the using in studies and applied works on the investigation and prediction of “Space weather”.

New classification of corona mass injection in accordance with their velocity in comparison with phone plasma is created based on the methods of dimensionless analysis of sun and geliospheric processes. This classification more clearly shows different situations and types of flow with quick, middle and slow plasma velocities in the corona of the Sun.

Empirical formula showing the dependence V(S) averaged for the day velocity of solar wind V from the area of coronal holes on the visible side of the Sun as the Teilor ranks of the first and second order is obtained.

Processes in the magnetosphere of the Earth

Theoretical investigations of the dynamics of the processes in the magnetosphere of the Earth were conducted. Obtained results are compared with experimental data.

Some characteristics of low latitude boundary layer (LLBL) are determined using data of satellite observations. It is shown that the results of observations support the predictions of the developed theory, which explains of thick LLBL under northward IMF conditions and thin LLBL under southward IMF conditions.

The statistical analysis of the results of observations of field-aligned currents on satellite "Intercosmos-Bulgaria-1300" taking into account the finite width of observed current structures was conducted. The dependences of probabilities to observe current sheet with fixed width and current density from current sheet width are determined.

The model of auroral particle acceleration by double layers is developed taking into account the process of distribution function modifications. It is taken into account that measured distribution functions are approximated by kappa-distributions in most cases.

Theory of plasma transport during magnetic storms is developed. The processes leading the intense filling of magnetic flux tubes by ions of ionospheric origin are selected. This process can be considered as one of the main process of storm dynamics.

Characteristic features of magnetospheric turbulence including analysis of data of satellite observations and riometric absorptions in the south polar cap study showed that the maximal level of turbulence is observed in the region 20-24 h of magnetic local time where as a rule the "substorm eye" is localized – the region of the formation of auroral bulge during substorm expansion phase. A number of experimental supports of developed earlier model of substorm expansion phase onset on quasidipole magnetic field lines and auroral arc brightening during substorm expansion phase is obtained. The mechanism explaining the stretching of magnetic field lines before the beginning of substorm expansion phase is suggested. It is shown that the factor determining nearest to the equator auroral arc brightening during magnetospheric substorm is the formation of field-aligned particle beams on the boundary of the nearest to the equator inverted V structure.

Complicated dynamical processes in the geomagnetic tail involving cycles of electromagnetic energy loading-unloading, fast breakdowns of equilibrium, embedded thin current sheets (CS), medium-scale turbulent plasma motions, and intense magnetic field variations, are considered from a unified point of view. As the most significant appear the nonlinear dynamical processes of thin kinetic CS formation.

Studies carried out with the use of numerical particle simulation (see Fig. 18), have shown that the nonlinear current structures which appear spontaneously, are quasi-stastionary, and they may be of two different kinds, depending on conditions in the plasma sheet. At certain conditions, they are the nonlinear equilibrium CS with anisotropic ions. At other conditions they are a pair of collisionless slow shocks. In both cases, fast conversion of electromagnetic energy into energy of rapid plasma flows takes place. The latter, in their turn, may be energy sources for the two-dimensional MHD turbulence in the plasma sheet. While the spontaneously arising thin current structures are quasi-stastionary, however at large spatial scales the disturbance involving them, also involves a fast MHD wave constituent. The latter may provide new equilibrium breakdowns in some new zones in the plasma sheet; those breakdowns are followed again with a relaxation process involving formation

of embedded thin CS and fast ion flows. The resulting intermittency is a real characteristic feature of turbulent disturbances observed in the plasma sheet.

Observations carried out in the geomagnetic tail reveal also a wide variety of thin embedded current structures. In the kinetic theory with the use of numeric simulation, a detailed study has been fulfilled of various versions of equilibrium CS. For the geomagnetic tail it is shown that as compared to the CS in the hydrogen plasma, the presence of oxygen ions can expand the thickness of boundaries of thin CS. Equilibrium solutions with a pair of current density peaks have been obtained. In such bifurcated CS the phase density domain of quasi-trapped ions increases at the expense of ions on transient orbits being the current carriers; this may produce the decay of CS. The electron component has been taken in consideration, and it is shown that a very narrow electron current peak appears at the centre of CS. The constructed theory reflects the hierarchy of plasma structures and processes in the magnetosphere where the micro-, meso-, and macro-scales are closely interrelated.

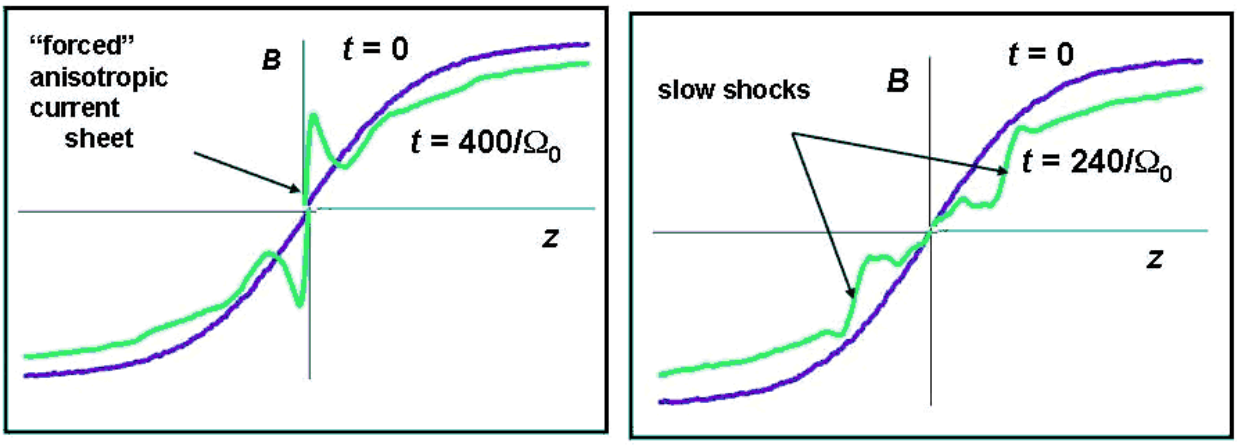

Figure 18: Formation of thin embedded current sheet.

Topological structure of the magnetosphere for northward IMF was studied in a framework of the paraboloid model. For the forced solar wind conditions, the location of the polar cap region, the polar cap potential drop, and the field-aligned acceleration potentials depending on the solar wind pressure and IMF By and Bx changes was investigated. Open field line bundles, which connect the Earth's polar ionosphere with the interplanetary space, are calculated. It is shown that specific curling of the open field line bundle which takes place near the cusp region leads to the vortex convection feature in the polar ionosphere. It is found that the moving of magnetic null points inside the magnetosphere for northward IMF leads to an additional attenuation of the solar wind electric field penetrated inside the magnetosphere.

The partial ring current field model have been created. It incorporated the field-aligned currents, and the eastward electrojet ionospheric closure currents.

Constructed partial ring current model gives the possibility to calculate its magnetic field on the Earth's surface. Relative ring current and tail current contributions to *Dst* were investigated on the basis of the statistical study of 70 magnetic storms of different intensities. Special attention was paid to the extremely disturbed conditions during magnetic storms in October – November 2003. Variations of the magnetic field produced by magnetospheric currents on the Earth's surface were calculated using paraboloid model of the magnetosphere A2000, taking into account the effect of terrestrial induced currents. Analysis of *Dst* sources shows saturation of the tail current effect under extremely disturbed conditions. The ring current becomes the dominant *Dst* source during severe magnetic storms, but during moderate storms its contribution to *Dst* is comparable with tail current's contribution. The ring current injection amplitude increases with the growth of magnetospheric disturbance level. Asymmetrical ring current effect was studied during magnetic storm on 20–22 November 2003. It was obtained that total partial ring current is about 6 MA during storm maximum. Its contribution to *Dst* on the storm main phase is about — 70 nT, while the symmetrical ring current effect is about — 200 nT. The partial ring current demonstrates fast development and sharp decay up to pre-storm level on the time-scale about of 10 hours.

Averaged spectra of proton and electron fluxes at $L < 1.2$ and electron fluxes at $1.2 < L < 1.9$ in the magnetosphere of the Earth are obtained. It is shown that the break in spectrum of electrons at $L < 2$ exists near energy ~1 MeV.

Computer model of space satellite electrization is developed in the hot magnetospheric plasma. The model is developed for engineering calculations on the stages of the development of the project, its designing and exploitation. It is possible to change in the interactive regime of conditions of satellite functioning, changes of its geometry and electro physical properties of construction materials.

2.1.6.4. Creation of Internet portal, database and the book "Model of Space"

The Internet portal http://smdc.sinp.msu.ru is created. It includes database of charge particle measurements, visualization programs and programs for the analysis of geomagnetic conditions in the magnetosphere and radiation conditions in the near Earth Space. Database in Oracle includes the results of charged particle measurements on orbits of satellites "University-Tatiana", "Coronas-F" and "Meteor-3M" and also data of space experiments of 90th. Database jointly with applied versions of space models developed in SINP MSU form the united system of space monitoring for storage, processing and scientific analysis and visualization of space data.

The interactive pocket of programs (IPP) COSRAD and WEB-interface are created (http://cosrad.sinp.msu.ru) which can be used for forecasting radiation conditions, absorption and equivalent doze and frequency of single failure in microschemes which are waited on satellite during long period flights (more than 1 year). All calculations are produced taking into account the width of the defense on space device for fluxes of electrons and protons of radiation belts of the Earth, protons

and nucleus of chemical elements (from helium till uranium), galactic cosmic rays/ protons and ions (from helium till nickel) of solar cosmic rays.

Summations of results of investigations of SINP MSU in the region of Space investigation and properties of materials in Space during lust 20 years and conducted analysis of achievements of Russian and foreign scientists in this region it is prepared and edited the book “Models of Space”. Two-volume book is developed for workers in Space institutes, students and post graduate students of corresponding specialties.

2.1.7. IOFFE PHYSICAL-TECHNICAL INSTITUTE OF THE RUSSIAN ACADEMY OF SCIENCES

2.1.7.1. Evidence for Existence of Multiply Charged Argon Ions in Anomalous Cosmic Rays

The spectrum of Ar ions in anomalous cosmic rays in the energy range 14–42 MeV/nucleon was measured in the PLATAN-5 experiment at the Mir space station in 1994–1997. The spectrum is analyzed along with the data obtained by the SIS instrument on the ACE spacecraft in the near-Earth space. On the basis of the comparison of the spectra recorded within and beyond the magnetosphere, the average effective charge of ACR argon ions has been estimated. The estimate obtained is much larger than unity at energies exceeding 22 MeV/nucleon. The ion charge gradually increases with an increase in energy and reaches the value $Q = 4$ at an energy of 38 MeV/nucleon.

Introduction

Anomalous cosmic rays (ACR), primarily the classical He, O, Ne, and Ar ions with a high first ionization potential (≥13.5 eV) attract much interest because they contain diverse information about the processes of acceleration and propagation of particles in the heliosphere. It is assumed that acceleration occurs mainly in the boundary shock wave at the heliospheric boundary. However, the existing experimental data are insufficient to substantiate a relatively complete theoretical model of the ACR phenomenon. There are a large number of theoretical investigations and assumptions in constructing models. However, they all meet a number of difficulties. The assumption about ion acceleration at the boundary shock wave has not been experimentally confirmed. The Voyager-1 spacecraft fixed the transmission of the heliospheric boundary in December 2004 at a distance of 94 au. However, the expected increase in the energy and intensity of ACR ions was not observed at the point of heliospheric boundary crossing at the heliolatitude 34° N, except for the conventional modulation due to the decrease in the solar activity influence at the transition from a maximum to minimum of solar activity. A similar modulation was also detected by the Voyager-2 spacecraft, which was inside the heliosphere in 2004.

ACR argon ions have been least investigated due to their small abundance. At energies of 10–20 MeV/nucleon, the intensity of argon ions is several hundred times lower than that of oxygen ions. It is important to clarify how strongly the differences between O and Ar ions in mass and rigidity can affect the characteristics of ion transport in the heliosphere and acceleration at its boundary. Both captured and interplanetary argon ions with energies of 1–4 MeV/nucleon were detected with the MAST instrument on the SAMPEX spacecraft. In this case, the ratio of the numbers of captured and interplanetary ions was found to be about 200 (larger than that for anomalous oxygen ions by a factor of 2). No captured

argon ions with energies >16 MeV/nucleon were detected in the experiment. Beyond the magnetosphere, the spectrum of interplanetary ACR argon ions in the energy range 3.5–20 MeV/nucleon was measured at the WIND spacecraft; the spectrum in the range 10–40 MeV/nucleon was measured with the SIS instrument on the ACE spacecraft at a distance of $1.5 \cdot 10^6$ km from the Earth. At energies higher than 40 MeV/nucleon, a dip arises in the spectrum, with subsequent increase in the flux due to the contribution of galactic cosmic ray (GCR) argon nuclei.

The data on multiply charged component of ACR ions with energies >20 MeV/nucleon are important. Oxygen ions with a charge $Q > 1$ in ACR have been revealed for the first time with the MAST and HILT instruments on the SAMPEX spacecraft. It was suggested that other ACR ions may also have a multiply charged component.

The purpose of this study was to measure the energy spectrum of ACR argon ions in the Earth's magnetosphere and determine the degree of ionization of anomalous argon through comparison with the spectrum beyond the magnetosphere, using the ion transmission functions for the orbit of the Mir space station (see Fig. 1).

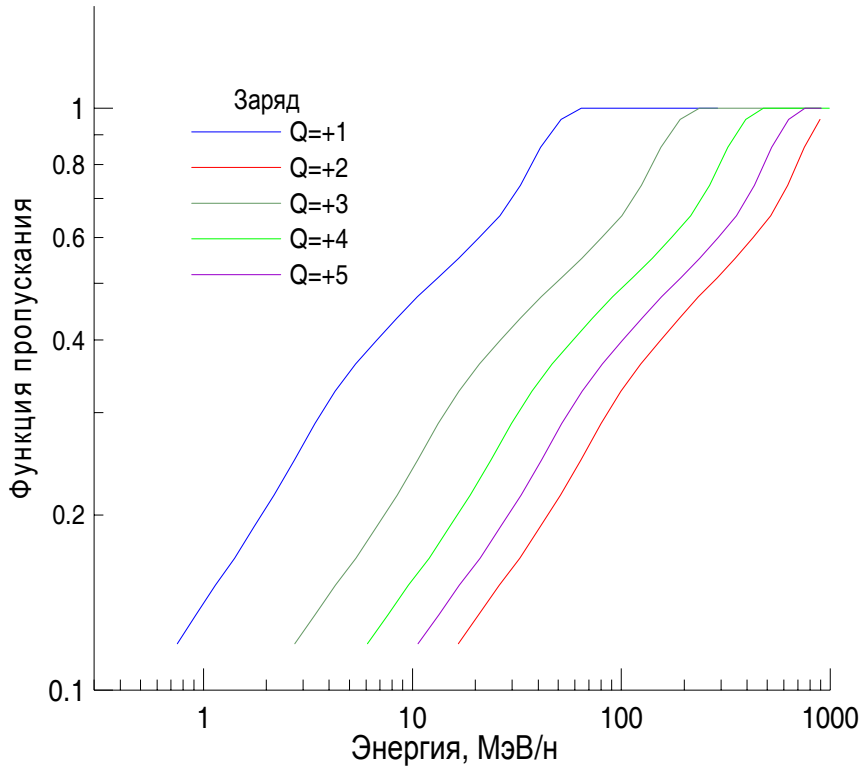

Figure 1: Penetration of charged particles on orbit of the Mir station: transmission function for Ar ions with different charges

Method

The PLATAN-5 chamber (PLATAN is an abbreviation of «plastic track analyzer») was exposed on the external surface of the "Kvant-2" module of the Mir space

station at the orbit with an inclination of 51.6° and an altitude of 350–400 km in the period from September 11, 1994 to November, 1 1997. The chamber with a geometric factor of 5200 cm^2 sr consisted of 32 layers of solid state track detector (polyethyleneterephthalate) with a thickness of 180 μm. The detector layers were subjected to special processing. Measurements were performed in one of eight identical units composing the PLATAN-5 chamber for the tracks stopping in the second–sixth layers (counted from the chamber top). The nuclear charge was identified by the method of LR diagrams.

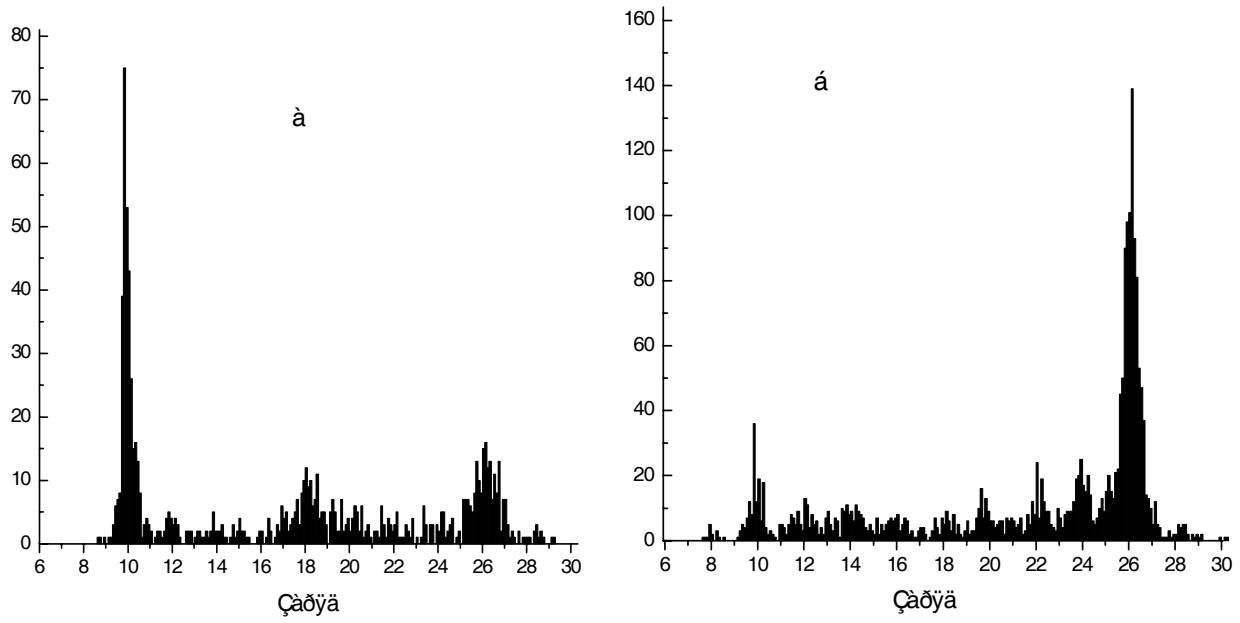

Figure 2: Charge distribution of particles in the (a) PLATAN-5 and (b) PLATAN-4 chambers.

Figure 2a shows the charge distribution of the nuclei stopped in the second and third layers in the PLATAN-5 chamber. This distribution contains peaks of ACR neon and argon ions. The argon peak is comparable in amplitude with the peak of GCR iron nuclei. The spectrum of GCR nuclei, measured over the entire depth of the PLATAN-4 chamber, which was exposed during 10 months on the Mir space station from September 11, 1994 to July 23, 1995, is shown in Fig. 2b for comparison. In this distribution, the contribution of anomalous argon is negligible (no larger than four or five particles) as a result of shorter exposure and smaller searched area of the detector in the PLATAN-4 chamber. This is confirmed by direct measurements in the upper layers of the PLATAN-4 chamber. The charge spectra in Figs. 2a and 2b incompletely reflect the relative abundance of individual elements because these spectra do not take into account the geometric corrections, which increase with a decrease in the particle charge. However, they indicate a sufficiently high charge resolution for selection of the anomalous component of argon and neon ions.

Results and discussion

Figure 3 shows the following data: a) the spectrum of ACR argon ions in the energy range 3–20 MeV/nucleon in the interplanetary space, measured with the LEMT instrument in the EPACT experiment on the WIND spacecraft in quiet days from November 1994 to November 1998; b) the total spectrum of ACR Ar and GCR Ar, measured in the interplanetary space with the SIS instrument on the ACE spacecraft from September 1997 to March 1998 in the energy range 10–120 MeV/nucleon; and c) the spectrum of ACR Ar measured in the magnetosphere at the Mir space station (this study) in the energy range 14–42 MeV/nucleon.

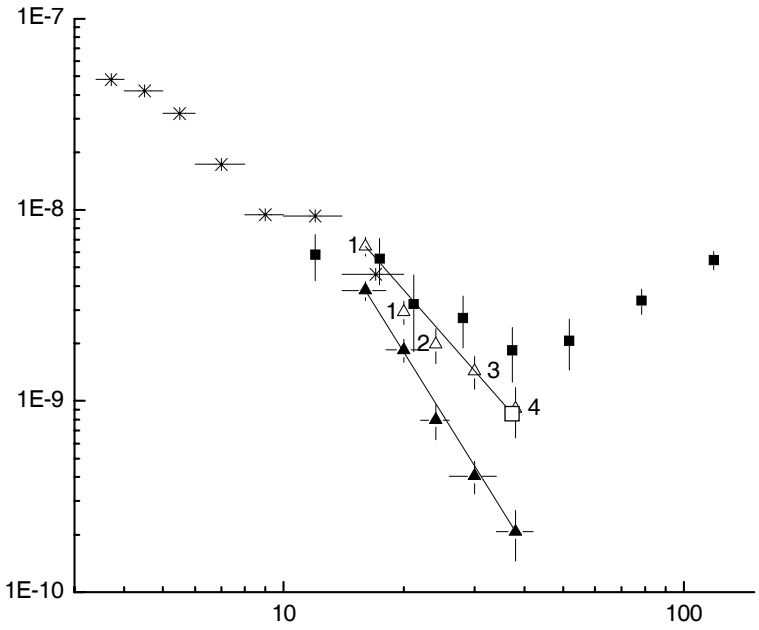

Figure 3: Energy spectra of argon ions measured in the minimum of solar activity beyond the Earth's magnetosphere at the (*) WIND (LEMT instrument) and (■) ACE (SIS instrument) spacecrafts and (▲) in the Earth's magnetosphere at the orbit of the Mir space station (PLATAN-5); (Δ) the intensity of ACR argon ions recalculated from the orbit of the Mir space station to the Earth's orbit at the noted values of the average effective charge; () the intensity of ACR argon ions (ACE) after subtraction of the contribution of GCR argon; and (straight lines) the spectra of ACR argon within and beyond the Earth's magnetosphere.

Note that the statistical errors in the magnetospheric measurements are smaller by a factor of 2–3 than in the measurements with the SIS instrument on ACE. We believe that the spectrum in the magnetosphere has a power form (filled triangles in Fig. 3). We estimated the contribution of ACR argon ions at energy of 37 MeV/nucleon (open squares in Fig. 3). To this end, the contribution of galactic argon beyond the magnetosphere was subtracted from the Ar spectrum and the value obtained was increased by 16 % (taking into account that the ACE measurements were performed in the declining phase of ACR intensity, by analogy

with the data on the intensity of ACR oxygen ions). Furthermore, we estimated the intensity of anomalous argon beyond the magnetosphere at an energy of 16 MeV/nucleon, using the transmission functions for argon ions with different degrees of ionization (for $Q = 1$ in the case under consideration). The value obtained (open triangle in Fig. 3) is in good agreement with the results of the WIND and ACE measurements. Approximation of the energy spectrum of ACR argon ions by a power function with the exponent $\gamma \approx 2.4$ is consistent with the similar shape of the spectrum of ACR oxygen ions ($\gamma = 2.12–2.62$) in the energy range 15–50 MeV/nucleon. As a result, we obtain the estimate of the shape of the spectrum of ACR argon ions in the interplanetary space. Upon transition from the spectrum in the magnetosphere to the spectrum beyond it, a gradual increase in the average effective charge of argon ions manifests itself with an increase in energy: $Q > 1$ (20 MeV/nucleon), $Q > 2$ (24 MeV/nucleon), $Q = 3$ (30 MeV/nucleon), and $Q = 4$ (38 MeV/nucleon). Note that for ACR oxygen and neon ions the increase in the average effective charge Q in the energy range 15–25 MeV/nucleon is smaller (from 1 to 2). Note also that the degree of ACR argon ionization cannot be determined with the use of the spacecrafts of the last generation that are in current use.

Two characteristics related to the change in the radial gradient of the ACR intensity are noteworthy.

First, the radial gradient for ACR argon ions, derived from the measurements with the Voyager-1, Voyager-2, and Pioneer spacecrafts and the SIS spacecraft, decreases by a factor of about 2 (from 3.3–4 to ~2) with an increase in energy from 10 to 20 MeV/nucleon.

Second, the above-mentioned radial gradient for ACR argon ions is much smaller than that for ACR oxygen ions (~6.5) at energies in the range 7–17 MeV/nucleon.

The noted features may reflect the increase in the degree of ACR ionization with an increase in energy and the difference in the rigidities of ACR oxygen and argon ions.

Conclusions

1. The energy spectrum of ACR argon ions in the Earth°s magnetosphere has been measured for the first time in the energy range 14–42 MeV/nucleon.
2. The shape of the spectrum of ACR argon ions in the interplanetary space in the above-mentioned energy range has been estimated.
3. It is established that the effective average charge of ACR ions increases with an increase in mass and energy. For argon ions, the charge reaches the value $Q = 4$ at an energy of 38 MeV/nucleon.

2.1.8. MOSCOW ENGINEERING PHYSICS INSTITUTE (STATE UNIVERSITY). ASTROPHYSICS INSTITUTE

2.1.8.1. The results of AVS-F apparatus database treatment in experiment CORONAS-F

The AVS-F (Amplitude-Time Sun spectrometry) apparatus [1, 2] was intended to study characteristics of fluxes of hard X-rays and gamma-rays from solar flares and to detect other non-stationary fluxes of cosmic γ-rays. The experiment was conducted within framework of the CORONAS (Complex ORbiting ObservatioNs of the Active Sun) international project onboard the special-purpose automatic station "CORONAS-F" during time period from 31.07.2001 to 06.12.2005.

This apparatus constitutes the system of electronic for onboard data acquisition from two detectors: SONG-D [3] (CsI(Tl) detector Ø200 mm and 100 mm height, fully surrounded by plastic anticoincidence shield) for gamma-ray analysis in two energy bands 0.1–10 MeV (low energy band) and 2–80 MeV (high energy band) and XSS-1 [4, 5] (CdTe detector 4.9×4.9 mm) for X-ray analysis in 3–30 keV energy range. The detector threshold and amplification coefficient were changed approximately on 1 percent per month [6, 7]. The energy resolution of the system was ~13.0 % for gamma-quanta from ^{137}Cs with energy 0.662 MeV [6, 7]. The function diagram of AVS-F apparatus is shown at Fig. 1.

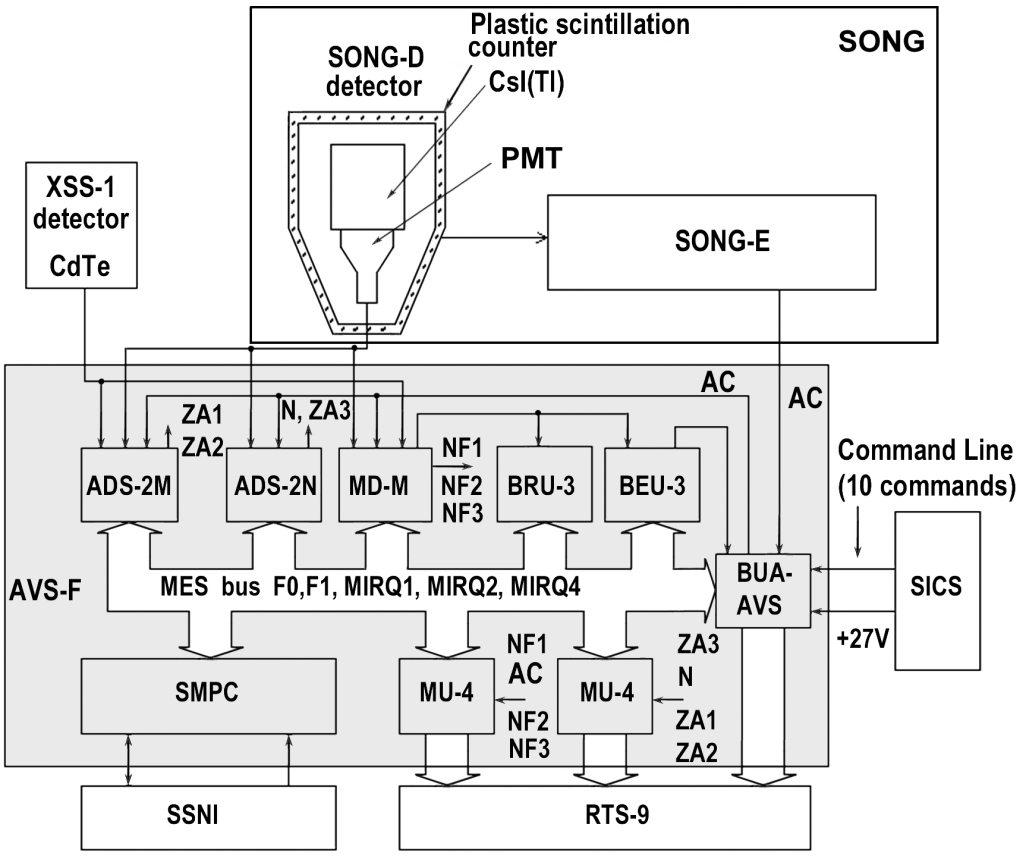

Figure 1: The function diagram of AVS-F apparatus

Solar flares characteristics by AVS-F data

Over 100 solar flares were found during data processing. The catalogues of solar flares registered in low [8-10] and high energy bands [11] of AVS-F apparatus were compiled (now about 40% of whole amount of data was processed).

On Fig. 2 the examples of solar flares time profiles registered by AVS-F are presented. Most part of solar flares shows gamma-ray emission during rise time of soft X-ray emission by GOES satellites series data and duration of it is smaller than soft X-ray one (Fig. 1*a*, *b*) [8, 9, 12-15]. Some solar flares demonstrate gamma-ray emission only during the maximum of X-ray emission and some flares has identical time duration in soft X-ray and gamma-ray bands [8, 16-18]. In 10 % of flares gamma-emission with energy over ~17 MeV was observed by preliminary data analysis [12, 19]. In 8 flares the duration of gamma-ray registration in both AVS-F energy bands practically coincide [11, 15–17].

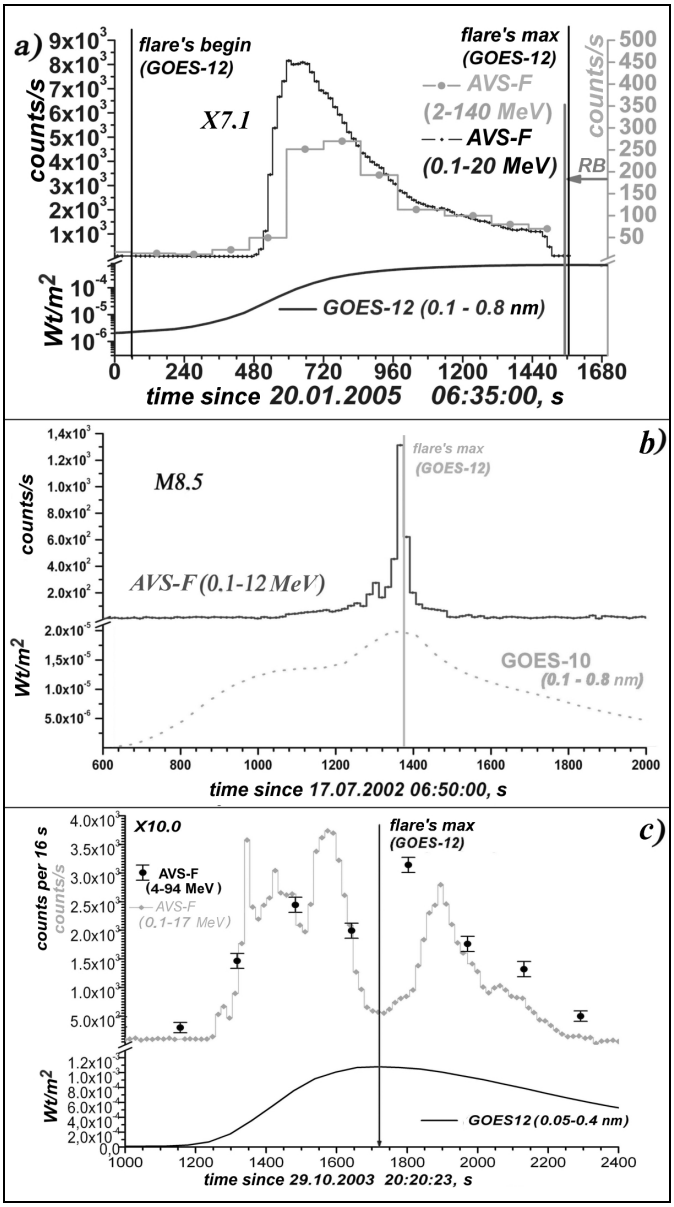

Figure 2: Solar flares temporal profiles examples by AVS-F data

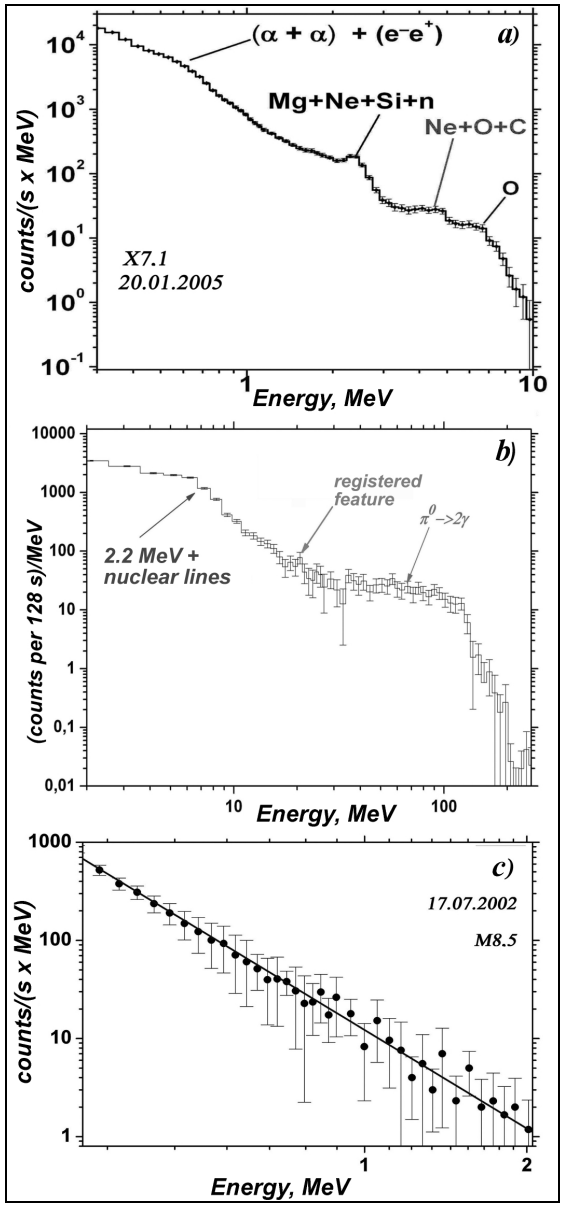

Figure 3: Solar flares energy spectra by AVS-F data

Certain complexes of gamma-lines were observed in solar flares energy spectra in low energy gamma-band of AVS-F apparatus. These complexes correspond to αα-line, annihilation line, nuclear lines and neutron capture line (Fig. 3*a* and 5*a*) [9, 12, 16, 17]. In high energy gamma-band there is a wide peculiarities around 2–7 MeV region, corresponding to combinations of nuclear lines and neutron capture line and one corresponding to gamma-rays from neutral pions decay (Fig. 3b) [17, 22, 23].

Unidentified spectral feature in the region of 15–21 MeV was first observed in spectrum of 20.01.2005 solar flare in time interval 06:44:52–06:51:16 UT [19]. The confidence level of this feature separation in summarized spectrum is 2.5σ (Fig. 3b), but in the flare maximum (06:47:00–06.49.08) it separated at 3σ one [18, 19].

Some solar flares without any lines in energy spectra (e-dominated flares) were also observed (see Fig. 3*c* and 4*b*) [8, 14, 20, 21]. This feature may be connected with 15.1 MeV line ($^{12}C+^{16}O$) or probably with radiative neutron capture on ^{3}He (20.58 MeV) or their combination [18, 19].

There is not any strong correlation between presence or absence of high energy gamma-ray and the intensity of soft X-ray emission during solar flares but in some cases there is gamma emission during very week solar flares (class B and C) [20, 21].

As an example of such event the solar flare 12.01.05 (class B4.6) is presented on Fig. 4. The highest value of gamma-ray energy during this flare was $E_{max} = 7.0 \pm 0.3$ MeV.

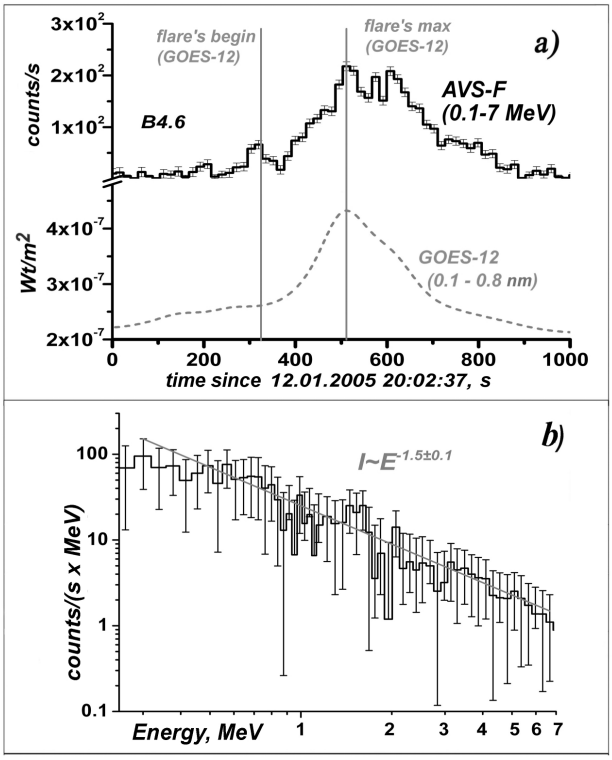

Figure 4: Temporal profile (*a*) and energy spectrum (*b*) of faint solar flare January 12, 2005.

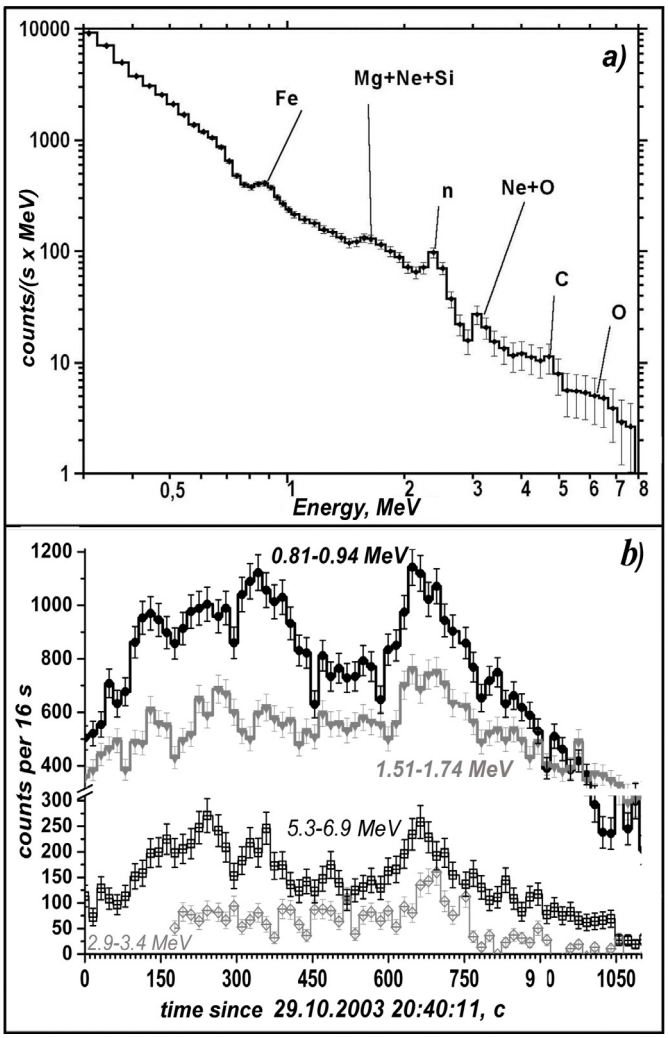

Figure 5: Energy spectrum of 29.10.2003 solar flare in low energy gamma-band of AVS-F apparatus (*a*) and this flare temporal profiles in some energy bands corresponding to lines separated in energy spectrum (*b*).

There are not any lines in energy spectrum of this flare but there is a fine structure on its temporal profile with time scale ~90 sec (following the results of preliminary analysis of periodogram) [20]. Now the compilation of the catalogue of such faint events is continued.

During some events, periodogram analysis shows fine structure having time regularities in low energy gamma band of AVS-F apparatus with time scale of 30-120 sec and the same for energy windows corresponding to gamma lines presented in these flares (Fig. 5*b*) [15, 22, 23] on 99 % confidence level [13, 21]. In some cases time profiles in different energy windows are significant shifted and summed time profile (in wide energy window) haven't got any fine structure at all [22].

The AVS-F apparatus performs time profile analysis during first 4.096 sec of flares trigger with 1 msec resolution. We have analyzed such temporal profiles for 7 solar flares (17.07.2002 (class M8.5), 04.04.2002 (class M6.1), 26.10.2003 (class M7.6), 29.10.2003 (class X10.0), first episode of solar flare 04.11.2003 (class 18.0) gamma-emission, 12.09.2004 (class M3.2) and 20.01.2005 (class X7.1)). This

analysis shows the time regularities with scale from 7 to 35 msec in 0.1–20 MeV energy band for only one flare of 20.01.2005 on 99 % confidence level, but for other 6 flares time regularities with scale 3-100 ms are absent on temporal profiles with 1 ms time resolution in the low-energy gamma-ray band of AVS-F apparatus on 99% confidence level (Fig. 6) [23].

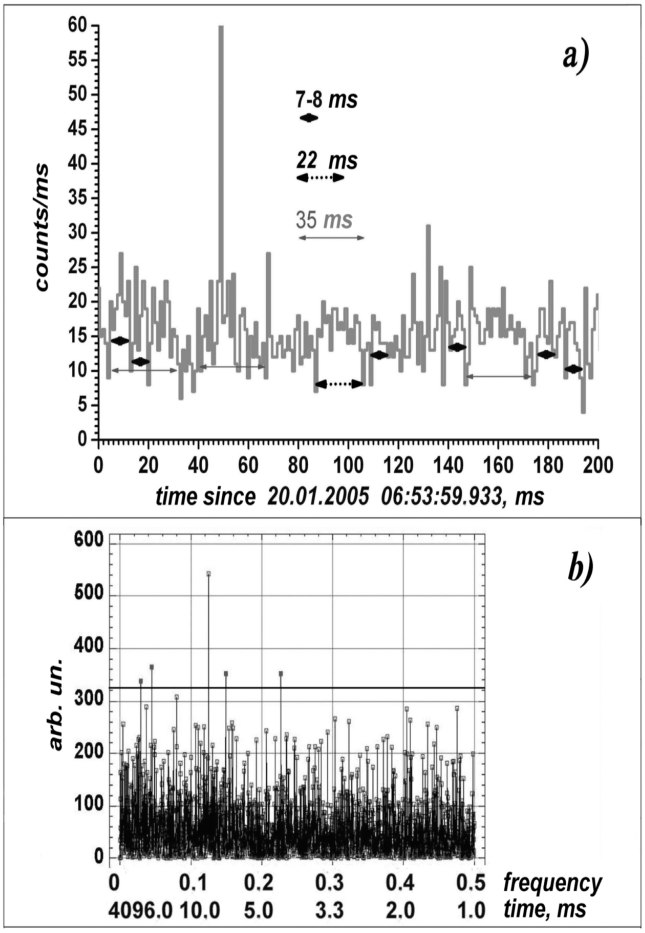

Figure 6: Fragment with thin structure (*a*) and periodogram (*b*) of January 20 solar flare temporal profile with 1 ms time resolution in energy band 0.1–20 MeV.

The characteristics of gamma-ray bursts by AVS-F data

More than 30 Gamma-ray bursts (GRB) were registered during AVS-F apparatus period of operation in low energy gamma band [24, 25]. All observed GRB have duration more than 2 s, because of the minimum integration time for spectroscopy information from AVS-F apparatus was 1 s. Comparative characteristics of AVS-F apparatus and another GRB detectors in Table 1 are presented [25]. Most part of GRB registered in low energy band of AVS-F apparatus were confirmed by data of HETE, RHESSI and SWIFT/BAT (see. Fig 7*a*, *c*).

For some GRB AVS-F observed γ-emission in high energy band within RHESSI, HETE and SWIFT t_{90} intervals. Maximum energy of gamma-emission was detected by AVS-F apparatus during GRB050525 $E_{max} = 147 \pm 3$ МэВ (Fig. 7*b*) [24]. In this period there were not any other detectors with opportunity of so high energy registration.

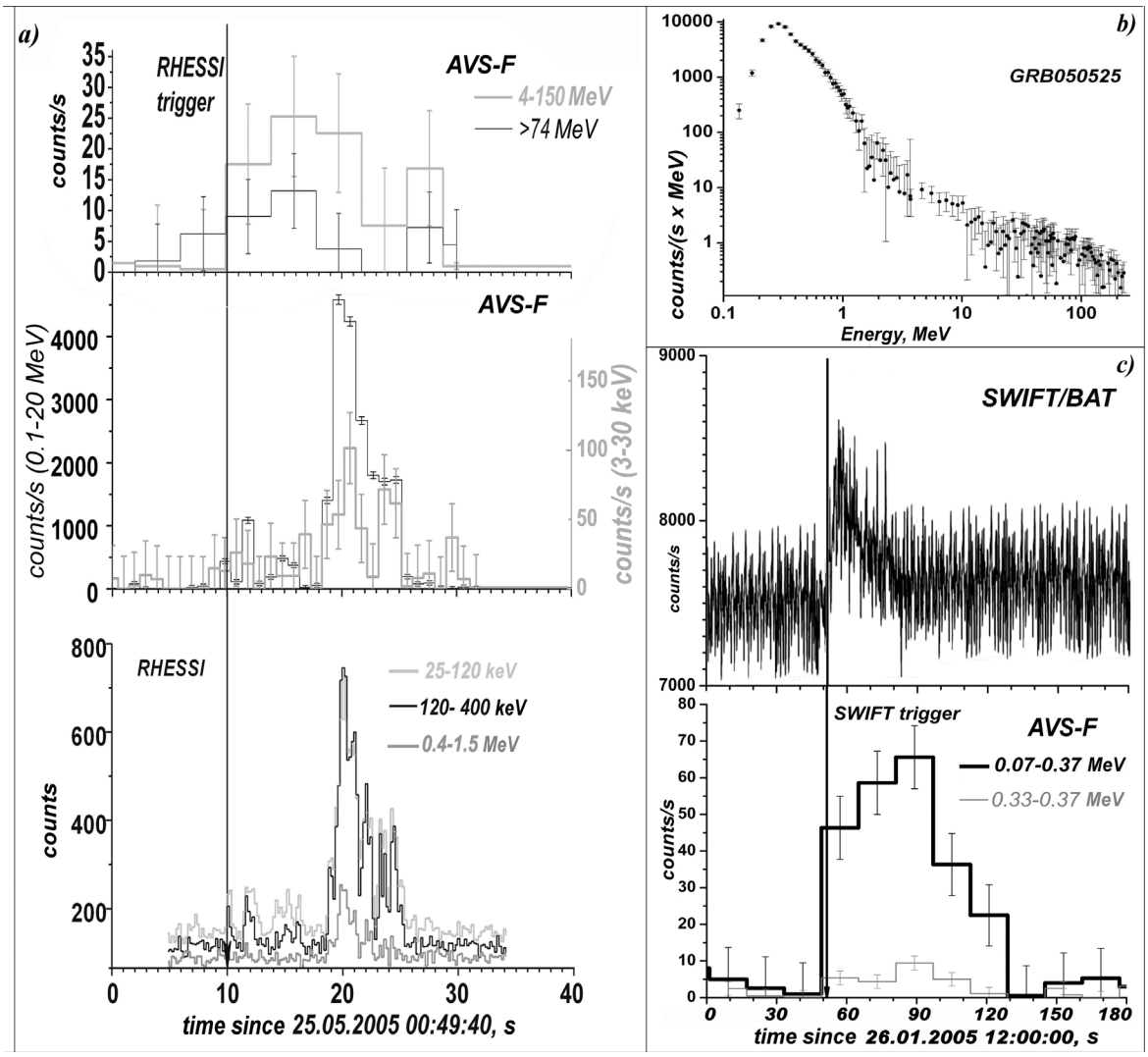

Figure 7: Temporal profile of GRB050525 by AVS-F and RHESSI data (*a*), GRB050525 energy spectrum by AVS-F data (*b*) and temporal profile of GRB050126 by data of AVS-F and SWIFT (*c*)

Table 1. Comparative characteristics of AVS-F apparatus and other GRB detectors

Characteristics	***Detectors***			
	***AVS-F* (*gamma-bands*)**	***RHESSI***	***Swift/BAT***	***GGS Wind/Konus***
Active area	~ 600 cm^2	~ 300 cm^2	5200 cm^2	200 cm^2
Field of view	~ 2π sr	2π sr	2 sr	4π sr
Type of detector	CsI(Tl)	Ge	CdZnTe	NaI
Energy band	0.05–11 MeV 4–94 MeV (2001 year data) 0.08–22 MeV 2–260 MeV (2005 year data)	0.05–17 MeV	15–150 keV	0.01–10MeV
Energy resolution (FWHM)	86 keV (13 %) at 662 keV	<3 keV at 100 keV <5 keV at 500 keV	3.3 keV at 60 keV 100 keV at 660 keV	100 keV at 660 keV

The analysis of quasistationary equatorial precipitations by AVS-F data

Count rate exceeding on 15–30 % relatively to polynomial approximation in low-energy AVS-F gamma band were found at some equatorial parts of orbits in latitude range –25⋯+30° [7, 26]. This effect was named quasistationary equatorial precipitations. More than 700 (68 %) of registered events were identified as precipitations during processing of ~40 % of telemetry sessions.

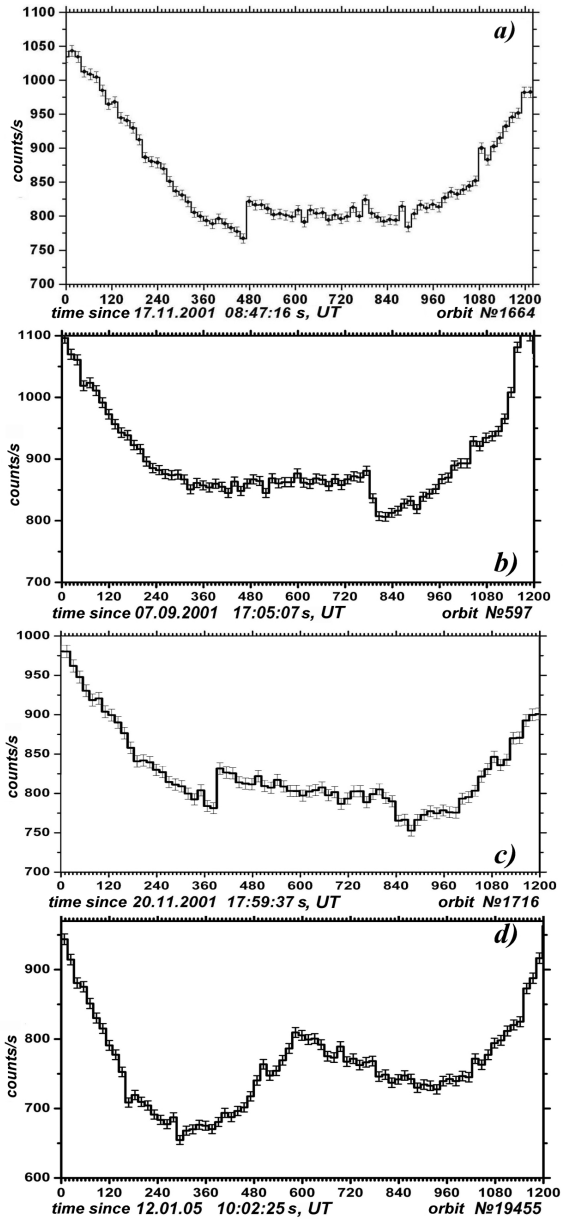

Figure 8: The typical temporal (latitude) profiles of precipitations on AVS-F data: *a* — type I; *b* — type II; *c* — type III; *d* — type IV

Four main types of quasistationary precipitations were separated [27–30] (Fig. 8). The shape of 44 % precipitations temporal (latitude) profiles (I type) has a fast rise of count rate on the South direction and flat decay on the North direction from geomagnetic equator. The shape of 21 % ones has a fast rise of count rate on the North direction and flat decay on the South direction from geomagnetic equator

(II type), 4 % ones (III type) are practically symmetrical with sharp boundaries and shape of 4 % ones (IV type) has intence maximum and symmetrical shape too. The linear dependence of registered events quantity on geomagnetic activity level was found for II type precipitations at 95 % significance level [28, 30]. The similar tendency was observed for I type quasistationary precipitations too [28, 29]. Unfortunately amount of sets for III and IV type precipitations now is not sufficient for statistical analysis.

Typical energy spectra of quasistationary equatorial precipitations are power-law $I \sim E^{-\alpha}$ [29, 30], where

$\alpha = 2{,}1 \pm 0{,}2$ for I and III types events

$\alpha = 1{,}8 \pm 0{,}1$ for II types events.

Analysis of other types of precipitations spectra is not complete now.

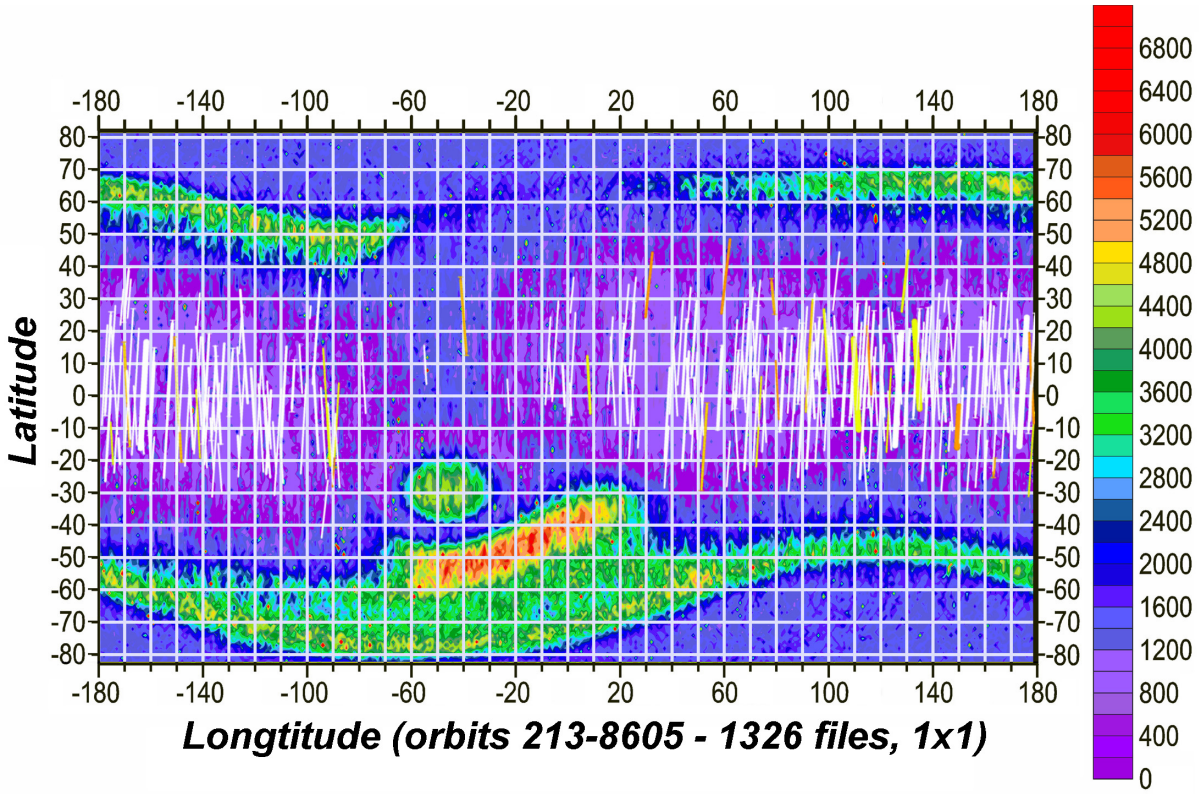

Figure 9: The count rate map in AVS-F low energy band averaged for 1.5 years of operation. 241 quasistationary equatorial precipitations are shown by lines (white — I type, orange — II type and yellow III one)

Most part of I–III types of precipitations is located in the strip-shape region (width 40°) practically symmetrical relatively geomagnetic equator (see. Fig. 2), the width of near-equatorial area, in which IV type events were observed, is ~20° [12]. So, the most part of precipitations are located in the region in which precipitations of electrons were registered by various satellites at low latitudes ($L \sim 1.5$) and in equatorial region [28, 30]. Quasistationary equatorial precipitations can be caused by charged particles precipitations in some regions of Earth magnetosphere, which were periodically intercepted by satellite.

References

1. A.S. Glyanenko, Yu.D. Kotov, A.V. Pavlov, A.I. Arkhangelskiy et al. The AVS-F experiment on recording rapidly changing fluxes of cosmic and gamma radiation prepared under the CORONAS-F project. // Instruments and Experimental Techniques, 1999, V. 42, #5, P. 596
2. A.I. Arkhangelskii, A.S. Glyanenko. The MicroPC module application in the AVS-F on-board equipment of the "Coronas-F" satellite // Modern Automation Technologies, №3, 2004, P. 30
3. S. N. Kuznetsov; K. Kudela, S. P. Ryumin et al. CORONAS-F satellite: Tasks for study of particle acceleration. // Advances Space Research, 2002, V. 30, #7, P. 1857
4. V.M. Pankov, V. L. Prokhin, Yu.G. Shkurkin, V.A. Yakovlev et al X-ray semiconductor (CdTe) spectrometer for solar flare and preflare studies // Radiophysics. Quantum Electronics, 1996, V. 39, #11-12, C. 1000
5. V.M. Pankov, V. L. Prokhin, N. G. Khavenson. The RPS-1 X-ray CdTe spectrometer onboard the CORONAS-F satellite // Solar System Research, 2006, V. 40, № 4, P. 314
6. I.V. Arkhangelskaja, O.I. Chervyakova, A.I. Arkhangelskii, A.S. Glyanenko, Yu.D. Kotov. The investigation of AVS-F spectroscopy tract stability in low energy gamma bend // Proceedings of the International conference "CORONAS-F: Three years of Solar activity observations (2001-2004)" held in Troitsk, IZMIRAN, January 31 – February 5 2005, P. 33
7. I.V. Arkhangelskaja, A.I. Arkhangelskii, A.S. Glyanenko, Yu.D. Kotov. Inflight calibration and results of database treatment of AVS-F apparatus in experiment onboard satellite CORONAS-F // Space science and technology, 2003,V. 9, #2, P. 20, Ukraine
8. I.V. Arkhangelskaja, A.I. Arkhangelsky, Yu.D. Kotov, S.N. Kuznetsov et al. The solar flare catalog in the low-energy gamma-ray range based on the AVS-F instrument data onboard the CORONAS-F satellite in 2001-2005 // Solar System Research, 2006, V. 40, №2, P. 133
9. I.V. Arkhangelskaja, A.I. Arkhangelskii, A.S. Glyanenko, Yu.D. Kotov et al. The solar flares observed in low energy gamma-ray band by AVS-F apparatus data onboard CORONAS-F satellite in 2001-2005 years, // Proceedings of the 11th European Solar Physics Meeting «The Dynamic Sun: Challenges for Theory and Observations», (ESA SP-600). 11-16 September 2005, Leuven, Belgium. Editors: D. Danesy, S. Poedts, A. De Groof and J. Andries, P.108.1, 2005
10. A.I. Arkhangelsky, I.V. Arkhangelskaja, Yu.D. Kotov, A.S. Glyaneneko et al. Solar flares observed by AVS-F instrument onboard CORONAS-F satellite during 2,5 year of it's operation // Multi-Wavelength Investigations of Solar Activity, IAU Symposium, V. 223, Cambridge, UK: Cambridge University Press, 2004, P.441
11. I.V. Arkhangelskaja, A.I. Arkhangelskii,, Yu.D. Kotov, A.S. Glyanenko et al. The solar flare catalog in the high-energy gamma-ray range based on the AVS-F apparatus data onboard the CORONAS-F satellite in 2001-2005 //

Proceedings of the Russian Conference "Experimental and theoretical investigations of the heliophysics activity base of prognosis " Editors: V.N. Obridko, V.V. Zaitsev. Troitsk, 2006, P. 9

12. I.V. Arkhangelskaja, A.I. Arkhangelskii, A.S. Glyanenko, Yu.D. Kotov, et al. The investigation of January 2005 solar flares gamma-emission by AVS-F apparatus data onboard CORONAS-F satellite in 0,1-20 MeV energy band, Proceedings of the 11th European Solar Physics Meeting «The Dynamic Sun: Challenges for Theory and Observations»\, (ESA SP-600). 11-16 September 2005, Leuven, Belgium. Editors: D. Danesy, S. Poedts, A. De Groof and J. Andries, P.107.1, 2005
13. I.V. Arkhangelskaja, A.I. Arkhangelsky, Yu.D. Kotov, S.N. Kuznetsov et al. The investigation of gamma-ray of solar flares by AVS-F apparatus data onboard CORONAS-F satellite in January 2005 // Solar System Research, 2008, №4, P.351
14. Yu.I. Yermolaev, L.M. Zelenyi, V.D. Kuznetsov, I.M. Chertok et al. Magnetic storm of November, 2004: Solar, heliospheric, and magnetospheric disturbances // Journal of Atmospheric and Solar-Terrestrial Physics, 2007, V. 70, №2-4, P. 334
15. I.V. Arkhangelskaja, A.I. Arkhangelsky, Yu.D. Kotov, S.N. Kuznetsov et al. Gamma-Ray Radiation of Solar Flares in October-November 2003 According to the Data Obtained with the AVS-F Instrument Onboard the CORONAS-F Satellite, // Solar System Research, 2006, V. 40, №4, P. 302
16. I.V. Arkhangelskaja, A.I. Arkhangelsky, Yu.D. Kotov, S.N. Kuznetsov. The investigation of the spectra of solar events observed in October-November 2003. // Multi-Wavelength Investigations of Solar Activity, IAU Symposium, V. 223, Cambridge, UK: Cambridge University Press, 2004, P.439
17. Yu.D. Kotov, I.V. Arkhangelskaja, A.I. Arkhangelsky, A.S. Glyanenko et al. The investigation of the gamma-emission of solar flare October 29, 2003 on data of AVS-F and SONG onboard the CORONAS-F Satellite // Izvestija RAN, Serija Physicheskaja, , 2005, V.69, #6, P.768
18. I.V. Arkhangelskaja, A.I. Arkhangelsky, Yu.D. Kotov, P.A. Kalmykov et al. January 20, 2005 solar flares characteristics investigation in high-energy gamma-band on AVS-F apparatus data // Proc. “Scientific Session of the Moscow Engineering Physics Institute – 2007”, Moscow: MEPhI, 2007, V. 7, P.19
19. A.I. Arkhangelskij, I.V. Arkhangelskaja, A.S. Glyanenko , Yu.D. Kotov. The observation of gamma-ray emission during January 20, 2005 solar flare // Abstracts of SEE2007, p. 50, 2007
20. Kostina M.S., I.V. Arkhangelskaja, A.I. Arkhangelsky, D.B. Amandzholova et al. Faint solar flares investigation on the data of AVS-F apparatus onboard the CORONAS-F Satellite // Proc. “Scientific Session of the Moscow Engineering Physics Institute – 2008”, Moscow: MEPhI, 2008, V.9, P.113
21. Arkhangelskaja I.V., Kotov Yu. D., Kostina M.S., Arkhangelsky A.I.et al. Faint solar flares with hard X-ray and gamma emission observed by AVS-F onboard CORONAS-F satellite. // Proceedings of The 37th Committee of Space Recearch Scientific Assembly (COSPAR 2008), 2008, in press

22. I.V. Arkhangelskaja, A.I. Arkhangelskij, A.S. Glyanenko , Yu.D. Kotov. Thin structure of temporal profiles of solar flares January 15, 17 and 20 2005 by data of AVS-F apparatus onboard CORONAS-F satellite // Abstracts of SEE2007, P. 37, 2007
23. I.V. Arkhangelskaja, A.I. Arkhangelskii, A.S. Glyanenko, Yu.D. Kotov, et al. Studying of temporal profiles behavior of solar flares January 2005 series iv various energy bands on data of AVS-F apparatus onboard CORONAS-F satellite // Proceedings of the Russian Conference "Experimental and theoretical investigations of the heliophysics activity base of prognosis " Editors: V.N. Obridko, V.V. Zaitsev. Troitsk, 2006, P. 15
24. I.V. Arkhangelskaya, A.I. Arkhangelskii, Yu.D. Kotov, S.N. Kuznetsov et al. Gamma-ray bursts recorded in 2001-2005 by the AVS-F instrument onboard the Coronas-F satellite in the low-energy gamma-ray range // Cosmic Research, V. 45, №3, P. 261
25. I.V. Arkhangelskaya, A.I. Arkhangelskii, A.S. Glyanenko, Yu.D. Kotov et al. The GRB detected in low energy gamma-ray band by AVS-F apparatus onboard CORONAS-F satellite in 2001-2005 years // Proceedings of the Eleventh Marcel Grossmann Meeting on General Relativity, edited by H. Kleinert, R.T. Jantzen and R. Ruffini, World Scientific, Singapore, 2008, in press
26. I.V. Arkhangelskaja, I.V. Afonina, A.I. Arkhangelskii, E.A. Borodina et al. Preliminary results of database treatment from AVS-F apparatus in energy range 0,1-11 MeV // Proceedings of the 18th European Cosmic Ray Symposium, Moscow, Russia, July 2002, P. 38.
27. I.V. Arkhangelskaja, D.B. Amandzholova, A. I. Arkhangelsky, Yu.D. Kotov. The investigation of quasystationary equatorial precipitations on AVS-F data // Proc. “Scientific Session of the Moscow Engineering Physics Institute – 2005”, Moscow: MEPhI, 2005, V. 7, P. 31
28. I.V. Arkhangelskaja, D.B. Amandzholova, A. I. Arkhangelsky, Yu.D. Kotov. The investigation of quasistationary equatorial precipitations registration frequency dependence from the Kp and Dst –indexes on AVS-F data // Proc. “Scientific Session of the Moscow Engineering Physics Institute – 2007”, Moscow: MEPhI, 2007, V. 7, P. 17
29. I.V. Arkhangelskaja, D.B. Amandjolova, A. I. Arkhangelsky, Yu.D. Kotov. Properties of the quasi-stationary precipitations by AVS-F apparatus data onboard CORONAS-F satellite. // Solar System Research, 2006, V. 42, #6, in press
30. D.B. Amandzolova, I.V. Arkhangelskaja, A.I. Arkhangelskiy, Yu.D. Kotov et al. The analysis of quasistationary equatorial precipitations observation frequency dependence from the geomagnetical activity level // Proceedings of The 20th European Cosmic Ray Symposium in Lisbon, Portugal, 2007, http://www.lip.pt/events/2006/ecrs/proc/ecrs06-s0-189.pdf